Precision Measurement of Parity-violation in Deep Inelastic Scattering Over a Broad Kinematic Range

December 15, 2008

Abstract

We propose to measure the parity-violating electroweak asymmetry A_{PV} in the deep-inelastic scattering of polarized electrons (PVDIS) to high precision in order to search for physics beyond the Standard Model in lepton-quark neutral current interactions. Presently, the atomic parity-violation measurement in ^{133}Cs provides important limits on such new physics, and the Qweak experiment at Jefferson Laboratory will provide an additional constraint. Our proposed PVDIS experiment will provide constraints of similar precision to these measurements, but will be unique in that it is sensitive to axial-hadronic currents. Such currents are only accessible in DIS; their interpretability in analogous measurements in elastic scattering is limited due to unconstrained and theoretically intractable radiative corrections. One measure of our sensitivity is that we will measure $\sin^2\theta_W$ with a precision of ± 0.0006.

In order to perform such a precise test, possible novel hadronic physics issues must be addressed. One is the violation of charge symmetry (CSV) at the quark level. Another is the contributions from interesting higher-twist operators. Since we will measure an asymmetry, some higher-twist contributions will cancel, but those particular higher-twist terms involving quark-quark correlations might remain at a significant level. Establishing whether or not these two effects are substantial is extremely interesting in itself.

We plan to use several different targets. Deuterium is ideally suited for the Standard Model test. With a hydrogen target, we can measure the d/u ratio in the proton. Finally, with a heavy nucleus like ^{208}Pb, we can provide a new window on the EMC effect.

In order to untangle the above physics, we plan to measure A_{PV} with a precision of about 0.5% over the range $0.3 < x < 0.7$ and with a dynamic range of Q^2 of about a factor of two. To reach the region where $x > 0.55$ with $W > 2$ GeV, scattering angles on the order of 30° with an 11 GeV beam are required. To obtain sufficient statistics, very high luminosity combined with a large azimuthal acceptance, about 1/3 of 2π, is required. Presently, no machine or apparatus exists which meets this requirement.

In this proposal, we present a design of a new spectrometer, called SoLID, which is based on a large solenoidal magnet. Fast-counting of particles through tracking, Cherenkov, and calorimeter detectors will provide sufficient resolution and particle identification for precision measurements at high rates in well-defined kinematics. Combined with upgraded polarimetry at the level of 0.5%, the resolution and luminosity of SoLID will provide the precision necessary for this broad program of electroweak studies.

P. Bosted, J. P. Chen, E. Chudakov, A. Deur, O. Hansen, C. W. de Jager, D. Gaskell, J. Gomez, D. Higinbotham, J. LeRose, R. Michaels, S. Nanda, A. Saha, V. Sulkosky, and B. Wojtsekhowski
Jefferson Lab, Newport News, VA 23606

P. A. Souder (*Contact**) and R. Holmes
Syracuse University, Syracuse, NY 13244

K. Kumar, D. McNulty, L. Mercado, and R. Miskimen
University of Massachusetts Amherst, Amherst, MA 01003

H. Baghdasaryan, G. D. Cates, D. Crabb, M. Dalton, D. Day, N. Kalantarians, N. Liyanage, V. V. Nelyubin, B. Norum, K. Paschke, S. Riordan, O. A. Rondon, M. Shabestari, J. Singh, A. Tobias, K. Wang, and X. Zheng
University of Virginia, Charlottesville, VA 22904

J. Arrington, K. Hafidi, P. E. Reimer, and P. Solvignon
Argonne National Laboratory, Argonne, IL 60439

D. Armstrong, T. Averett, and J. M. Finn
College of William and Mary, Williamsburg, VA 23173

P. Decowski
Smith College, Northampton, MA 01063

L. El Fassi, R. Gilman, R. Ransome, and E. Schulte
Rutgers, The State University of New Jersey, Piscataway, NJ 08855

W. Chen, H. Gao, X. Qian, Y. Qiang, and Q. Ye
Duke University, Durham, NC 27708

K. A. Aniol
California State University, Los Angeles, CA 90032

G. M. Urciuoli
INFN, Sezione di Roma, 00185 Roma, Italy

A. Lukhanin, Z. E. Meziani, and B. Sawatzky
Temple University, Philadelphia, PA 19122

P. M. King and J. Roche
Ohio University, Athens, OH 45701

E. Beise
University of Maryland, College Park, MD 20742

W. Bertozzi, S. Gilad, W. Deconinck, S. Kowalski, and B. Moffit
Massachusetts Institute of Technology, Cambridge, MA 02139

F. Benmokhtar, G. Franklin, B. Quinn
Carnegie Mellon University, Pittsburgh, PA 15213

G. Ron
Tel Aviv University, Tel Aviv, Israel 69978

T. Holmstrom
Longwood University, Farmville, VA 23909

P. Markowitz
Florida International University, Miami, FL 33199

X. Jiang
Los Alamos National Laboratory, Los Alamos, NM 87544

W. Korsch
University of Kentucky, Lexington, KY 40506

J. Erler
Universidad Autónoma de México, 01000 México D. F., México

M. J. Ramsey-Musolf
University of Wisconsin, Madison, WI 53706

C. Keppel
Hampton University, Hampton, VA 23668

H. Lu, X. Yan, Y. Ye, and P. Zhu
University of Science and Technology of China, Hafei, 230026, P. R. China

N. Morgan and M. Pitt
Virginia Tech, Blacksburg, VA 24061

J.-C. Peng
University of Illinois, Urbana-Champaign, IL 61820

H. P. Cheng, R. C. Liu, H. J. Lu, and Y. Shi
Institute of Applied Physics, Huangshan University, Huangshan, P. R. China

S. Choi, Ho. Kang, Hy. Kang, B. Lee, and Y. Oh
Seoul National University, Seoul 151-747, Korea

J. Dunne and D. Dutta
Mississippi State University, Mississippi State, MS 39762

K. Grimm, K. Johnston, N. Simicevic, and S. Wells
Louisiana Tech University, Ruston, LA 71272

O. Glamazdin and R. Pomatsalyuk
NSC Kharkov Institute for Physics and Technology, Kharkov 61108, Ukraine

Z. G. Xiao
Tsinghua University, Beijing, P. R. China

B.-Q. Ma and Y. J. Mao
School of Physics, Beijing University, Beijing, P. R. China

X. M. Li, J. Luan, and S. Zhou
China Institute of Atomic Energy, Beijing, P. R. China

B. T. Hu, Y. W. Zhang, and Y. Zhang
Lanzhou University, Lanzhou, P. R. China

C. M. Camacho, E. Fuchey, C. Hyde and F. Itard
LPC Clermont, Universit Blaise Pascal CNRS/IN2P3 F-63177 Aubire, France

A. Deshpande
SUNY Stony Brook, Stony Brook, NY 11794

A. T. Katramatou and G. G. Petratos
Kent State University, Kent, OH 44242

J. W. Martin
University of Winnipeg, Winnipeg, MB R3B 2E9, Canada

* e-mail: souder@physics.syr.edu

Contents

1 Introduction **4**

2 Motivation **6**

2.1 Parity Violation in DIS . . . 6
2.1.1 Introduction . . . 6
2.1.2 PVDIS in the QPM . . . 7
2.1.3 Additional Corrections . . . 9
2.2 Electroweak Physics . . . 9
2.2.1 Contact Interactions . . . 11
2.2.2 Z' Bosons . . . 12
2.2.3 Supersymmetry . . . 12
2.3 Hadron Physics with Deuterium . . . 13
2.3.1 Charge Symmetry Violation . . . 13
2.3.2 Higher Twist Effects in DIS . . . 15
2.3.3 Q^2 Dependence and Quark-Quark Correlations . . . 16
2.3.4 Higher Twist and the Operator Product Expansion . . . 17
2.3.5 Physics of $Y_3 a_3^D(x)$ . . . 19
2.4 Program for Deuterium . . . 20
2.4.1 Kinematic Points . . . 20
2.4.2 Fit of Asymmetry Data . . . 20
2.4.3 Sensitivity to Physics Beyond the Standard Model . . . 22
2.4.4 Summary of the Deuterium Program . . . 23
2.5 Physics with Other Targets . . . 23
2.5.1 Measuring d/u for the proton at high x . . . 23
2.5.2 Induced Nuclear Isospin Violation . . . 24

3 Large Acceptance Apparatus for High Luminosity **27**

3.1 General Requirements . . . 27
3.2 Solenoidal Spectrometer (SoLID) . . . 30
3.2.1 Overview . . . 30
3.2.2 Simulation . . . 33
3.2.3 Spectrometer Resolution . . . 33
3.2.4 Baffles . . . 34

3.2.5 Low Energy Background . . . 37
3.2.6 Trigger Logic . . . 37
3.2.7 Pion Background . . . 38
3.2.8 Acceptance and Rates . . . 39
3.2.9 Implementation . . . 41

4 Beam and Target **42**
4.1 Beam . . . 42
4.2 Target . . . 43

5 Systematic Corrections **45**
5.1 Kinematic Reconstruction . . . 45
5.2 Radiative Corrections . . . 46
5.2.1 Electromagnetic (EM) Radiative Correction . . . 46
5.2.2 Electroweak Radiative Correction . . . 46
5.3 Polarimetry . . . 47

6 Conclusion **49**
6.1 Collaboration . . . 49
6.2 Synergy with Other Proposals . . . 49
6.3 Beam Request . . . 49
6.4 Cost and Schedule . . . 50
6.5 Assignment of Tasks . . . 50

A Physics **51**
A.1 DIS Phenomenology . . . 51

B Detector Implementation for SoLID **53**
B.1 Solenoidal Magnet . . . 53
B.2 Coordinate Detectors . . . 54
B.3 Electromagnetic Calorimeter . . . 57
B.4 Cherenkov Detector . . . 58
B.5 Trigger . . . 59
B.6 Data Acquisition . . . 60

C Polarimetry **62**
C.1 Compton Polarimetry . . . 62
C.1.1 The Hall A Compton Polarimeter . . . 62
C.1.2 Systematic Uncertainties . . . 64
C.1.3 Summary of Compton Polarimetry Uncertainties . . . 68
C.2 Møller Polarimetry . . . 71
C.2.1 Møller Scattering . . . 71
C.2.2 Ways to Higher Accuracy . . . 71
C.2.3 Atomic Hydrogen Target . . . 73

C.2.4 Møller Polarimeter in Hall C 80

D Options: Double Toroid **84**
D.1 Overview 84
D.2 Toroidal Magnets 85
D.3 Spectrometer Resolution 88
D.4 The Acceptance and the Rates 89
D.5 Implementation 89
D.5.1 Magnets 90
D.5.2 Coordinate Detectors 90

Bibliography **100**

Chapter 1

Introduction

The advent of an 11 GeV beam at JLab will open up the possibility to explore deep-inelastic scattering (DIS) in the kinematic region of large Bjorken $x = Q^2/2M\nu$. One important probe is the parity-violating asymmetry:

$$A_{PV} = \frac{\sigma_R - \sigma_L}{\sigma_R + \sigma_L} \tag{1.1}$$

Since both the cross sections and asymmetries are large in parity-violating deep-inelastic scattering (PVDIS), high-precision measurements of the asymmetries are feasible. In addition, many of the systematic errors that arise in cross-section measurements, such as the thickness of the target and the solid angle acceptance of the detector, cancel in PVDIS, allowing for smaller systematic errors than is possible with cross-section measurements. Indeed, we propose to make a series of measurements in the kinematic range $0.3 > x > 0.7$, $W^2 > 4$ GeV^2, and a dynamic range in Q^2 of about a factor of two. The total precision for each point will be $< 1\%$ of the asymmetry.

We have identified a number physics issues that may be addressed with such a set of data:

1. Search for new interactions beyond the Standard Model (SM) in a unique way. The special feature of PVDIS is that it is sensitive to axial-hadronic currents, yet is insensitive to unknown radiative corrections that cloud the interpretation of lower energy experiments sensitive to these currents.

2. Search for Charge Symmetry violation (CSV) at the quark level.

3. Search for higher-twist effects in the parity-violating asymmetry. Significant higher-twist effects are observed in DIS cross sections, but in PVDIS large higher-twist contributions can only be due to quark-quark correlations.

4. Measure the d/u ratio in the proton, without requiring any nuclear corrections.

5. Determine if additional CSV is induced in heavier nuclei. Such an effect would have profound implications for our understanding of the EMC effect.

The above program requires an apparatus with large acceptance for scattering angles in the range $20^\circ - 35^\circ$. In order to do this, we have designed a new solenoidal spectrometer. The details of the design are the heart of this proposal. The design is based on the re-use of an existing magnet, such as those used at BaBar at SLAC, CLEO at Cornell, or CDF at Fermilab. Should none of these magnets be available, we mention in the Appendix an approach using a custom toroidal magnet.

The unique opportunities for experiments on parity-violation at Jlab with the 11 GeV upgrade were recognized in the NSAC long-range planning exercises. Four pertinent points were made in the report:

1. The field of fundamental symmetries is now recognized for its accomplishments and future potential to further the larger goals of Nuclear Physics. Notably, the SLAC E158 A_{PV} result in Møller scattering and the limits on strange quarks in the nucleon set by parity-violation experiments were highlighted among the important accomplishments of the field in the past seven years.

2. The third of the principle recommendations calls for significant new investments in this subfield and emphasizes the importance of electroweak experiments to further our understanding of the fundamental interactions and the early universe.

3. One of the overarching questions that serves to define this subfield is: "What are the unseen forces that were present at the dawn of the universe but disappeared from view as the universe evolved?"

4. To address this question and as part of the third principal recommendation, significant funds were recommended for equipment and infrastructure for two new parity-violating electron scattering projects (Møller scattering and parity-violating deep inelastic scattering or PVDIS) that would use the upgraded 11 GeV beam at Jefferson Laboratory.

We quote a particularly relevant part of the long range plan report: "A second thrust involves precise measurements of the PV deep-inelastic electron deuteron and electron-proton asymmetry. The asymmetries are 100 times larger that the PV Møller asymmetry, making a kinematic survey feasible. The first step in this program will be carried out with the existing 6 GeV beam, followed by additional experiments at 11 GeV. The variation of the asymmetry with both energy and Q^2 – as well as the use of different targets– will probe a variety of largely unexplored aspects of the nucleon's quark and gluon substructure. Ongoing theoretical activities will provide a comprehensive framework for interpretation of the deep-inelastic asymmetries and delineate their implications for both the Standard Model and its possible extensions".

Chapter 2

Motivation

2.1 Parity Violation in DIS

2.1.1 Introduction

For electron scattering, the cross section depends on the amplitudes for both photon and Z-boson exchange:

$$\sigma \propto |A_\gamma + A_Z|^2$$

At the low values of Q^2 available at JLab, the weak amplitude A_Z is much smaller than the electromagnetic amplitude. However, the parity-violating part of A_Z, denoted $\tilde{A}_Z$, can be isolated by the technique of measuring the helicity-dependent asymmetry

$$-A_{LR} = A_{PV} = \frac{\sigma_R - \sigma_L}{\sigma_R + \sigma_L} \sim \frac{\tilde{A}_Z}{A_\gamma} \sim \frac{G_F Q^2}{4\pi\alpha}(g_A^e g_V^T + \beta g_V^e g_A^T) \tag{2.1}$$

Here β is a kinematic-dependent factor that tends to be large for large scattering angles in the center-of-momentum frame. For the Standard Model, $g_A^e = 1$ is large, whereas $g_V^e = -1 + 4\sin^2\theta_W$ is small[1].

A large number of measurements of A_{PV} have been published or are in progress. Moreover, great progress has been made over the years in improving the precision of these measurements, both in terms of measuring tiny asymmetries and measuring the asymmetries with excellent relative precision. Some of the experiments focus on aspects of hadron structure, such as strange form factors of the nucleon [2, 3, 4, 5] or the radius of the neutron distribution in a heavy nucleus such as Pb [6]. Other measurements use targets and kinematics where the hadronic structure is understood and search for parity-violating extensions to the Standard Model [7, 8, 9, 10].

A notable gap in the above work is a precise test of the Standard Model prediction for hadronic axial-vector currents, the term with g_A^T in Equation 2.1. The main reason, best known in the case of elastic nucleon scattering, is that the electroweak radiative

[1]Here we are using the conventions from Hobbs and Melnitchouk [1], which are different from those used by the PDG.

corrections often have large uncertainties involving anapole moments or box diagrams containing more than one quark [11,12]. Thus a precise measurement, even at the appropriate kinematics, would be dominated by theoretical errors. The one exception is deep inelastic scattering (DIS). Since in this case the scattering is from isolated elementary quarks, all radiative corrections are calculable.

With the advent of the 11 GeV upgrade, significant phase space for DIS measurements becomes available. In addition to being sensitive to axial hadronic currents, DIS has a number of other attractive features:

1. The cross sections are large.
2. Backgrounds are manageable.
3. Large values of Q^2 imply large asymmetries, on the order of 10^{-3}.
4. Precision beam polarimetry is easier with high beam energy.

Given these advantages, we believe that with the apparatus that we are proposing, we can measure A_{PV} with a relative precision of $\sim 0.5\%$. This will improve the present limits on the axial-vector hadronic currents by about a factor of 20.

In light of the high proposed precision, we have comprehensively investigated hadronic corrections that might be significant. The corrections are smallest for isoscalar targets like deuterium. Even in deuterium, however, we have found two interesting effects:

1. Charge symmetry violation (CSV) at the quark level. Present limits on the assumption that the up quark distribution in the proton is the same as the down quark distribution in the neutron are not sufficient for our proposed precision.
2. Finite Q^2 effects. Such effects are significant in the cross sections for $x > 0.5$, but it is not known whether or not they cancel in the asymmetry. If they do not cancel, they provide direct evidence for quark-quark correlations in the nucleon.

We find that these hadronic effects are extremely interesting in themselves.

In order to untangle the hadronic and electroweak effects, we need to make precise measurements over as large a kinematic range as possible, changing Q^2, x, and y. The implementation of this program requires a high acceptance spectrometer that must operate at scattering angles on the order of 30°. In this proposal we present plans to build such a device.

2.1.2 PVDIS in the QPM

At JLab energies, the interactions of the Z-boson and heavier particles can be approximated by four-fermion contact interactions. The parity-violating part of the electron-hadron interaction can then be given in terms of phenomenological couplings C_{ij}

$$\mathcal{L}^{PV} = \frac{G_F}{\sqrt{2}}[\overline{e}\gamma^\mu\gamma_5 e(C_{1u}\overline{u}\gamma_\mu u + C_{1d}\overline{d}\gamma_\mu d) + \overline{e}\gamma^\mu e(C_{2u}\overline{u}\gamma_\mu\gamma_5 u + C_{2d}\overline{d}\gamma_\mu\gamma_5 d)]$$

with additional terms as required for the heavy quarks. Here C_{1j} (C_{2j}) gives the vector (axial-vector) coupling to the j^{th} quark. For the Standard Model,

$$C_{1u} = g_A^e g_V^u \approx -\frac{1}{2} + \frac{4}{3}\sin^2\theta_W \approx -0.19 \tag{2.2}$$

$$C_{1d} = g_A^e g_V^d \approx \frac{1}{2} - \frac{2}{3}\sin^2\theta_W \approx 0.34 \tag{2.3}$$

$$C_{2u} = g_V^e g_A^u \approx -\frac{1}{2} + 2\sin^2\theta_W \approx -0.030 \tag{2.4}$$

$$C_{2d} = g_V^e g_A^d \approx \frac{1}{2} - 2\sin^2\theta_W \approx 0.025 \tag{2.5}$$

Here we have used the conventions that $g_A^e = 1$, $g_V^e = -1 + 4\sin^2\theta_W$, $g_A^u = 1/2$, and $g_V^u = -1/2 + (4/3)\sin^2\theta_W$, etc. The numerical values include electroweak radiative corrections explained in Section 5.2.2.

The cross sections for DIS can be expressed in terms of structure functions $F_i^j(x, Q^2)$, as discussed in detail in Appendix A.1. Here $x = Q^2/2M\nu$ is the Bjorken scaling variable with M the nucleon mass. For the spinless case, there are two electromagnetic structure functions, F_1^γ and F_2^γ. For PVDIS, three more structure functions are involved, $F_1^{\gamma Z}$, $F_2^{\gamma Z}$ and $F_3^{\gamma Z}$. The axial-vector hadronic current is described by $F_3^{\gamma Z}$. The relative weighting of the different structure functions is a function of the kinematic variable $y \equiv \nu/E$, where ν is the energy loss in the lab frame.

In the limit of large Q^2, the structure functions can be described by parton distribution functions (PDFs) $f_i(x)$ ($\overline{f}_i(x)$), which are the probabilities that the i^{th} quark (antiquark) carries a fraction x of the nucleon momentum. In this limit, the structure functions have a logarithmic Q^2-dependence given by QCD evolution. With the definitions $f_i^\pm = f_i \pm \overline{f}_i$, $y = \nu/E$, the asymmetry can be written

$$A_{PV} = -\frac{G_F Q^2}{4\sqrt{2}\pi\alpha}\left[Y_1 a_1(x) + Y_3(y) a_3(x)\right] \tag{2.6}$$

where

$$Y_1 \approx 1; \quad Y_3 \approx \frac{1-(1-y)^2}{1+(1-y)^2} \equiv f(y) \tag{2.7}$$

and

$$a_1(x) = g_A^e \frac{F_1^{\gamma Z}}{F_1^\gamma} = 2\frac{\sum_i C_{1i} Q_i f_i^+(x)}{\sum_i Q_i^2 f_i^+(x)}; \quad a_3(x) = \frac{g_V^e}{2}\frac{F_3^{\gamma Z}}{F_1^\gamma} = 2\frac{\sum_i C_{2i} Q_i f_i^-(x)}{\sum_i Q_i^2 f_i^+(x)}$$

For isoscalar targets such as the deuteron, the structure functions cancel and we have

$$a_1^D(x) = \frac{6}{5}(2C_{1u} - C_{1d})\left(1 + \frac{0.6 s^+}{u^+ + d^+}\right); \quad a_3^D(x) = \frac{6}{5}(2C_{2u} - C_{2d})\left(\frac{u^- + d^-}{u^+ + d^+}\right) + \ldots \tag{2.8}$$

For $x > 0.4$, only valence quarks are important, and the expressions for a_1 and a_3 become constants. Then the asymmetry becomes

$$A_{PV}^D = -\frac{G_F Q^2}{\sqrt{2}\pi\alpha}\left(\frac{9}{20}\right)\left[1 - \frac{20}{9}\sin^2\theta_W + (1 - 4\sin^2\theta_W) f(y)\right]. \tag{2.9}$$

2.1.3 Additional Corrections

A detailed study of the above phenomenology [1] reveals additional corrections that will be important at our level of precision. First, the approximation that r^2 in Equation A.2 is unity. That and similar terms in Appendix A.1 make about a 0.5% correction for Q^2=5 GeV^2.

A more interesting observation is that the Y_1 term depends on y. We have

$$\lim_{y\to 0} Y_1 = \left(\frac{1+R^{\gamma Z}}{1+R^{\gamma}}\right); \quad \lim_{y\to 1} Y_1 \approx 1$$

where the second limit neglects the $2xyM/E$ term in Equation A.4.

Another important effect is target mass corrections. We anticipate that there will be substantial cancellation in the ratio A_{PV} as is the case for spin-dependent structure functions [13].

2.2 Electroweak Physics

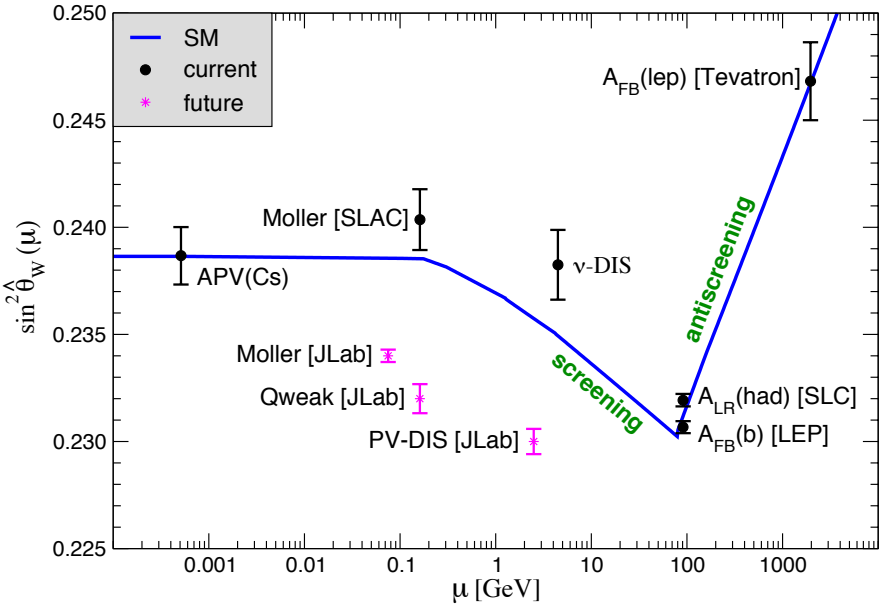

Figure 2.1: Plot of $\sin^2\theta_W$ versus Q for various precision experiments that are either completed or proposed.

One goal of PVDIS is to search for new physics beyond the Standard Model. With that in mind, we have designed the experiment so that we can obtain a precision of

0.6% on the combination of electroweak parameters in A_{PV}^{D}, as described in Section 2.4.3 below. One signature for the new physics is a deviation of the value of $\sin^2\theta_W$ obtained from comparing the data with Equation 2.9. The resulting sensitivity for our projected error is plotted in Figure 2.1, together with the results of other precise measurements, both published and proposed.

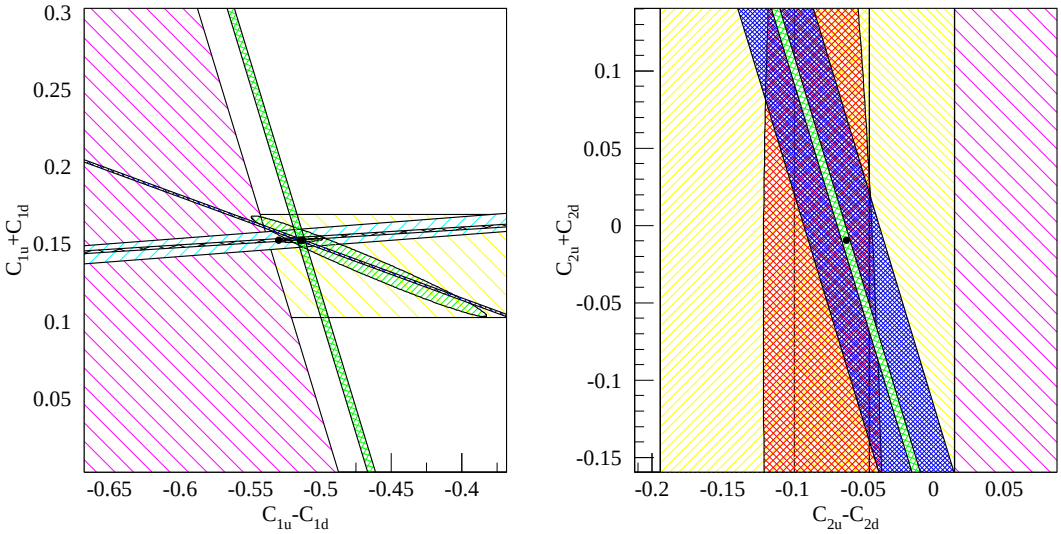

Figure 2.2: Constraints on the Standard Model from parity-violation experiments. The magenta/yellow hatched bands present the SLAC-DIS/Bates results. The cyan/black hatched band presents the Tl/Cs APV result. The narrow black band in the left plot shows the expected results from Qweak. The red band in the right plot shows the PDG constraint, and the blue band shows the expected precision from the approved 6 GeV PVDIS experiment (E08-011) [14] which will run in 2009. The green bands show the expected results from the experiment proposed. All limits are 1 standard deviation.

From a more phenomenological perspective, a measurement of A_{PV}^{D} provides a limit on deviations of the couplings C_{ij} from the predictions of the Standard Model. The resulting sensitivity on plots of the C_{ij}'s is given in Figures 2.2 and 2.3. There is a tremendous decrease in the allowed region of the C_2 plot. Both the high statistical sensitivity and the large values of Y_3 due to the large scattering angles are important for this improvement. The unique feature of PVDIS is that it provides a precise constraint in the plot of the C_2's.

As discussed in a recent review by Ramsey-Musolf and Su [15], combining various precision measurements at low energies can have an important impact on physics beyond the Standard Model. In this spirit, these data will be complementary to the anticipated high-energy data from the LHC. PVDIS is one example of these low-energy experiments [16].

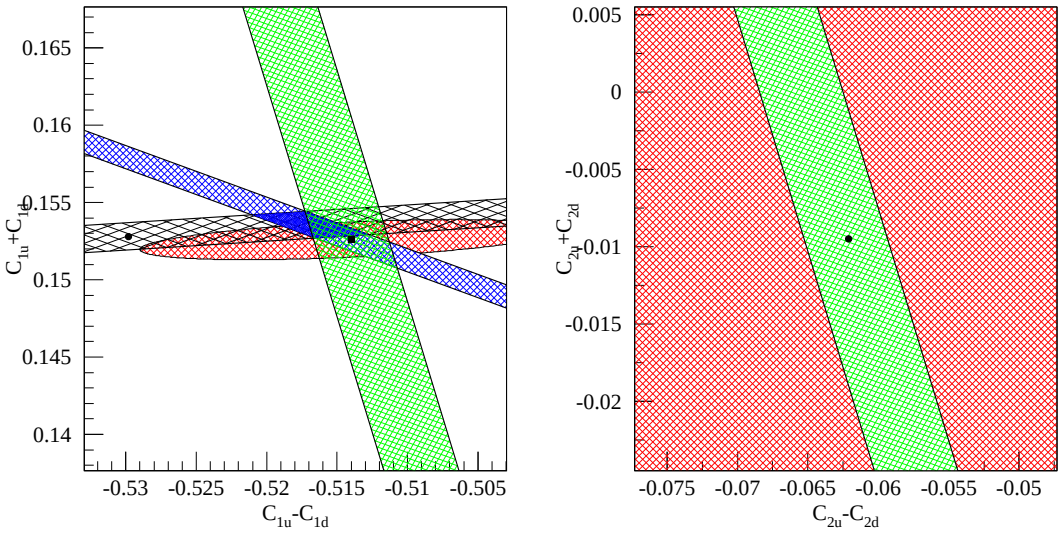

Figure 2.3: Expanded view of constraints on the Standard Model from parity-violation experiments (Fig. 2.2). The black crossed band presents the Cs APV results, the blue band - the expected QWEAK result, the red ellipse is a PDG fit, the black dots indicate the SM expectation and the best PDG fit, while the green band shows the current proposal. The anticipated error band from the future E08-011 experiment would also fill the entire region visible in the right plot. All limits are 1 standard deviation.

2.2.1 Contact Interactions

A general, model-independent way to parametrize the contributions of contact interactions of high-mass particles to low-energy measurements is to use the Lagrangian

$$\mathcal{L}_{eq} = \sum_{i,j=L,R} \frac{g_{ij}^2}{\Lambda^2} \, \overline{e}_i \gamma_\mu e_i \, \overline{q}_j \gamma^\mu q_j \tag{2.10}$$

Here $e_{L/R} = \frac{1}{2}(1 \mp \gamma_5)\psi_e$ and $q_{L/R} = \frac{1}{2}(1 \mp \gamma_5)\psi_q$ are the chirality projections of the fermion spinors, the g_{ij} are the coupling constants $g_{ij} = 2g_{ij}^u - g_{ij}^d$ and Λ is the mass scale.

The projected results on A_{PV}^D translates into a measurement of the linear combination of the phenomenological couplings $2\left[(2C_{1u} - C_{1d}) - 0.84\,(2C_{2u} - C_{2d})\right]$ to an accuracy of ± 0.0098. This translates into

$$\frac{\Lambda}{\sqrt{|g_{RR}^2 - g_{LL}^2 + g_{RL}^2 - g_{LR}^2|}} = \frac{1}{\sqrt{\sqrt{2}G_F|0.0098|}} \simeq 2.5 \text{ TeV}. \tag{2.11}$$

For example, models of lepton compositeness are characterized by strong coupling dynamics. Taking $\sqrt{|g_{RR}^2 - g_{LL}^2 + g_{RL}^2 - g_{LR}^2|} = 2\pi$ shows that mass scales as large as $\Lambda = 15.5$ TeV can be probed, corresponding to electron and quark substructure at the level of $\sim 10^{-20}$ m.

There are two kinds of new interactions that can contribute to PVDIS. One is the contact interactions mentioned above, which can include particles such as extra Z-bosons, leptoquarks, and supersymmetric (SUSY) partners. Contact interactions have real amplitudes, so they do not interfere with the imaginary amplitudes measured on the Z-pole at LEP and SLAC. Hence low energy measurements are competitive. In addition, the new generation of experiments at JLab, including Qweak, PVDIS, and Møller, has the precision to probe contributions to radiative corrections from loops involving new particles that do not directly couple to quarks and leptons.

2.2.2 Z' Bosons

A specific example of the kind of new physics to which the proposed experiment may be sensitive to are extra neutral gauge (Z') bosons with masses, $M_{Z'}$, in the TeV region. While these are very well motivated in many (if not most) models of physics beyond the SM, they are in general severely constrained by atomic parity violation (APV) measurements in Cs (and Tl) which agree with the SM prediction. However, APV in heavy nuclei is sensitive roughly to the sum of up and down quark vector couplings, and is thus blind to models where these are of similar size but opposite sign.

An example is the case where only right-handed quarks and leptons are charged under the underlying extra $U(1)'$ gauge factor[2] with charges proportional to the third component of the $SU(2)_R$ gauge group appearing in left-right symmetric models (it is not actually necessary that the $U(1)'$ is promoted to $SU(2)_R$). This case is interesting since the current precision electroweak data can accommodate such a heavy Z' with a mass as small as 660 GeV. If this case was actually realized in nature, the proposed measurement would see a 4σ deviation from the Standard Model prediction. For this particular example, the senstivity of this proposal exceeds that of any other low-energy parity-violation measurement in the electron-quark sector.

2.2.3 Supersymmetry

Another good example of new physics contributing to A_{PV} is in the case of SUSY. Predictions for the contributions of SUSY to both PVDIS and Qweak for models of supersymmetry (SUSY) are shown in Fig. 2.4. There are two classes of models shown, one that conserves R-parity and one that does not. For R-parity conserving models, where the effects are confined to loops, PVDIS is a bit more sensitive, but the predictions are highly correlated. For the R-parity-violating case, where contact interactions are important, the predictions for the two experiments are totally uncorrelated. If SUSY were observed at the LHC and the result from PVDIS were below the prediction, the implication would be that SUSY violates R-parity, which in turn implies that the lightest SUSY particle is unstable and is not a good candidate for dark matter.

[2]For instance, a model of this type can be obtained from an E_6 gauge group when large kinetic mixing with the hypercharge boson is induced.

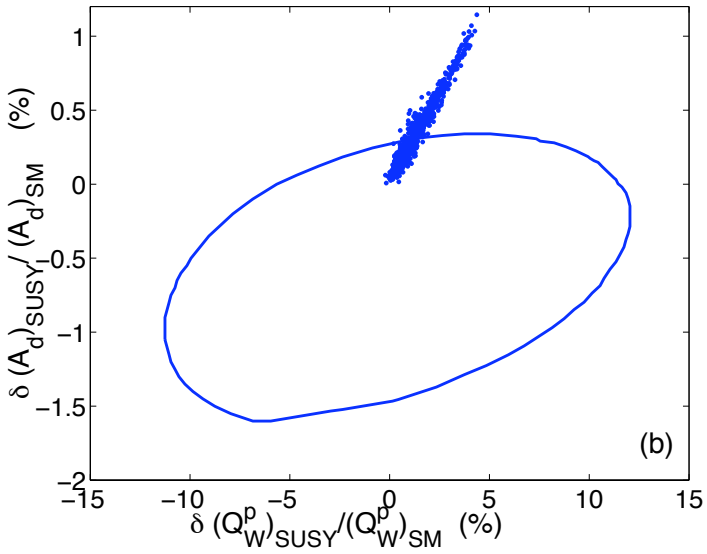

Figure 2.4: Implications of a measurement of PVDIS and Qweak for SUSY models. Dots: typical models for the R-parity conserving case. Line: region allowed at the 95% confidence level for models that violate R-parity but are consistent with other existing electroweak data.

2.3 Hadron Physics with Deuterium

2.3.1 Charge Symmetry Violation

One critical assumption for the cancellation of the structure functions in A_{PV} for the deuteron is charge symmetry, namely $u^p = d^n$ and $u^n = d^p$. Charge symmetry violation (CSV) can be parametrized by new PDFs

$$\delta u \equiv u^p - d^n; \quad \delta d \equiv d^p - u^n; \quad R^{CSV} \equiv \frac{\delta u - \delta d}{u + v}$$

Although the δu and δd are small, the ratio R^{CSV} can be significant if these CSV PDFs drop more slowly than the valence u and d with increasing x. There is no direct evidence for CSV at the parton level [17]. However, our PVDIS data will be more sensitive to CSV than any previous data, so we can set the best limits at large values of x.

There is some indirect evidence for CSV in neutrino scattering [18,19]. The Paschos-Wolfenstein ratio

$$R^{PW} = \frac{\sigma\langle \nu N \to \nu X\rangle - \sigma\langle \overline{\nu} N \to \overline{\nu} X\rangle}{\sigma\langle \nu N \to \mu X\rangle - \sigma\langle \overline{\nu} N \to \overline{\mu} X\rangle} \sim \frac{1}{2} - \sin^2\theta_W$$

which has been precisely measured by the NuTeV collaboration [20], is quite sensitive to CSV. In particular,

$$\frac{\delta R^{PW}}{R^{PW}} \sim 0.85 R^{CSV}$$

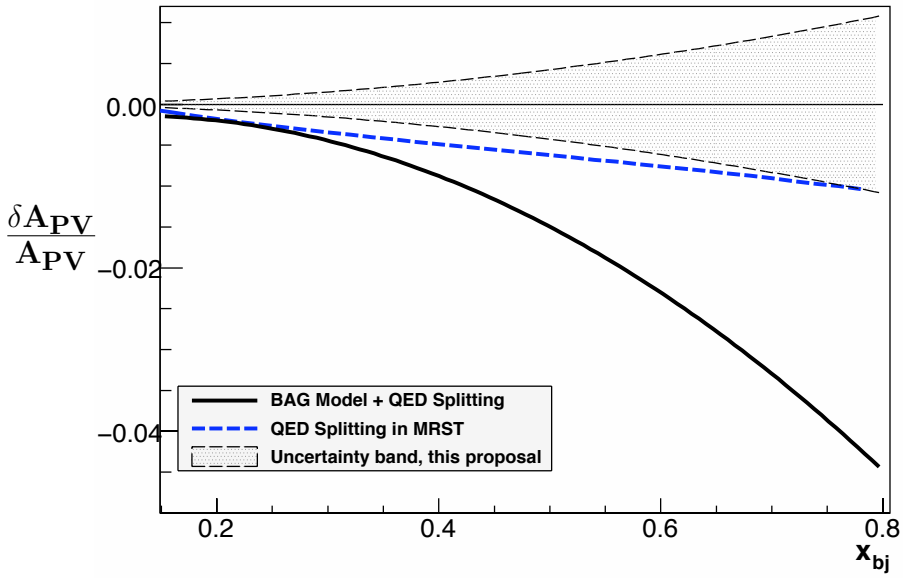

Figure 2.5: CSV predictions as a function of x. The vertical axis is the fractional change in A_{PV} due to CSV. The uncertainty band is the result of the fit discussed in Section 2.4.2. The MRST results shown here account for QED splitting in the Q^2 evolution only, and do not include non-pertubative QCD effects [24].

The discrepancy of the NuTeV result with the Standard Model expectation may indeed be due to CSV.

As a consequence of the above, the MRST group inserted CSV-violating terms to their global fits [21] and found that sufficient CSV is allowed to account for the NuTeV result. Non-zero values of R^{CSV} have been suggested in the literature caused both by non-perturbative QCD effects [22, 23] as well as QED effects in the Q^2 evolution [24, 25]. These are also in the range that would be significant for the NuTeV result.

The corrections due to CSV for A_{PV} for deuterium are

$$\frac{\delta^{CSV} a_1^D}{a_1^d} = \left(\frac{3}{10} + \frac{2C_{1u} + C_{1d}}{2(2C_{1u} - C_{1d})}\right) R^{CSV}$$

$$\frac{\delta^{CSV} a_3^D}{a_3^d} = \left(\frac{3}{10} + \frac{2C_{2u} + C_{2d}}{2(2C_{2u} - C_{2d})}\right) R^{CSV}$$

The effect of the CSV suggested in Ref. [22, 23, 24, 25] on A_{PV} is plotted in Figure 2.5. The size of the CSV effect is within reach of our sensitivity.

Since we can obtain high precision in several narrow bins of x for $x > 0.4$ with the JLab upgrade, we will be in an ideal position to study CSV. In contrast to physics beyond the Standard Model, the effect depends strongly on x. This signature will be a powerful method for discriminating CSV from new physics as an explanation for any deviation from the prediction of Equation 2.8.

Although the Paschos-Wolfenstein ratio is more sensitive to R^{CSV}, neutrino experiments to date have not been able to obtain high statistics on small bins in the relevant kinematic range. Another approach to studying CSV is to measure asymmetries in W-production at colliders, but the experimental sensitivity is not very good [26]. Other possible CSV experiments include pion-induced Drell-Yan scattering and pion electroproduction sum rules [27, 28], but these approaches have complications such as fragmentation functions and CSV in sea quarks.

2.3.2 Higher Twist Effects in DIS

A remarkable feature of DIS behavior is that higher twist effects for data where the mass of the final state $W > 2$ GeV are found to be small. For example, the higher twist terms have been determined recently for the measured e-p DIS structure functions $F_2(x, Q^2)$ [21] after the DGLAP evolution is removed. The ansatz is

$$F_2^\gamma(x, Q^2) = F_2^\gamma(x)(1 + D(x)/Q^2)$$

It turns out that the values of the $D(x)$ depend upon how many orders of α_s are taken in the DGLAP evolution of the PDFs. At leading order (LO), the higher twist contributions are significant and similar to the results of older analysis [29, 30]. However, as higher orders are taken, NLO, NNLO, and NNNLO, $D(x)$ becomes quite small, especially for $x < 0.4$. The values of D_i for both LO and NNNLO are summarized in Table 2.1. Recently the work on higher twists has been extended to one more order [31].

To interpret the size of higher twist terms at large values of x, one must take into account the relationship between W, Q^2 and x:

$$Q^2 = (W^2 - M^2)/(1/x - 1).$$

If $W = 2$ GeV is taken as the threshold for DIS behavior, then there is a threshold Q^2 denoted Q_t^2. Values for Q_t^2 are also given in Table 2.1. The maximum size of the higher twist effect that can be measured is thus $D(x)/Q_t^2$, which is also given in Table 2.1 as a fraction of $F_2^\gamma(x)$. This fraction is large enough to motivate a measurement only at high x.

We can include higher twist terms in $a_1(x)$ by defining

$$a_1(x, Q^2) = a_1(x)(1 + C(x)/Q^2).$$

As described in the next section, it is only quark-quark correlation that contributes to $C(x)$, whereas many possible higher-twist operators might contribute to $D(x)$. Hence it is plausible that $C(x) \leq D(x)$. Based on this assumption and Table 2.1, higher twist effects in $C(x)$ are probably impractical to isolate in PV DIS for $x < 0.4$. However, for $0.5 < x < 0.7$, it is possible that these effects could be observed cleanly. Moreover, since the effects of the DGLAP evolution cancel in the ratio $a_1^D(x)$, there is no problem with the order to which the evolution is performed.

Table 2.1: Higher twist coefficients $D(x)$ from Ref. [21].

x	$D(x)$ (LO)	$D(x)$ (N^3LO)	Q_t^2	$D(x)/Q_t^2$ (%) (LO)	$D(x)/Q_t^2$ (%) (N^3LO)
0.15	-0.07	0.01	0.5	-14	0.2
0.25	-0.11	0.00	1.0	-11	0
0.35	-0.06	-0.01	1.7	-3.5	-0.059
0.45	0.22	.11	2.6	8	4
0.55	0.85	0.39	3.8	22	10
0.65	2.6	1.4	5.8	45	24
0.75	7.3	4.4	9.4	78	47

2.3.3 Q^2 Dependence and Quark-Quark Correlations

The term $Y_1 a_1^D$ involves only conserved vector currents. As a consequence, we can make a strong statement about possible hadronic corrections that were addressed by Bjorken [32], Wolfenstein [33], and Derman [34] shortly after the data of Prescott, et al. were published. Going back to the hadronic tensor in terms of currents, we can write a_i^D as

$$Y_1 a_1^D \propto \frac{L_\gamma^{\mu\nu} \sum_X \{\langle X|J_\mu^{ZV}|\rangle^* \langle X|J_\nu^\gamma|D\rangle + H.C.\}(2\pi)^3 \delta(P_X - p - q)}{L_\gamma^{\mu\nu} \sum_X \{\langle X|J_\mu^{\gamma}|\rangle^* \langle X|J_\nu^\gamma|D\rangle + H.C.\}(2\pi)^3 \delta(P_X - p - q)}$$

where J^{ZV} is the vector part of the weak current. Next, we decompose the vector currents in terms of isospin

$$V_\mu = (\overline{u}\gamma_\mu u - \overline{d}\gamma_\mu d); \quad S_\mu = (\overline{u}\gamma_\mu u + \overline{d}\gamma_\mu d)$$

and define

$$\langle VV\rangle = L_\gamma^{\mu\nu} \sum_X \langle X|V_\mu|D\rangle^* \langle X|V_\nu|D\rangle (2\pi)^3 \delta(P_X - p - q)$$

with similar expressions for $\langle SS\rangle$ and $\langle SV\rangle$

Then the asymmetry is proportional to

$$Y_1 a_1^D \propto \frac{(C_{1u} - C_{1d})\langle VV\rangle + \frac{1}{3}(C_{1u} + C_{1d})\langle SS\rangle}{\langle VV\rangle + \frac{1}{3}\langle SS\rangle} \tag{2.12}$$

The key here is that the $\langle SV\rangle$ term vanishes in the absence of CSV. Strange quarks have also been neglected. If $\langle VV\rangle = \langle SS\rangle$, the hadronic structure completely cancels. The difference between $\langle VV\rangle$ and $\langle SS\rangle$ can be written

$$\langle VV\rangle - \langle SS\rangle = \langle (V - S)(V + S)\rangle \propto$$

$$L_\gamma^{\mu\nu} \sum_X \{\langle X|\overline{u}\gamma_\mu u|D\rangle^* \langle X|\overline{d}\gamma_\nu d|D\rangle + H.C.\}(2\pi)^3 \delta(P_X - p - q) \tag{2.13}$$

If this expression vanishes, all of the hadronic structure in Equation 2.12 cancels and the $Y_1 a_1^D$ part of the asymmetry is strictly independent of Q^2. The right hand side of Equation 2.13 is a correlation between u and d quarks. Thus any Q^2 dependence observed in this term will be a measure of quark correlations. The only assumption is that the hadronic vector current is conserved (CVC).

The valence PDFs drop rapidly after $x \sim 0.3$. However, the x relevant to the quark-quark correlation function is the sum of the individual x-values of each quark, so it is likely that the correlation function doesn't fall rapidly until $x \sim 0.6$ or so. Thus the ratio of diquarks to single quarks may be strongly enhanced at large x. This argument suggests that the x-dependence of the diquarks could be similar to the observed x-dependence of the higher twist coefficients $C(x)$.

Based on the above ideas, one method to remove the contribution of higher twist terms is to do a global fit of the form $D(X) = \alpha(1-x)^{-n}$, where α and n are parameters to be fit. If little Q^2-dependence is observed, tight bounds on the amplitudes will be found for $n > 2$. In this scenario, the contribution of the uncertainties in the higher twist coefficient to the high Q^2 point at $x \sim 0.4$ would be small.

In summary, the observation of Q^2-dependent effects would be of particular interest [35] in PVDIS because:

1. The experimental signature is especially clean. It is a violation of the QPM prediction that varies with both Q^2 and x. Since the DGLAP evolution cancels in the ratio, there is no uncertainty associated with the order to which the evolution is performed.

2. The theoretical interpretation, namely quark correlations, is well defined and interesting.

2.3.4 Higher Twist and the Operator Product Expansion

Estimates of the size of higher twist effects that use the operator product expansion (OPE) in QCD have been made by Castorina and Mulders [36] and Fajfer and Oakes [37]. These papers are based on the OPE analysis of Jaffe and Soldate [38], in which the twist-4 ($\sim 1/Q^2$) contributions are expressed in terms of a set of symmetric, traceless, and derivative-free operators. The QCD equations of motion are used to eliminate those operators that arise that do not satisfy these conditions. Such operators are a starting point for a rigorous phenomenology of higher twist effects. The computation of the matrix elements of these operators is presently less rigorous, and the MIT bag model has been used to make rough estimates.

For their analysis, Castorina and Mulders use a slightly different expression for the asymmetry

$$\frac{A}{Q^2} = a_1 + a_2 f(y) + a_3 g(y) + a_4 f(y) g(y)$$

where

$$f(y) = \frac{1-(1-y)^2}{1+(1-y)^2}; \quad g(y) = \frac{y^2}{1+(1-y)^2}$$

and

$$a_1 = -\frac{G_F}{4\sqrt{2}\pi\alpha}\frac{F_2^{\gamma Z}}{F_2^{\gamma}}$$

$$a_2 = -\frac{G_F}{4\sqrt{2}\pi\alpha}(1-4\sin^2\theta_W)\frac{xF_3^{\gamma Z}}{F_2^{\gamma}}$$

$$a_3 = -\frac{G_F}{4\sqrt{2}\pi\alpha}\left[\frac{2xF_L^{\gamma}F_2^{\gamma Z}}{(F_2^{\gamma})^2} - \frac{2xF_L^{\gamma Z}}{F_2^{\gamma}}\right]$$

$$a_4 = -\frac{G_F}{4\sqrt{2}\pi\alpha}(1-4\sin^2\theta_W)\frac{2xF_L^{\gamma}xF_3^{\gamma Z}}{(F_2^{\gamma})^2}$$

where the approximation

$$\frac{1}{F_2 - g(y)2xF_L} \approx \frac{1}{F_2}\left(1 + \frac{g(y)2xF_L}{F_2}\right)$$

is used and F_2 is used as the denominator instead of F_1 as is done in the appendix.

The higher twist contributions are given in terms of constants K_1 and K_2 computed in the MIT bag model;

$$a_1 = -\frac{G_F}{4\sqrt{2}\pi\alpha}\frac{9}{4}\left[1 + \frac{1}{Q^2}\left(-1.4K_1 + 3.8K_2\right) - \frac{20}{9}\sin^2\theta_W\right]$$

$$a_2 = -\frac{G_F}{4\sqrt{2}\pi\alpha}\frac{9}{4}\left[1 + \frac{1}{Q^2}\left(11.5K_1 - 23.5K_2\right)\right](1-4\sin^2\theta_W)$$

$$a_3 = 0$$

$$a_4 = \frac{G_F}{4\sqrt{2}\pi\alpha}\frac{9}{4}\left[\frac{1}{Q^2}\left(4K_1 - 3.5K_2\right)\right](1-4\sin^2\theta_W)$$

The most striking result is that $a_3 = 0$. As stated in the paper, this feature arises because the breaking of the Callan-Gross relation ($F_L = 0$) is due to two-quark-gluon operators, which contribute to the γ and γZ terms proportional to the leading twist-2 results. Therefore, there is no contribution to the ratio. This is consistent with the argument due to Bjorken that the only higher twist operators in a_1 involve quark-quark correlations, which are four-quark operators. This result of the calculation is expected to be quite general in the context of QCD.

The analysis of Castorina and Mulders only considered one moment of the higher twist contributions, so it applies only to the average over all x-values. It is quite likely, however, that the effects are larger at larger x. From a theoretical standpoint, the quark-quark correlations add the x-values of each quark, resulting in relatively greater strength

at larger x, as suggested by Brodsky [35]. From an empirical standpoint, the higher twist contribution to F_2^γ is observed to be significant only at large x as discussed in Sec. 2.3.2.

The higher twist contribution to the electromagnetic structure function

$$F_2^\gamma \to F_2^\gamma \left[1 + \frac{1}{Q^2}\left(17.4K_1 - 29K_2\right)\right]$$

is much larger than the contribution to a_1. It is not clear if this is an artifact of the MIT bag model and other approximations or a more general feature in QCD. The higher twist effects in the a_2 term are larger. However, the higher twist in the F_3 structure functions observed in neutrino scattering [39] have strength at moderate x, in sharp contrast to the electro-production data. It is possible that future theoretical work might shed light on these and other similar issues.

2.3.5 Physics of $Y_3 a_3^D(x)$

For the contribution to A_{PV} due to $F_3^{\gamma Z}$, there is no CVC theorem to help cancel uncertainties in the structure functions in the asymmetry. Fortunately, the $a_3(x)$ term is small in the Standard Model

$$\frac{a_3(x)}{a_1(x)} \sim 11.5\%$$

so a precision of only about 5% is required. The suppression factor is essentially the ratio of electron-Z couplings g_V^e/g_A^e.

In the QPM, the structure functions cancel if the sea quarks are negligible. Based on experiments of muon pair production by the Drell-Yan mechanism, sea quarks are known to be negligible at large x. The remaining problem is the dependence of R^γ in the Y_3 factor. Since R^γ is known from data [40] with an uncertainty of about 0.05, the uncertainty in $Y_3 a_3^D$ contributes about 0.5% to APV.

Another approach is to note that the axial current is just an isospin rotation of the $\nu - D$ *charge current* interaction

$$F_3^{\gamma Z} \propto F_3^\nu - F_3^{\overline{\nu}}$$

Thus data [41] can be used to determine $F_3^{\gamma Z}/F_2^\gamma$. Since

$$\lim_{y\to 0} Y_3 a_3^D = y\frac{F_3^{\gamma Z}}{F_2^\gamma}; \quad \lim_{y\to 1} Y_3 a_3^D = \frac{F_3^{\gamma Z}}{F_1^\gamma} = C_{2u} - C_{2d}$$

where the second equality arises from the absence of sea quarks at large x in the QPM. Finally, $Y_3 a_3^D$ for arbitrary y is a weighted sum of the above two limits. This procedure also has an acceptable uncertainty.

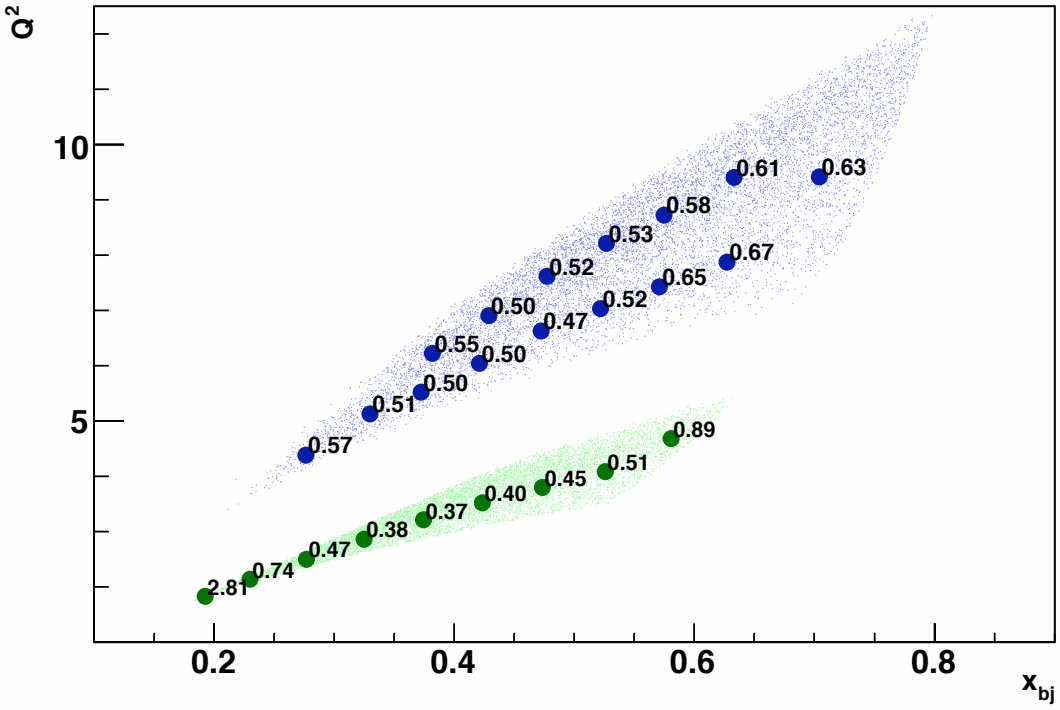

Figure 2.6: Errors in percent for A_{PV} for bins in Q^2 and x. The running times are 120 days with an 11 GeV beam and 60 days with a 6.6 GeV beam. The beam current is 50μa with a polarization of 85%.

2.4 Program for Deuterium

2.4.1 Kinematic Points

We plan to run for 120 days at 11 GeV and 60 days at 6.6 GeV. We assume a beam current of 50 μA and a polarization of 85%. The projected error bars for a selected binning over x and Q^2 is shown in Figure 2.6. All points have $W^2 > 4$ GeV^2. Most bins have $Y_3 \sim 0.84$. For $0.3 < x < 0.6$, there is a dynamic range of a factor of two in Q^2. There is one bin with average $x \sim 0.7$.

2.4.2 Fit of Asymmetry Data

The observation of CSV is possible with our apparatus only if the effect varies with x. An x-independent CSV effect would be indistinguishable from a change in the C_{1q}'s. It is quite natural, however, to expect that the x-dependence is similar to that shown in Figure 2.5, and we will make that assumption in our further discussion. From observations of higher-twist contributions to DIS cross sections, it is also natural to assume that Q^2-dependent effects will also increase with increasing x.

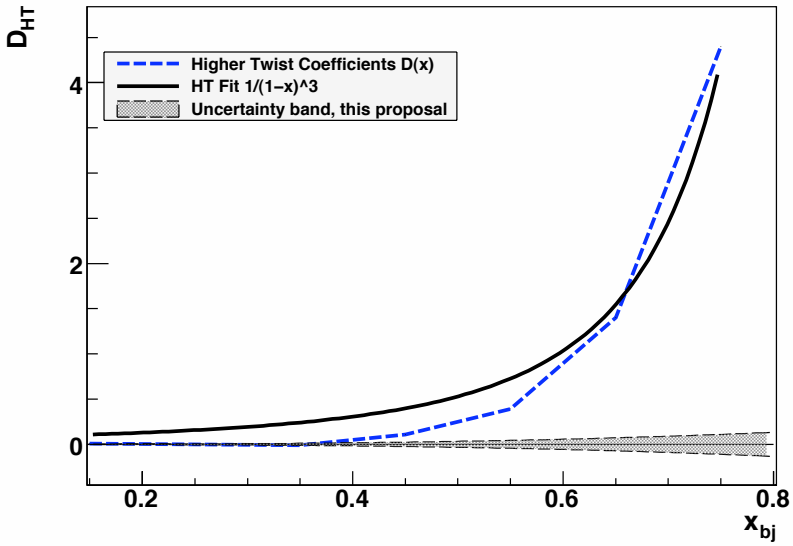

Figure 2.7: Demonstration of sensitivity to Q^2-dependent effects. Plotted are the higher-twist coefficients $D(x)$ from Ref. [21], listed in Table 2.1. Also shown is a fit to these coefficients using the form $(1-x)^{-3}$. The uncertainty band is the result of the fit discussed in Section 2.4.2.

Under these assumptions, independent sensitivity to the various possible contributions depends critically on the ranges of x and Q^2 which can be explored with precision measurements of A_{PV}^D. With the projected data displayed in Figure 2.6, we can obtain asymmetries at the same x and y with a dynamic range in Q^2 of about $\sqrt{2}$. The dynamic range is obtained by comparing the 11 GeV data with the 6.6 GeV data. We can improve this dynamic range in Q^2 to a factor of 2 by allowing the value of y to change slightly, by about $\Delta y \sim 0.2$. The uncertainty introduced, which is due only to uncertainty in the C_2's times Δy, is negligible. This applies for values of x up to 0.6.

To untangle the effects of hadronic and electroweak physics, we plan to fit the asymmetries to a function of the form

$$A_{PV}^D = A_{PV}^{EW}\left(1 + \beta_{HT}\frac{1}{(1-x)^3 Q^2} + \beta_{CSV}x^2\right) \tag{2.14}$$

The resulting statistical errors on the fit parameters are:

$$\delta A_{PV}^{EW}/A_{PV}^{EW} = 0.3\%; \quad \delta\beta_{HT} = 0.0026; \quad \delta\beta_{CSV} = 0.017$$

With this method, we use the full statistical power of the data set. However, the result has some sensitivity to the exact form of the chosen fitting functions. Under the scenario where the hadronic effects are small, these errors are negligible as long as we assume that CSV and higher twist effects depend strongly on x, as expected. The one-sigma band for the CSV term is plotted in Figure 2.5, the corresponding band for the higher-twist term is shown in Figure 2.7.

Table 2.2: Error budget in A_{PV}^{EW} at $x = 0.4$ for the test of the Standard Model

Source	Uncertainty in %
Statistics	0.3
Polarimetry	0.4
Q^2	0.2
Radiative Corrections	0.3
Total	0.6

If the pattern of higher twist effects is the same for A_{PV} as it is for the cross sections (Sec. 2.3.2, Table 2.1), then at $x = 0.6$ the asymmetries at the different Q^2 values will differ by 15%. In that scenario, the rapid x-dependence of the higher-twist coefficients for the cross section would imply that higher twist effects would still be negligible at $x = 0.4$. This scenario is illustrated in Fig. 2.7. With a comparable x-dependence, a Q^2-dependent effect as small as ∼1/30th of the effect seen in cross-section measurements would be easily identifiable given our statistical precision.

2.4.3 Sensitivity to Physics Beyond the Standard Model

If the hadronic terms are omitted from the fit, the error in A_{PV}^{EW} is 0.1%. The 0.3% error we quote from the fit is effectively dominated by an extrapolation error. The error on A_{PV}^{EW} increases to 0.6% when the systematic errors listed in Table 2.2 are included. This error corresponds to the vertical axis on Figure 2.4.

Presently, the atomic parity-violation in Cs is the most sensitive measurement of a combination of the C_{ij}'s, the parity-violating couplings in electron-quark sector. After the data on PVDIS and Qweak are obtained, there will be two more measurements of similar precision. One might then ask which of the experiments is most sensitive to new physics. Strictly speaking, there is no model-independent answer to this question. However, it is reasonable to assume that deviations δC_{ij} in any of the couplings are equally likely. In that spirit, the regions allowed by the measurements should be plotted on scales with equal units for each of the C_{ij} as we have chosen to do in Figures 2.2 and 2.3.

Equivalently, one can express the result of any measurement as a normalized linear function $M(C_{ij})$

$$M(C_{ij}) = \sum_{ij} \alpha_{ij} C_{ij}; \quad \sum_{ij} |\alpha_{ij}|^2 = 1$$

so that the experiments with the smallest value for δM are the most sensitive to new physics. Table 2.3 gives the projected results in this method. A final measure, which is more subjective, is the error in $\sin^2\theta_W$. A plot of the sensitivity of various experiments

Table 2.3: Comparisons of the different parity-violation experiments in the electron-quark sector by two different criteria

Experiment	$M(C_{ij})$	δM	$\delta \sin^2\theta_W$
APV (Cs)	$0.67C_{1u} + 0.75C_{1d}$	0.0007	0.0014
Qweak	$0.89C_{1u} + 0.45C_{1d}$	0.0007	0.0007
PVDIS	$0.68C_{1u} - 0.34C_{1d}$		
	$+0.58C_{2u} - 0.29C_{2d}$	0.0017	0.0006

to $\sin^2\theta_W$ is given in Figure 2.1. PVDIS does well by this measure, with a sensitivity of $\delta \sin^2\theta_W = 0.0006$.

If a large violation of the Standard Model is observed, measurements made with the maximum possible difference in Y can be used to separate the contributions from the C_{1q}'s and the C_{2q}'s. By comparing data at 12° and 35°, a dynamic range in the difference of $\Delta Y \sim 0.5$ can be achieved. However, the Q^2 values will be ~ 3 GeV^2 for the lowest Y and ~ 6 GeV^2 for the highest Y. The procedure can be justified if the observed higher twist effects are negligible at large x and assumed to be much smaller at lower x.

2.4.4 Summary of the Deuterium Program

This experiment, like the strange quark experiments before, is almost guaranteed to provide answers to one or more significant questions: Are there large CSV effects in the parton distributions? Is there evidence for significant quark-quark correlations that lead to a departure from the parton model at moderate Q^2? If SUSY is seen at the LHC, do we have evidence for the breaking of R-parity which would (a) preclude conventional WIMP dark matter in the MSSM and (b) imply that neutrinos are Majorana particles?

2.5 Physics with Other Targets

2.5.1 Measuring d/u for the proton at high x

Another important issue in DIS is the ratio of down quarks to up quarks, $d(x)/u(x)$, in the proton. The traditional method for measuring this ration is to assume charge symmetry and use the deuteron as a neutron target. Unfortunately, nuclear corrections introduce a large uncertainty at large x [42, 43, 44, 45]. At JLab, a number of methods have been proposed to circumvent the problem. One is to compare ^{3}He with tritium. Another, developed by the BONUS collaboration [46], is to tag the recoil proton and thereby control the expected dominant corrections. However, PVDIS from hydrogen is sensitive to $d(x)/u(x)$ and completely avoids any nuclear corrections. In particular, the

dominant term in the asymmetry is given by

$$a_1^p(x) = \left[\frac{12C_{1u}u(x) - 6C_{1d}d(x)}{4u(x) + d(x)}\right]$$

$$\sim \left[\frac{u(x) + 0.912d(x)}{u(x) + 0.25d(x)}\right]$$

Precision measurements in the range of x from 0.6 and 0.7 would be of great interest.

The fractional error in d/u is roughly twice the fractional error in A_{PV}. If the higher twist contribution to A_{PV} for the deuteron is negligible, we will also neglect higher twist for the hydrogen data. We estimate that we can obtain a 2% error on d/u over a range of x bins, with the highest having an average $x = 0.7$, in 90 days of running. The achievable precision is illustrated in Figure 2.8.

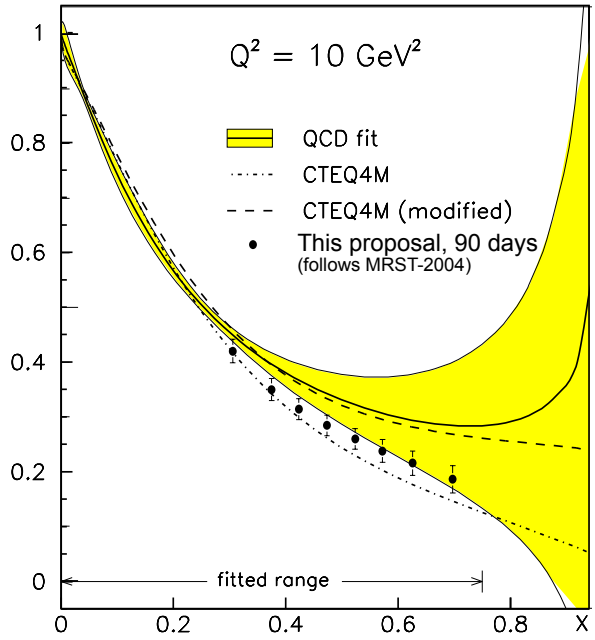

Figure 2.8: Uncertainties in d/u together with error bars corresponding to results from A_{PV} for a hydrogen target.

2.5.2 Induced Nuclear Isospin Violation

The ratio of the structure functions between complex nuclei and deuterium

$$R_{EMC}^{\gamma} = \frac{4u_A(x) + d_A(x)}{4u(x) + d(x)} \tag{2.15}$$

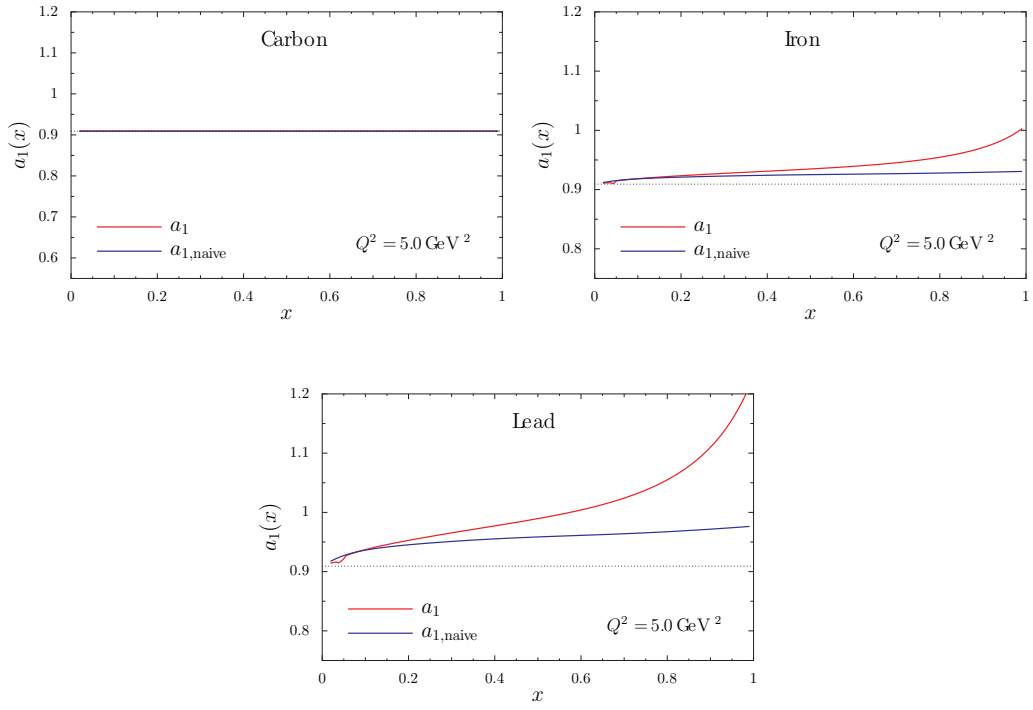

Figure 2.9: Theoretical predictions based on the NJL model described in the text for the super-ratio for various nuclei. For these calculations, there is no effect if $A = Z$.

where $u(d)_A$ is the normalized PDF for quarks in the nucleus, have been observed to depend on x. For parity violation, the PDFs are weighted differently:

$$R_{EMC}^{\gamma Z} = \frac{1.16u_A(x) + d_A(x)}{1.16u(x) + d(x)} \tag{2.16}$$

The quantity that is practical to measure is the super-ratio

$$R_{Super} = \frac{A_{PV}^A}{A_{PV}^D} = \frac{R_{EMC}^{\gamma Z}}{R_{EMC}^{\gamma Z}} \tag{2.17}$$

Assuming CSV in the deuteron, any difference between the super-ratio and unity is sensitive to a violation of the equation

$$u_A = d_A \tag{2.18}$$

or simple extrapolations for the case where $N \neq Z$. In Figure 2.9, a theoretical prediction based in the presence of a vector potential in complex nuclei [47] is displayed that suggests that the effect in Pb is about 5% at large x, large enough to be observed in our experiment. The same effect can explain a large fraction of the NuTeV anomaly. The observation of a non-unity value for R_{Super} would be clear evidence that nucleon structure is fundamentally altered in the presence of nuclear matter. A measurement of this

effect would be valuable and appears feasible in PVDIS. Although this proposal focuses on measurements with hydrogen and deuterium, this topic is mentioned as an example of further electroweak studies which would be enabled by the SoLID spectrometer.

Chapter 3

Large Acceptance Apparatus for High Luminosity

3.1 General Requirements

The main purpose of the spectrometer designed is to measure the Parity Violation effects in DIS (PVDIS) at $W > 2$ GeV, $Q^2 > 6$ GeV^2 and in a wide range of x_{Bj}, namely $0.3 < x_{Bj} < 0.8$, with an accuracy of about 1%. Since the DIS cross section drops sharply at $x_{Bj} > 0.5$ the apparatus should provide a large acceptance in that area. The acceptance may be somewhat smaller at $x_{Bj} < 0.5$. The current design aimed to maximize rates in the region $x_{Bj} > 0.55$. The useful kinematic range of the scattered electron is shown in Fig. 3.1. The spectrometer should accept the scattered electrons in a relatively narrow band in the $E' - \theta$ parameter space. The acceptance in the scattering angle θ is limited at $\theta > 18^\circ$ by the $Q^2 > 6$ GeV^2 cut. The upper limit on θ is defined by the figure of merit of the asymmetry measurement as well as the implementation limitations.

We assume a current of 50 μA at 11 GeV and 85% polarization, and use a 40 cm liquid hydrogen target to provide a luminosity of $\mathcal{L} \sim 5.4 \cdot 10^{38}$ cm^{-2}s^{-1} = 540 pb^{-1}s^{-1}.

The asymmetry to be measured (see Eq. 2.6) is $A_{PV} \sim 0.84 \cdot 10^{-4}$ GeV$^{-2} \cdot Q^2$. The figure of merit depends on the asymmetry measured and the number of detected events $\mathcal{F} = A_{PV}^2 \cdot N_{events}$. The maximum occurs at $\theta \sim 20^\circ$ (see Fig. 3.2), while at 35° the value drops by a half. Typically, there are additional limitations on the useful θ range, driven by the large background at small angles and by acceptance losses at large angles.

As a demonstration of the statistical figure-of-merit, we consider the range of

- $22^\circ < \theta < 35^\circ$;
- $x_{Bj} > 0.55$;
- $W > 2.$ GeV;

It follows:

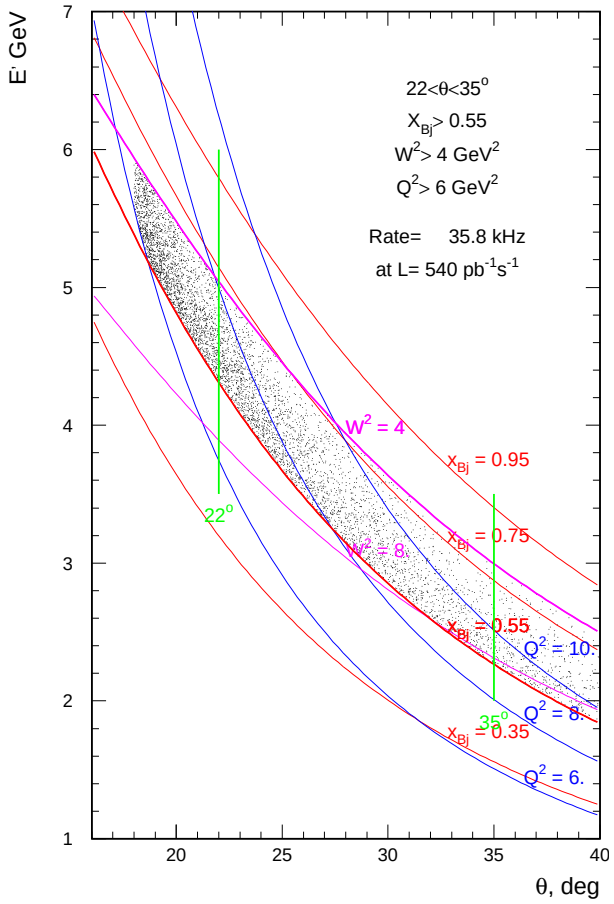

Figure 3.1: The useful kinematic range of the scattered electrons is limited by the conditions $x_{Bj} > 0.6$ from the bottom of the plot and $W > 2$ GeV from the top. The DIS events shown on the scatter plot are simulated for the 11 GeV beam. A cut off at $Q^2 > 6$ GeV^2 selects the scattered angles of $\theta > 18°$.

- $2.3 < E' < 6$ GeV
- $6 < Q^2 < 12$ GeV^2.

In order to achieve a 1% statistical accuracy on the PV asymmetry measured, one has to detect $\sim 1/(A_{PV} \cdot \mathcal{P}_{beam} \cdot 0.01)$ events.
The DIS rates at 540 pb^{-1}s^{-1}, the average asymmetries A_{PV}, and the statistics needed for a 1% measurement, are shown in Table. 3.1 for two kinematic ranges.

The requirements to the apparatus are as follows:

- running at the maximum available luminosity which, for hydrogen, is $\mathcal{L} \sim 540$ pb^{-1}s^{-1};
- the acceptance $> 50\%$ for DIS electrons in the range of interest;

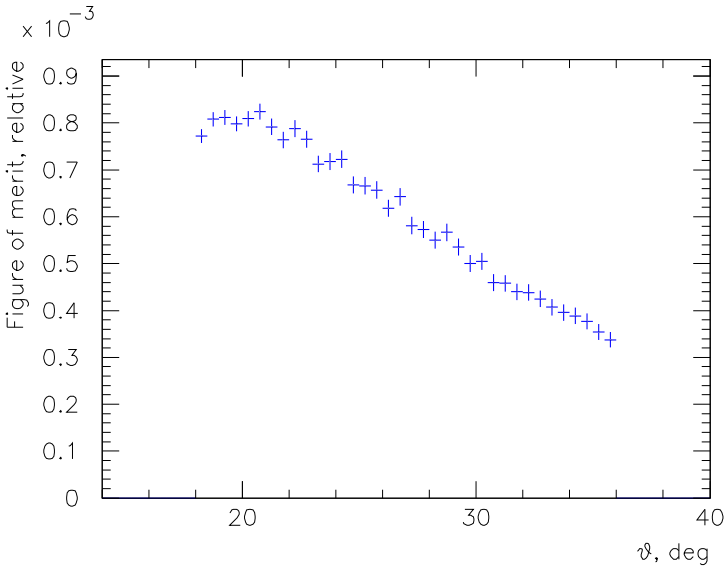

Figure 3.2: The figure of merit $\sum_{events} A_{PV}^2$ for PVDIS, depending on the scattering angle θ.

Range	Rate, kHz	$\langle A_{PV} \rangle$	events	time needed
$0.55 < x_{Bj} < 0.75$	35.0	$7.1 \cdot 10^{-4}$	$27 \cdot 10^9$	18 days
$0.65 < x_{Bj} < 0.75$	9.3	$7.8 \cdot 10^{-4}$	$23 \cdot 10^9$	60 days

Table 3.1: The DIS rates (for H_2 at 540 $pb^{-1}s^{-1}$) and PV asymmetries in the given kinematic ranges. The number of detected events shown is needed to achieve a 1% statistical accuracy. The beam time needed was estimated assuming a 100% acceptance and a 50% efficiency.

- the resolutions of $\sigma_{E'}/E' < 3\%$ and $\sigma_\theta < 4$ mrad;
- the pion contamination of the electron sample below a 1% level;
- an acceptable trigger rate;
- an acceptable background rate in the detectors.

No existing or planned device at JLab can fulfill these requirements.

These conditions require a magnetic spectrometer. The goals can not be achieved with the integrating technique, widely used for many PV experiments (see for example [3]), and the experiment must record the particle trajectories for the subsequent reconstruction of the kinematic parameters and for PID. The spectrometer must be split into > 10 independent sectors with separated triggering and readout, in order to absorb a full trigger rate up to several hundred kilohertz. In addition to the coordinate detectors,

Experiment	B, T	Bore D, m	Length, m	MJ	X_0
BaBar	1.5	2.80	3.46	27	<1.4
Cleo-II	1.5	2.90	3.80	25	2.5
CDF	1.5	2.90	5.00	30	0.85

Table 3.2: The parameters of recently used solenoidal magnets.

the spectrometer should be equipped with an electromagnetic calorimeter for the trigger and PID purposes, and a Cherenkov detector for electron identification. A gaseous Cherenkov radiator would provide the lowest background from converting soft photons. Because of the high luminosity, the detectors must be shielded from low energy electrons and photons.

Several options of magnetic spectrometers have been considered (see Appendix D). The preferred one, based on a large solenoidal magnet, is described here.

3.2 Solenoidal Spectrometer (SoLID)

3.2.1 Overview

The spectrometer described is tentatively called Solenoidal Large Intensity Device (SoLID). The target is located in the middle of a large solenoidal magnet. In order to improve the ratio of the DIS signal to various backgrounds a system of baffles has to be designed and accurately positioned between the target and the detectors.

Several solenoids with the bore diameter of about 3 m and the central field of about 1.5 T have been used in recent experiments (see Table 3.2). We plan to use one of these existing magnets. The design presented here is based on the BaBar magnet [48], but would be very similar for another magnet.

We plan to position nearly all the detector in the endcap, outside of the magnet coil, since we need space for the baffles, the gas Cherenkov detector, the coordinate detectors and the calorimeter. The layout is shown in Fig. 3.3.

The magnetic field was calculated using the 2-dimensional code *Superfish* [49] (see Fig. 3.4). The yoke includes a pocket for the detectors downstream of the magnet. A thick endcap at the upstream part would be required by possible SIDIS experiments with a polarized ^{3}He target. This target can be located just upstream of the endcap plate, which provides the required magnetic shielding. The field at the center is about 1.5 T and it drops to 0.7 T at the exit of the coil (Fig. 3.5).

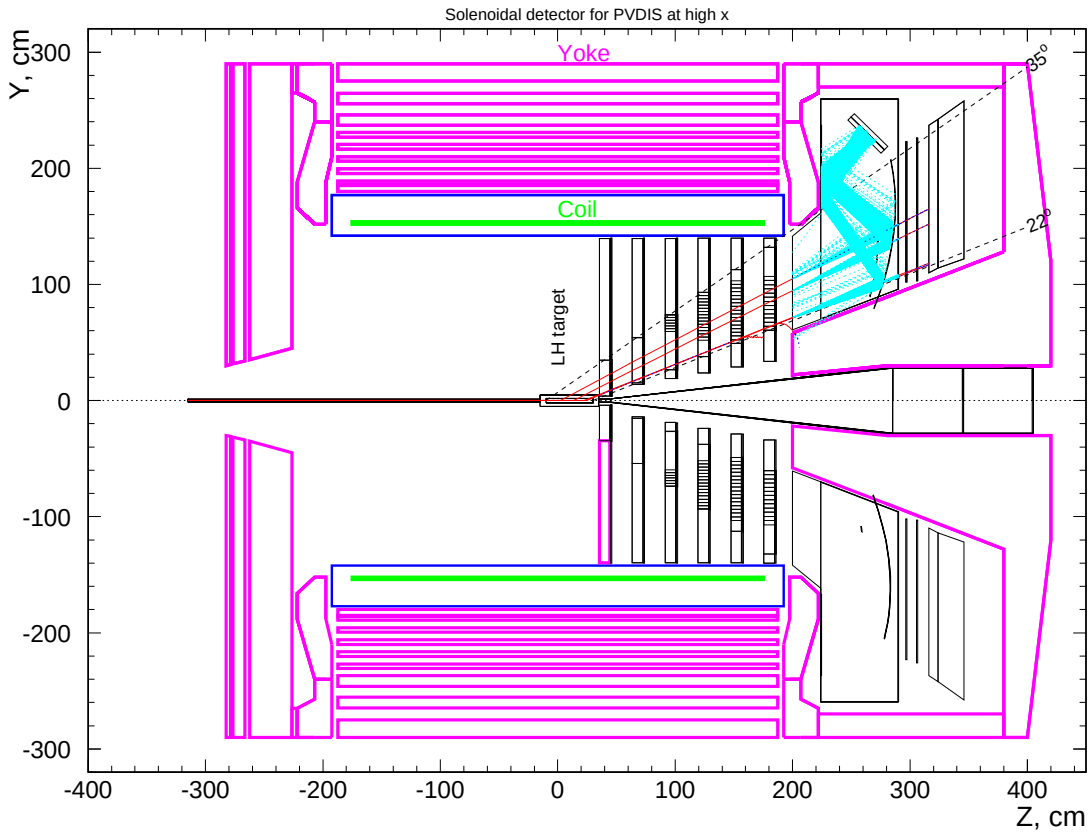

Figure 3.3: The layout of the SoLID design. The target is located close to the center of the magnet, followed by 6 wheels with the baffles. The wheels 4-6 are equipped with coordinate detectors. The gas Cherenkov is located downstream of the coil, followed by coordinate detectors and the calorimeter. A few GEANT-simulated interactions are shown, with tracks from secondary electrons and Cherenkov photons.

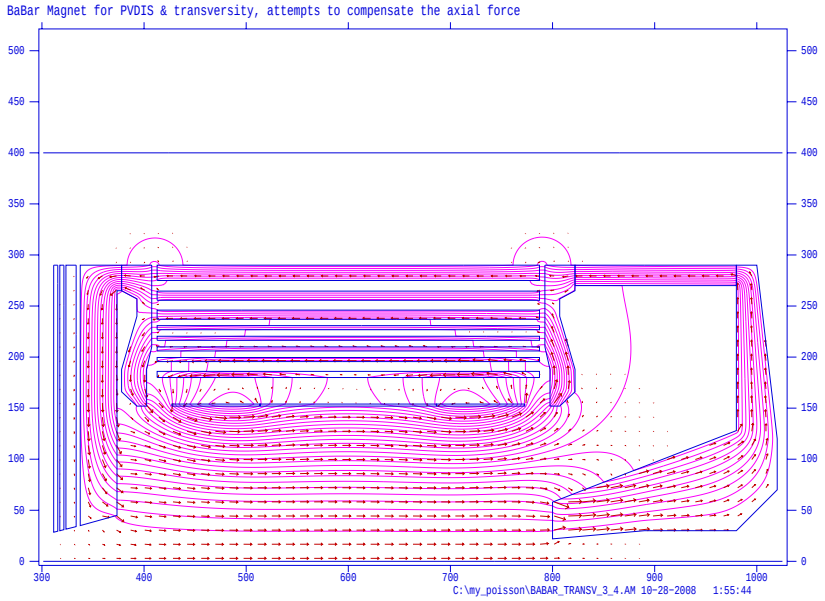

Figure 3.4: The *Superfish* [49] calculation of the magnetic field in the BaBar solenoid with a custom yoke. The barrel part of the yoke is identical to the BaBar yoke, the rest is optimized for both PVDIS and SIDIS type of experiments. The latter needs a small magnetic field in the target area, upstream of the frontal endcap. In spite of the asymmetric yoke the residual axial force on the coil is small and within the tolerance.

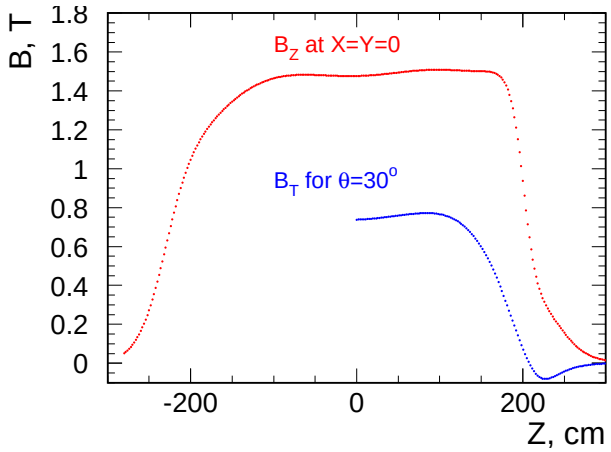

Figure 3.5: The magnetic field along the Z-axis (see also Fig. 3.4), and the field perpendicular to a particle trajectory at $\theta = 30°$.

3.2.2 Simulation

The simulation of the experiment was done with GEANT3 [50]. The interaction point was uniformly distributed over the 40 cm length of the liquid hydrogen or deuterium target, the size of the beam spot was 2×2 mm^2. The magnetic field calculated by *Superfish* was used. In order to calculate the backgrounds and the resolutions, we put in a realistic distribution of materials, including the target windows, the beam pipes etc. The setup was filled with air. The thickness of a coordinate detector plane was 0.7% of R.L., as the thickness of GEM detectors (see Section B.2). The detectors were attached to the rear sides of the baffle wheels, starting with the 4-th wheel. The 1-st detector, at the location of the highest particle flux, might be omitted at a further optimization step. For the calorimeter material, a lead-plastic sandwich was taken, with the average radiation length of 1.32 cm. The calorimeter was split into a preshower detector 8 cm thick and a shower detector 22 cm thick. Gas Cherenkov threshold detector, located at the exit of the bore, was about 1 m long, filled with C_4F_{10}. The thickness of the upstream and downstream windows was 0.2 and 0.5 mm of Al, the mirror was 3% R.L. thick.

The DIS was simulated using the MRST fit [51] for the differential cross section. The pion background was simulated using a fit to SLAC measurements [52]. The low energy background was calculated using GEANT-induced interactions of electrons with the target.

3.2.3 Spectrometer Resolution

Particle trajectories at the exit to the coil area are sufficient to define the inclusive DIS kinematics. The experiment does not rely on tracking detectors which are closer to the target inside the coil to achieve sufficient momentum and angular resolution.

The radial projections of the useful trajectories are nearly straight and provide a good enough position reconstruction of the track origin in the target. In order to estimate the momentum resolution of the setup, an empirical method was used. DIS electrons in the range of interest were simulated and traced through the setup using GEANT3 [50], with all physical processes turned off, apart from the energy loss. It was assumed that the rastered beam X-Y coordinates could be predicted to a precision of < 0.5 mm for each event, as is currently done in Hall A. Only the detectors 6 and 8 were used in the reconstruction. They were split radially in 1-2 cm intervals. For each combination of intervals $r6 - r8$, the momentum was extrapolated using a linear formula $p = \alpha_\circ + \alpha_1/\Delta\varphi(8-6) + \alpha_2 \cdot r_6 + \alpha_3 \cdot r_8$ and the scattering angle was approximated using: $\theta = \beta_\circ + \beta_1 \cdot \Delta r(8-6) + \beta_2 \cdot \Delta\varphi(8-6)$ where the parameters α, β were fit to the simulated data. The model was accurate enough to provide in the absence of multiple scattering and detector smearing a momentum resolution of 0.1% and an angular resolution of 0.1 mrad. Figure 3.6 shows the obtained energy resolution for data simulated with the multiple scattering and detector resolution included. With a reasonable detector resolution of about 0.5mm, the momentum resolution is about 2.5% while the angular resolution is about 1 mrad. The resolution of Q^2 is about 2.5%, while the x_{Bj} resolution is 0.025. The momentum is shifted on average by 2% due to the radiation losses in the

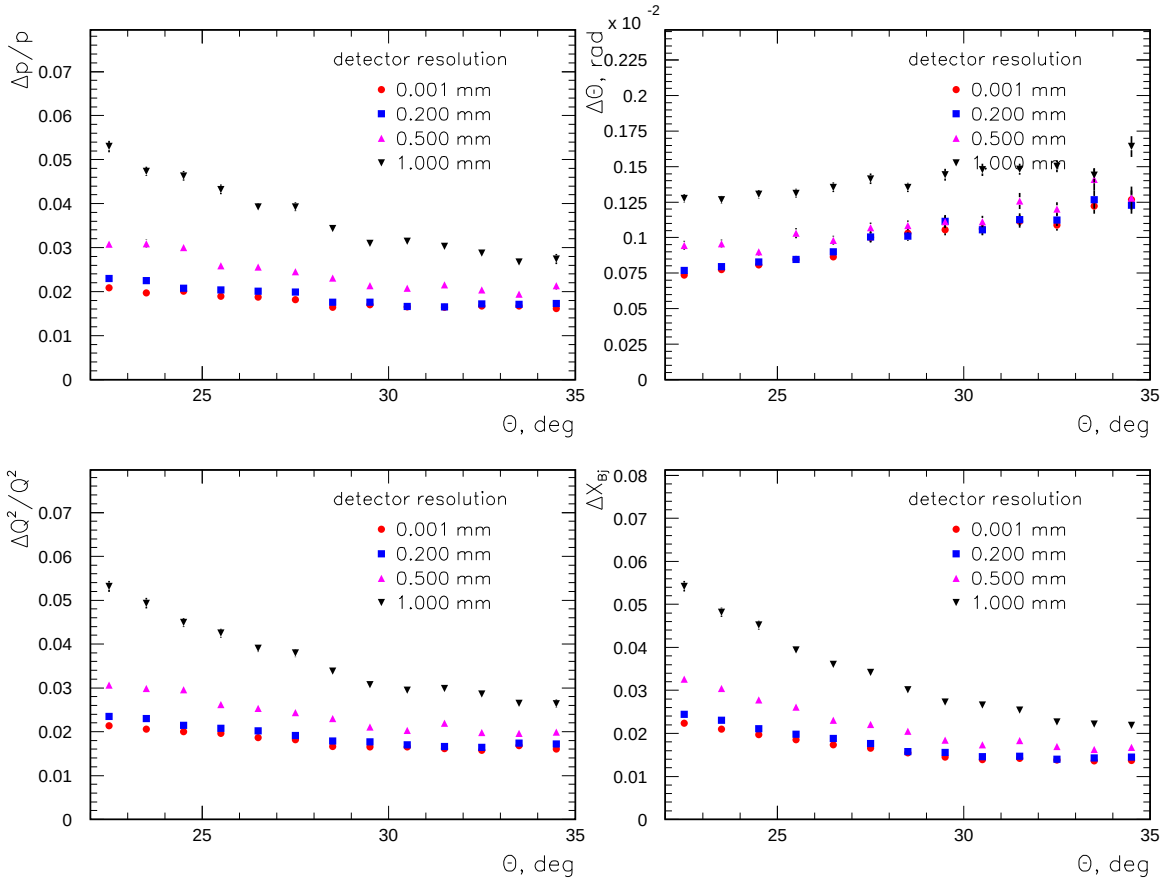

Figure 3.6: The spectrometer resolutions (RMS) in momentum p and the scattering angle θ, as well as the derived DIS variables Q^2 and x_{Bj}. The resolutions are calculated for 4 different position resolutions of the detectors.

material. The φ resolution is about 3 mrad.

3.2.4 Baffles

The solenoidal field shields the detectors from charged particles with $p < 0.3$ GeV. However, a high rate of photons coming from the target, as well as a high flux of low momentum pions $p > 0.3$ GeV, would limit the operations of the spectrometer discussed. A relatively narrow momentum spectrum of the particles of interest allows us to implement a system of baffles which would filter out both strongly bending low momentum particles and straight photons. Several disk-shaped absorbers can be inserted downstream of the target. These disks should have sets of relatively narrow slits, which form channels, shaped in order to let the useful particles produced in a certain azimuthal range $\Delta\varphi$ to pass through. The goal is to provide an overall acceptance of 30-50% of the full azimuthal coverage of 2π, for the scattered electrons in the selected range. One should try to maximize the value of $\Delta\varphi$ in order to simplify the geometry and reduce the effects

of slit scattering.

In the reference frame used the axis Z pointed along the beam. The solenoid magnetic field turned electrons toward larger values of the azimuthal angle φ. After several iterations an approximate φ range was defined, as $\Delta\varphi(\theta) = 5^\circ + 4^\circ \cdot (\theta - 22^\circ)/(35^\circ - 22^\circ)$. In total, 6 absorber disks (or wheels) were considered, located at the following Z-positions (in cm): 30. 60. 90. 120. 150. 180.

Each disk contains 30 curved slits. The slits' shape was optimized in two steps in a semi-automatic procedure. First, the GEANT-simulated tracks in the kinematic region of interest, in a defined φ range, were used to maximize the acceptance to these tracks. A small line-of-sight aperture to the target remained, allowing direct photon flux downstream of the 6^{th} baffle. The slits were adjusted to block these photons completely, with miminal cost to the useful acceptance. The baffles geometry is shown in Fig. 3.7. For the full GEANT simulation the baffles were assumed to be made of lead 9 cm thick (20 R.L.). The slits were cut just perpendicular to the surface of the disk.

Below 1.5 GeV, the baffles eliminate the electrons and reduce the pions by a factor of 20-30 (see Fig. 3.8).

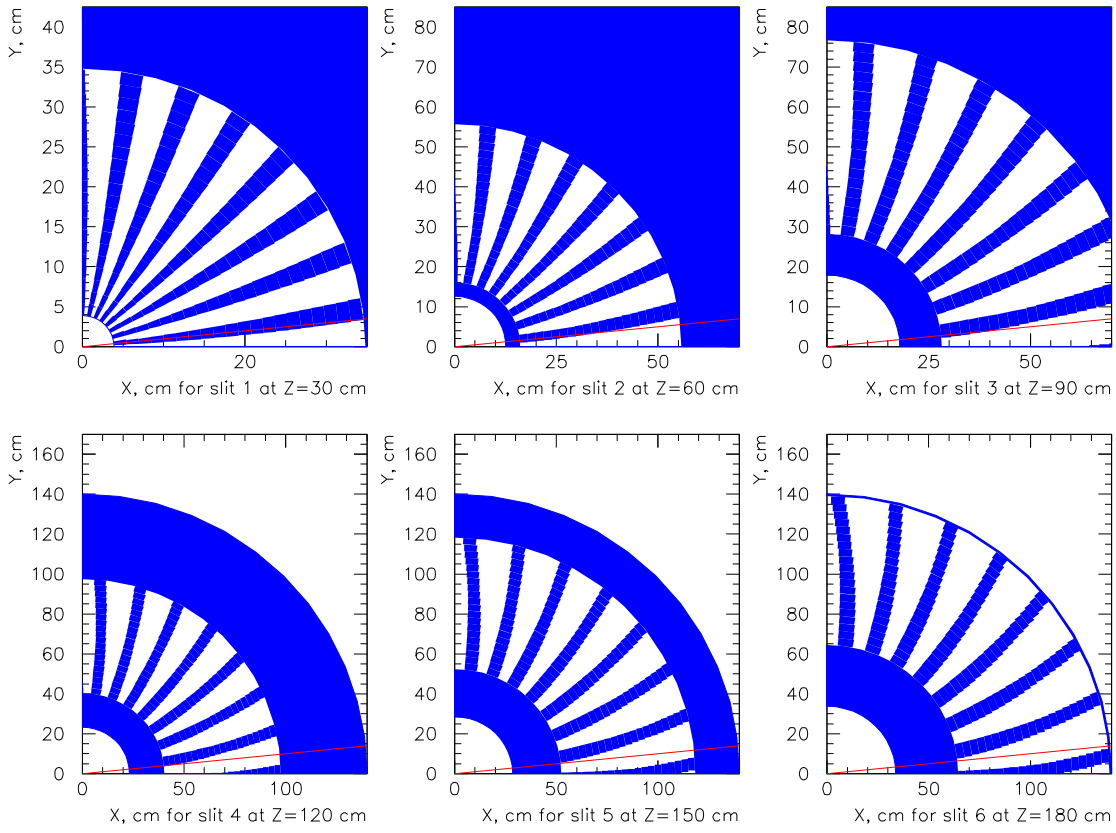

Figure 3.7: The optimized geometry of the baffles.

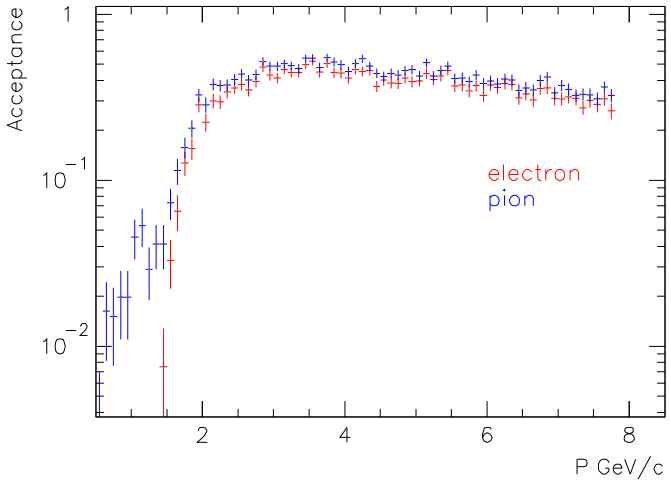

Figure 3.8: The acceptance dependence on the particle momentum for electrons and pions. The baffles reject electrons with $p < 1.5$ GeV, while pions below 1.5 GeV are reduced by a factor of 20-50.

3.2.5 Low Energy Background

The low energy background was simulated using GEANT3, for the design luminosity of 540 $pb^{-1}s^{-1}$. A realistic material distribution was implemented, including the target walls, the baffles and the detector material. The dominant backgrounds are of electromagnetic origin, which GEANT3 simulates reasonably accurately. Measurements in Hall A demonstrated that the energy flow in a calorimeter can be predicted with a 30% accuracy, while the signal rate in a wire chamber might be underestimated by a factor not more than 3. With a deuteron target, the neutron background may contribute. For the moment, the neutron background has not been simulated.

The results are presented in Fig. 3.9.

In the open geometry, the energy flow in the typical calorimeter module is about 10^7 GeV/s. For a 100 ns ADC gate it gives on average a 1 GeV energy deposit - way too high. The baffles suppress the energy flow by a factor of 15-50, to an acceptable level of 20 MeV per ADC gate.

In the open geometry the highest rate in the coordinate detectors is ~ 20 kHz/mm^2 (or < 60 kHz/mm^2, corrected for the possible systematic factor of 3 scaling of GEANT3 results). High-rate GEM detectors, have been used in a 30 kHz/mm^2 flux in experiment COMPASS [53, 54]. The baffles reduce the rate in the coordinate detectors by a factor of $\sim$10, to a level well below the COMPASS benchmark.

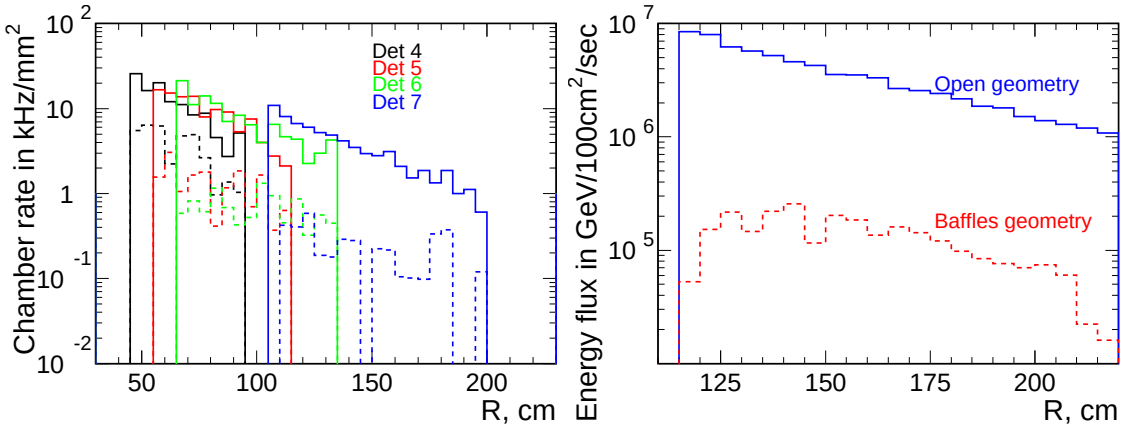

Figure 3.9: Left: the background rate in the coordinate detectors in kHz per mm^2, depending on the radius, without the baffles (the solid lines) and with the baffles (dashed lines). The baffles reduce the rate by a factor of $\sim$10 for the detectors 5-8. Right: the energy flow in the EM calorimeter in GeV/100cm^2/s, without baffles and with them. The baffles reduce the rate by a factor of 15-50.

3.2.6 Trigger Logic

Large signals produced by electrons in the calorimeter can be used for the trigger, with a threshold which is high enough to suppress the low energy background and also the

weaker signals from charged pions. The average energy of both electrons and pions are larger at smaller scattering angles, therefore it helps to make the threshold dependent on the radius of the calorimeter element (see Fig. 3.10).

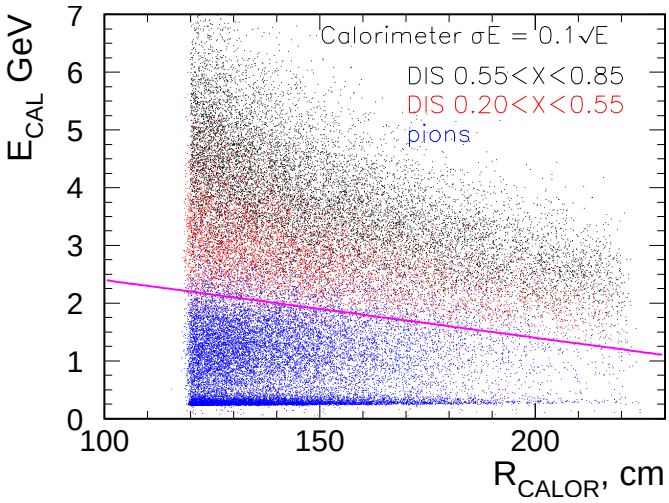

Figure 3.10: The simulated signal in the electromagnetic calorimeter, versus the radius of the hit, for DIS at $0.55 < x_{Bj} < 0.85$, DIS at $0.20 < x_{Bj} < 0.55$ and for background pions. The line indicates a threshold value, which would retain 93% of the DIS electrons accepted by the spectrometer ($x_{Bj} > 0.20$) and suppress most of the pions.

The trigger rate based on the calorimeter signals is estimated assuming a moderate calorimeter resolution of $\sigma_E/E \approx 10\%/\sqrt{E}$ for electrons. The calorimeter response to pions was simulated using GEANT3.

The threshold level shown on the plot would reject about 7% of the DIS events accepted by the spectrometer, mostly at $x_{Bj} < 0.5$. The full DIS rate accepted would be ~100 kHz. The pion rate would be reduced to 120 kHz.

With such a trigger, the expected rate per one sector will be about 7 kHz. This rate can be handled by the modern pipeline electronics.

In order to achieve the required level of pion suppression, the calorimeter has to be split longitudinally into 2 parts ("preshower" and "shower"). For the trigger purposes, the sum of both can be used.

3.2.7 Pion Background

The pion background must be suppressed, by the combination of the trigger and off-line analysis, to a ~1% level. Below 2 GeV the acceptance drops sharply for electrons (see Fig. 3.8) and slowly for pions. A reasonable off-line selection is $p > 2$ GeV[1]. The loss

[1]This selection is harder than the trigger cut shown in Fig. 3.10. The off-line cut uses a more accurate momentum measurement than the calorimeter response at the trigger level.

is about 4% of all DIS events, mostly in a range $0.3 < x_{Bj} < 0.5$. The pion to electron ratio within the acceptance (Fig. 3.11) is about 10^2 at 2 GeV.

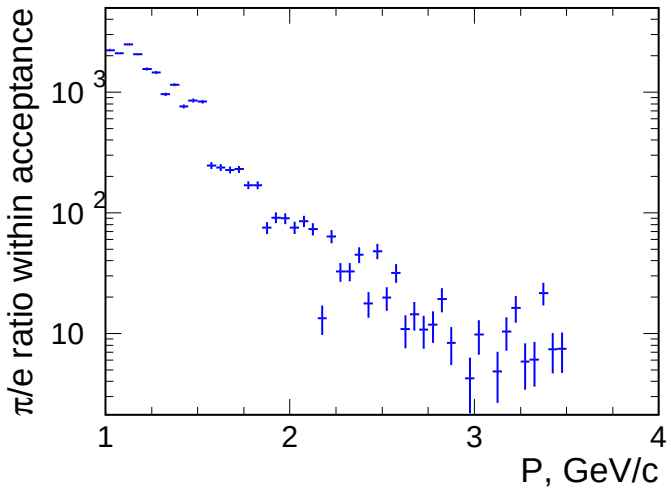

Figure 3.11: Pion to electron ratio, as a function of particle momentum for the particles within the geometric acceptance.

One can obtain a suppression factor of $\sim 2 \cdot 10^5$ [55] for pions, using an electromagnetic calorimeter and a gas Cherenkov threshold detector. The calorimeter has to be segmented longitudinally into a "preshower" and "shower" parts. With such a suppression factor the pion background would be ∼0.1% at 2 GeV and would drop at larger momenta. At $p > 3$ GeV the π/e ratio is < 10. This can be reduced to 1% with the help of the calorimeter only.

Due to low energy backgrounds, the proposed experiment will require detectors with at least the same performance, and perhaps with better timing, than the lead-glass calorimeter and the CO_2-filled, 130 cm long gas Cherenkov detector used in [55].

3.2.8 Acceptance and Rates

The $x_{Bj}-Q^2$ plot of the DIS events accepted is shown in Fig. 3.12 (left), for 11 GeV beam. The acceptance is nearly flat at $x_{Bj} > 0.5$ and drops from 37% to 25% at $x_{Bj} = 0.4$, as shown in Fig. 3.12, right. The rates calculated (see also Section 3.2.6) for hydrogen with $\mathcal{L} \sim 540$ pb^{-1}s^{-1}, under various conditions, are presented in Table 3.3. The total trigger rate is estimated to be below 220 kHz. The DIS rate in the region $x_{Bj} > 0.65$ is about 3 kHz.

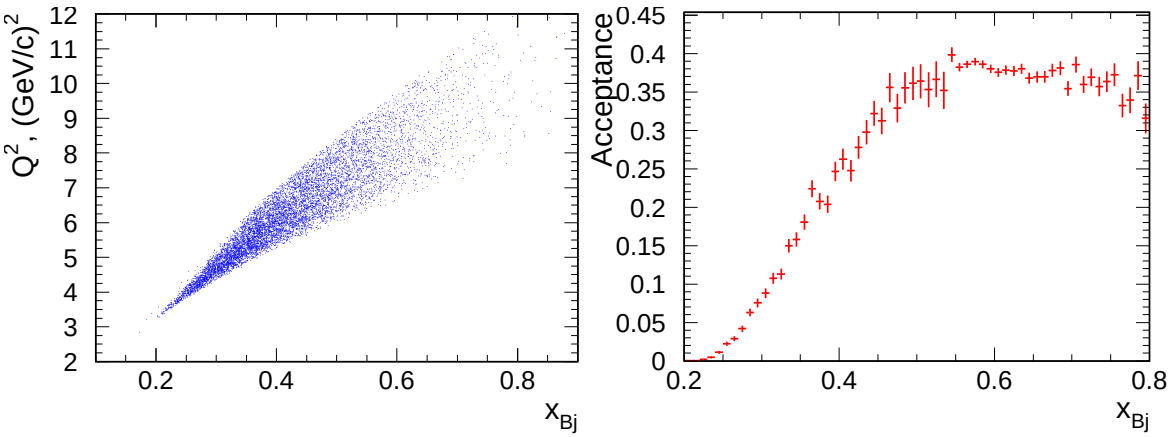

Figure 3.12: Left: the $x_{Bj} - Q^2$ plot of the accepted DIS events at $E_{beam} = 11$ GeV. Right: the acceptance dependence on x_{Bj}.

Process	Geometry	
	Open	baffles
DIS total	2500 kHz	110 kHz
DIS $W > 2$ GeV, $X > 0.20$	1500 kHz	110 kHz
DIS $W > 2$ GeV, $X > 0.55$	35 kHz	12 kHz
DIS $W > 2$ GeV, $X > 0.65$	8 kHz	3 kHz
π^- $p > 0.3$ GeV	2300 MHz	140 MHz
π^- $p > 1.0$ GeV	460 MHz	70 MHz
π^- $p > 2.0$ GeV	26 MHz	8 MHz
DIS $X > 0.20$ $E_{CALOR} > E_{thr}(R)$	680 kHz	102 kHz
π^- $E_{CALOR} > E_{thr}(R)$	540 kHz	120 kHz
π^- $E_{CALOR} > E_{thr}(R)$ pileup	$\sim$10 kHz	$<$2 kHz

Table 3.3: Calculated DIS and pion rates in the spectrometer.

3.2.9 Implementation

Possible technical solutions for the Solenoidal Large Intensity Device (SoLID) are discussed in details in Section B. For some systems robust solutions already exist. Others will require R&D, on implementing existing technologies to the particular case.

Chapter 4

Beam and Target

4.1 Beam

In this section we describe the preparation of the beam, the control of beam-related systematic errors and beam-related noise. The excellent quality of the beam at Jefferson Lab has made feasible parity experiments with much smaller asymmetries than this proposal. The random fluctuations in beam parameters are small enough to not add significant noise to the measurements. For the polarized source we have a well-developed model for controlling the laser systematics, which allows us to minimize helicity correlations in the laser beam used to produce polarized electrons. For the accelerator, we have a well-developed procedure for betatron matching that achieves maximum dampening of position differences. For the 11 GeV running we will require the upgrade of the ARC energy measurement apparatus, which is already planned.

For parity experiments, the physical properties of the beam need to be identical for the left- and right-handed beams to a very high degree so as to minimize spurious asymmetries. The helicity-correlated intensity asymmetry will be maintained to be less than 1 ppm by an active feedback loop. The physical properties of the electron beam will be monitored with high precision by beam monitors, both stripline and cavity monitors. A luminosity monitor downstream of the target will monitor target density fluctuations, which are not expected to be a problem for this proposal. Although the main DAQ for this experiment is a counting-mode DAQ, for the purposes of studying helicity-correlated beam properties, the beam monitors and possibly other detectors could be simultaneouosly read out by the existing HAPPEX DAQ which integrates over the helicity period.

At the polarized source, a GaAs photocathode is optically pumped by circularly polarized laser light to produce polarized electrons, with the ability to rapidly and randomly flip the sign of the electron beam polarization. The asymmetry is extracted by generating the incident electron beam as a pseudorandom time sequence of helicity "windows" at 30 Hz and then measuring the fractional difference in the integrated scattered flux over window pairs of opposite helicity.

The electron beam polarization will be measured by Møller scattering and Compton scattering (section 5.3).

To measure the sensitivity of the scattered flux to beam parameters we may combine our counting-mode DAQ for the detectors with the integrating-mode DAQ for beamline elements, and we may spend a fraction of our beam time ($\sim 2\%$) making modulations of beam parameters by modulating corrector coils in the beam line leading to the target, as well as a klystron which modulates energy.

To measure the beam intensity, microwave cavity BCMs have been developed at Jefferson Lab. The precision that has been achieved for a 30 ms beam window at 100 μA is 4×10^{-5}. This superior resolution is a result of the high quality of the JLab beam, the good radiofrequency (rf) instrumentation, as well as a custom high resolution ADCs. During the 2005 HAPPEX run we achieved helicity correlated position differences averaged over 1-month at the $\sim$1 nanometer level. These performances are more than adequate for this proposal.

4.2 Target

For this proposal we plan to build 40-cm long cyrogenic liquid hydrogen and deuterium targets. Jefferson Lab has extensive experience with cyrogenic targets, although they are normally 20 to 25 cm long. The two available designs of the cryotarget cell which can fulfill our requirements are a racetrack-shaped (as used in HAPPEX-II) and cylindrical a ("cigar-tube") cells. Racetrack cells have much better cooling flow and thus have proved to be more suitable to avoid boiling effects. However, due to our low rates the boiling effects are not expected to be a problem, as explained further below.

For the 6 GeV PVDIS experiment, expected to run in the Fall of 2009, will use a 25-cm LD_2 target with 100 μA. The main change for this proposal is a longer cell, 40-cm, which at 50 μA beam current would require 25% more cooling capacity. An increase in cooling capacity is already foreseen for the lab. For example, the Qweak experiment will run with 180μA on a 35-cm LH_2 target.

The endcaps of a typical target cell at JLab are made of 10 mil aluminum (AL 7075-T6). For the G0 experiment, a special cell was made with Al endcaps 5 mils thick. This will be sufficient for this experiment to maintain an acceptable level of background. The background ratio from endcaps will be measured in the standard way using an empty target with the same endcaps as the target cells, a "dummy" cell. The radiation length of the thick dummy cell will be made the same as the cryogenic cells so that radiative losses are similar. The asymmetry of $\vec{e}-$Al DIS could be somewhat different from A_d or A_h. We plan to measure the $\vec{e}-$Al DIS asymmetry during the approved 6 GeV PVDIS experiment. If necessary this asymmetry could also be measured during this experiment using an empty target with thick Al endcaps,

Target boiling effects are not expected to be a problem for this experiment because the statistical accuracy in a given helicity period is much larger than the expected noise from boiling. There are two effects commonly termed "target boiling". One is due to a phase change in the liquid which reduces the rate; this should be less than 5% for this experiment. The second meaning of "target boiling" which is more relevant for parity-violation, is pulse-to-pulse density fluctuations induced by beam parameters such

as spot size. This causes noise in the measured asymmetry. Based on the experience with cryogenic targets at JLab we don't expect the noise to be significant compared to counting statistics. A luminosity monitor placed downstream is commonly used to monitor the density fluctuation noise.

The hydrogen target may become polarized in the magnetic field of the solenoid. This would cause an asymmetry unrelated to the weak interaction physics of the experiment. The strategy for depolarizing the targets may be different for the two targets because of their different spin relaxation timescales. For the deuterium target we may use an RF depolarizer, while for the hydrogen the plan would be to start with relatively pure para-hydrogen. Catalysis by interaction with surface materials in the target loop might also help depolarize the hydrogen target. Small residual polarizations that may remain can be cancelled by flipping the polarity of the field in some running periods.

Chapter 5

Systematic Corrections

5.1 Kinematic Reconstruction

In order to reconstruct the kinematic quantities of interest, i.e. Q^2, x_{Bj}, etc, we will need precise measurements of the beam energy E_b, the scattering angle θ and the final-state energy E' as well as having good PID for the scattered particle. The PID is provided by the electromagnetic calorimeter (ECAL) shower and preshower data combined with the Cherenkov detector data.

The general strategy is to rely on the excellent knowledge of E_b and to calibrate the apparatus with elastic scattering. The scattering angle may be reconstructed with ~ 0.5 mrad accuracy using the high-resolution GEM tracking information and precise measurements of the detector positions. We plan to map out the magnetic field in the tracking area, for the momentum reconstruction. Additionally, we plan to use the elastic scattering off hydrogen at beam energies of 4.4 and 6.6 GeV to calibrate the measurements of the momentum and Q^2. With the expected spectrometer resolution, at 4.4 GeV the elastic peak will be separated from the inelastic background, with a contamination from the latter of about 5%. At 6.6 GeV the contamination will be about 25%. Since the expected rate at the full luminosity will be high (50 kHz at 4.4 GeV and 4 kHz at 6.6 GeV) further optimization of the calibration conditions are possible, for example using thinner targets or running at a low current. Comparing the elastic peaks at two beam energies will allow to cross-check both the momentum and the angle scales, and calibrate the Q^2 measurement to a 0.2% accuracy.

Several options exist to increase the accuracy further. They will be considered at the next stage of development. For a better selection of the elastic events one can detect the recoil proton, which, for the given electron kinematics, mostly stays within the acceptance of the spectrometer. For this, we will need to be able to rotate the baffle wheels in order to allow positively charged particles to come through. Another possibility is to make calibration runs without the baffles, and at much lower luminosity. Note that the beam position and current monitors are already being upgraded to achieve good accuracy (better than 0.1 mm in position) at very low currents (down to 0.1 nA).

Measurements of beam energy E_b to better than 10^{-3} accuracy are routine at JLab,

and with the upgrade of the ARC energy measurement apparatus for the 11 GeV era, which is already foreseen in Hall A, we should continue to have this accuracy.

The ECAL can be initially calibrated with the elastic scattering on hydrogen, and then continuously monitored and recalibrated using the main data set of DIS electrons and the momentum reconstruction by the spectrometer.

5.2 Radiative Corrections

5.2.1 Electromagnetic (EM) Radiative Correction

In the scattering process both the incident and the scattered electrons can emit photons, and the kinematics (Q^2, W) at the reaction vertex is different from that reconstructed from the beam energy and the measured momentum and angle of the scattered electron. Consequently, when we extract cross sections and asymmetries from the measured values there are electromagnetic radiative corrections to be made. The theory for the EM radiative corrections is well developed [56] and the corrections can in principle be calculated. However, an uncertainty to this correction arises from the uncertainty of the input structure functions, in particular those from the resonance regions.

Figure 5.1 shows the region of covered Q^2 and W for the reconstructed kinematics of events in the acceptance (blue), and the region containing the true vertex kinematics for those events (red). About 10% of events will come from the resonance region due to internal and external Bremsstrahlung. We anticipate that A/Q^2 will be roughly constant everywhere. However, the Q^2 and the effective initial state polarization are altered for radiative processes. The size of the full radiative correction can be as large as 6% of the measured asymmetry. To limit the uncertainty of EM radiative corrections to a tolerable level, we plan to measure the PV asymmetry in the lower W and Q^2 region using lower beam energies. Using about 10% of the DIS production time, the error on the radative corrections can be limited to an acceptable ($< 0.3\%$) level.

5.2.2 Electroweak Radiative Correction

The products of weak charges $C_{1,2u(d)}$ given by Eq. (2.2-2.5) are valid only for the case in which there is no electroweak radiative correction. With this correction they are given by

$$C_{1u} = \rho'[-\frac{1}{2} + \frac{4}{3}\kappa' \sin^2(\theta_W)] + \lambda_{1u} \quad (5.1)$$

$$C_{1d} = \rho'[\frac{1}{2} - \frac{2}{3}\kappa' \sin^2(\theta_W)] + \lambda_{1d} \quad (5.2)$$

$$C_{2u} = \rho[-\frac{1}{2} + 2\kappa \sin^2(\theta_W)] + \lambda_{2u} \quad (5.3)$$

$$C_{2d} = \rho[\frac{1}{2} - 2\kappa \sin^2(\theta_W)] + \lambda_{1d} \quad (5.4)$$

Figure 5.1: Region of phase space containing the vertex kinematics (red) compared to that covered by the reconstructed kinematics (blue) for the proposed measurement.

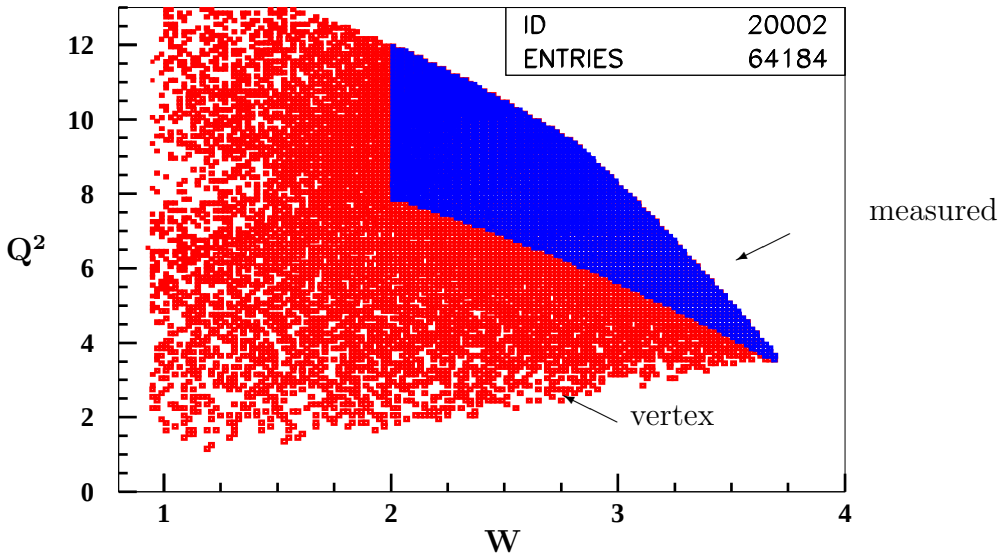

The electroweak radiative correction is well determined in the Standard Model. Standard Model electroweak radiative corrections to $C_{1,2u(d)}$ have been calculated [57] and are relatively small. The corrections modify the ρ, κ, and λ parameters from their tree level values $\rho - \rho' = \kappa = \kappa' = 1$ and $\lambda_{1u} = \lambda_{1d} = \lambda_{2u} = \lambda_{2d} = 0$. A recent evaluation [58, 59] gives $\rho' = 0.9881$, $\kappa' = 1.0027$, $\rho = 1.0011$, $\kappa = 1.0300$, $\lambda_{1d} = -2\lambda_{1u} = 3.7 \times 10^{-5}$, $\lambda_{2u} = -0.0121$, $\lambda_{2d} = 0.0026$. Also $\sin^2\theta_W = 0.2312$, where we are using the $\overline{MS}$ scheme.

The above values are computed for $Q^2 = 0$. We are presently calculating the Q^2-dependent terms. We anticipate that the changes, although critical at the proposed level of precision, will be smaller in size than those for Møller scattering.

5.3 Polarimetry

The experiment requires a relative accuracy of the electron beam polarization measurement at the level of ∼0.4%. A comparable level of accuracy has been previously achived by the SLD collaboration [60], using a Compton polarimeter with a ∼ 46 GeV pulsed beam at SLAC. JLab has accumulated extensive experience with polarimetry below 6 GeV, and presently boasts two separate polarimeters with quoted accuracies at or near the 1% level. However, these polarimeters have never been cross-checked with each other at this level of precision, nor has any experiment yet matched this level of precision on a beam polarization observable.

The prospects for improving polarimetery at JLab to the necessary level are good. Upcoming experiments in the JLab "6 GeV" program, in both Halls A and C, require 1% polarimetry [61,62,14,63]. These requirements will lead to the upgrade of the Hall A Compton polarimeter, the development of a Hall C Compton polarimeter and improvements to existing Moller polarimeters which use ferromagnetic foil targets. These 6 GeV experiments will be an excellent introductory challenge to very high-accuracy polarimetry at JLab, and should sharpen techniques both in controlling systematic uncertainties and in cross-comparing high-precision polarimeters.

In order to reach a robust 0.4% accuracy, we propose to develop two separate, continuous polarimeters for the current proposal, each independently normalized to that level of accuracy. Each polarimeter should provide a 0.4% statistical precision in comparable time periods of not more than several hours, in order to facilitate cross-checks and systematic studies. This redundancy, both in the measurement and monitoring of the beam polarization, will provide a new benchmark in precision electron beam polarimetry. We discuss both polarimeters in extensive detail in Sec. C.2 and Sec. C.1.

Chapter 6

Concluding Remarks

6.1 Collaboration

The collaboration is quite diverse, including experts of precise parity experiments such as Qweak, G_0, HAPPEX, SLAC E158. We also have groups with the experience to develop and build the necessary hardware. Theoretical support for PVDIS is being provided by collaborators J. Erler and M. Ramsey-Musolf.

6.2 Synergy with Other Proposals

There is significant overlap between the PVDIS and Moller experimental collaborations. This ensures ample expertise in the special issues related to parity experiments. The polarimeters will be shared by both experiments. Since the total fractional error for PVDIS is 0.6%, the demands on polarimetry are more severe. However, since the Møller experiment needs to be strictly statistics limited, our specified precision of 0.4% is very useful for them.

The SIDIS collaboration is also submitting a proposal using the solenoid to make coincidence measurements with a polarized ^{3}He target. While there are significant differences in the configurations for PVDIS and SIDIS, much of the hardware is shared. If both proposals are approved, we plan to work closely together on both experiments.

6.3 Beam Request

For the deuterium data, we have based our sensitivity on 180 days of production running at 50 μA, with 1/3 of the data at 6.6 GeV and the rest at 11 GeV. Approximately 27 additional days, run at various currents, will be required for checkout and calibrations. An additional 18 days will be required at 4.4 GeV and 50 μA for radiative correction measurements. The total beam request at all energies for the deuterium measurement is 225 days, with about 25 of those days run mostly at reduced beam currents.

For the hydrogen meausrement, 90 days are needed for production data at 11 GeV, about 9 days are required at 4.4 GeV to control radiative corrections and another 14 days will be required for calibration. The running time requested for hydrogen totals to 113 days.

In the future, we would also anticipate requesting an additional comparable run for a heavy nucleus such as Pb.

6.4 Cost and Schedule

We are preparing a preliminary cost estimate for the project. However, it is already clear that significant funds will be required from several agencies. We plan to seek funding from the US DOE, NSF, and international sources. As emphasized earlier, this project has been listed in the Fundamental Symmetries initiative in the NSAC Long Range Plan, and has been included in the Plan's 10 year funding profile.

Assuming that we receive the endorsement of the JLab PAC, we will request a technical review by the end of 2009 so that we can start seeking funding from the agencies early in 2010. The goal is to start construction by 2012 and schedule installation for 2015.

6.5 Assignment of Tasks

We list below key subsystems and institutions who are interested in design, construction and implementation of them. Note that these are not firm or binding responsibilities, but simply the current thinking of the collaboration given each institution's current interests and past experience. As emphasized earlier, we expect the collaboration to expand should we receive PAC approval.

- **Polarized source:** *UVa, JLab*
- **Cryo Target:** *JLab, MissSt*
- **Magnet:** *UMass, JLab, MIT, ANL*
- **Baffles:** *Longwood*
- **Tracking Detectors:** *UVa, Seoul Nat'l, Kentucky, William and Mary, MissSt, China Collaboration (USTC, Beijing, China IAE, Lanzhou, Tsinghua, Huangshan)*
- **Gas Cerenkov:** *Temple, ANL, Ohio*
- **Shower:** *William and Mary, Syracuse, UMass, Rutgers, VaTech*
- **Electronics:** *JLab*
- **Polarimetry:** *UVa, Syracuse, JLab, CMU, ANL, MissSt*
- **Data Acquisition:** *UVa, JLab, LANL, Ohio, LaTech*
- **Simulations:** *Longwood, JLab, UVa, LaTech*

Appendix A

Physics

A.1 DIS Phenomenology

In order to make a precise comparison of the data with theory, a more careful treatment of the asymmetry must be used [1]. The cross section can be written formally in terms of products of hadronic and leptonic tensors.

$$\frac{d^2\sigma}{d\Omega de'} = \frac{\alpha^2}{Q^4}\frac{E'}{E}\left(L^{\gamma}_{\mu\nu}W^{\mu\nu}_{\gamma} + \frac{G_F}{4\sqrt{2}\pi\alpha}L^{\gamma Z}_{\mu\nu}W^{\mu\nu}_{\gamma Z}\right)$$

The lepton tensor for the interference term is related to the electromagnetic lepton tensor

$$L^{\gamma}_{\mu\nu} = 2(l_\mu l'_\nu + l'_\mu l_\nu - l\cdot l' g_{\mu\nu} + i\lambda\varepsilon_{\mu\nu\alpha\beta}l^\alpha l'^\beta)$$

by

$$L^{\gamma Z}_{\mu\nu} = (g^e_V + \lambda g^e_A)L^{\gamma}_{\mu\nu}$$

where λ is 1 (-1) for positive (negative) helicity of the initial lepton beam.

For the hadronic tensors, we can write

$$W^{\gamma(\gamma Z)}_{\mu\nu} = \frac{1}{2M}\sum_X\{\langle X|J^{\gamma(Z)}_\mu|N\rangle^*\langle X|J^{\gamma}_\mu|N\rangle$$

$$+ \langle X|J^{\gamma}_\mu|N\rangle^*\langle X|J^{\gamma(Z)}_\mu|N\rangle\}(2\pi)^2\delta(P_X - p - q) \tag{A.1}$$

where $J^{\gamma(Z)}_\mu$ is the hadronic electromagnetic (weak) current and M is the nucleon mass, and N is the target nucleus.

For unpolarized targets, the hadronic current can be decomposed into three structure functions F^j_i where $i = \gamma$ is the purely electromagnetic tensor and $j = \gamma Z$ is the interference tensor:

$$W^j_{\mu\nu} = -\frac{g_{\mu\nu}}{M}F^j_1 + \frac{p_\mu p_\nu}{Mp\cdot q}F^j_2 + \frac{i\varepsilon_{\mu\nu\alpha\beta}p^\alpha p^\beta}{2Mp\cdot q}F^j_3$$

The F^j_i are fucntions of x and Q^2 only. They do not depend on y.

In the QPM, the Callan-Gross relation $F_2^j = 2xF_1^j$ holds, but for our kinematics, this is a poor approximation. The violation is usually expressed in terms of the ratio R^j defined by

$$R^{\gamma(\gamma Z)} \equiv \frac{\sigma_L^{\gamma(\gamma Z)}}{\sigma_T^{\gamma(\gamma Z)}} = r^2 \frac{F_2^{\gamma(\gamma Z)}}{F_1^{\gamma(\gamma Z)}} - 1$$

where

$$r^2 = 1 + \frac{Q^2}{\nu} = 1 + \frac{4M^2x^2}{Q^2} \tag{A.2}$$

The parity-violating asymmetry in terms of the structure functions is given by

$$A^{PV} = -\left(\frac{G_F Q^2}{4\sqrt{2}\pi\alpha}\right) \frac{g_A^e(2xyF_1^{\gamma Z} - 2[1 - 1/y + xM/E]F_2^{\gamma Z} + g_V^e x(2-y)F_3^{\gamma Z}}{2xyF_1^{\gamma} - 2[1 - 1/y + xM/E]F_2^{\gamma}}$$

Then the asymmetry in full generality may be written

$$A^{PV} = -\left(\frac{G_F Q^2}{4\sqrt{2}\pi\alpha}\right) \left[g_A^e Y_1 \frac{F_1^{\gamma Z}}{F_1^{\gamma}} + \frac{g_V^e}{2} Y_3 \frac{F_3^{\gamma Z}}{F_1^{\gamma}}\right] \tag{A.3}$$

The Y_i are functions of y and R:

$$Y_1 = \frac{1 + (1-y)^2 - y^2(1 - r^2/(1+R^{\gamma Z})) - 2xyM/E}{1 + (1-y)^2 - y^2(1 - r^2/(1+R^{\gamma})) - 2xyM/E} \left(\frac{1+R^{\gamma Z}}{1+R^{\gamma}}\right) \tag{A.4}$$

$$Y_3 = \frac{1 - (1-y)^2}{1 + (1-y)^2 - y^2(1 - r^2/(1+R^{\gamma})) - 2xyM/E} \left(\frac{r^2}{1+R^{\gamma}}\right) \tag{A.5}$$

In the QPM, the structure functions are given by

$$F_1^{\gamma} = \frac{1}{2}\sum_i Q_i^2(f_i(x) + \overline{f}_i(x)); \quad F_2^{\gamma} = 2xF_1^{\gamma}$$

$$F_1^{\gamma Z} = \sum_i Q_i g_V^i(F_i(x) + \overline{f}_i(x)); \quad F_2^{\gamma Z} = 2xF_1^{\gamma Z}$$

$$F_3^{\gamma Z} = 2\sum_i Q_i g_A^i(f_i(x) - \overline{f}_i(x))$$

In this limit, where $R = 0$, and also in the limit $M \to 0$, Equation A.3 for deuterium reduces to Equations 2.6, 2.7, and 2.8.

Appendix B

Detector Implementation for SoLID

B.1 Solenoidal Magnet

We based our design on the properties of the BaBar magnet. The results can be partly applied to other similar magnets, as one from CLEO-II. The biggest difference is in the sizes and construction details of the yokes.

The BaBar magnet [64, 65, 66] (see Fig. B.1) contains an aluminium stabilized, thin superconducting solenoid and a return yoke, providing an axial central field of 1.5 T.

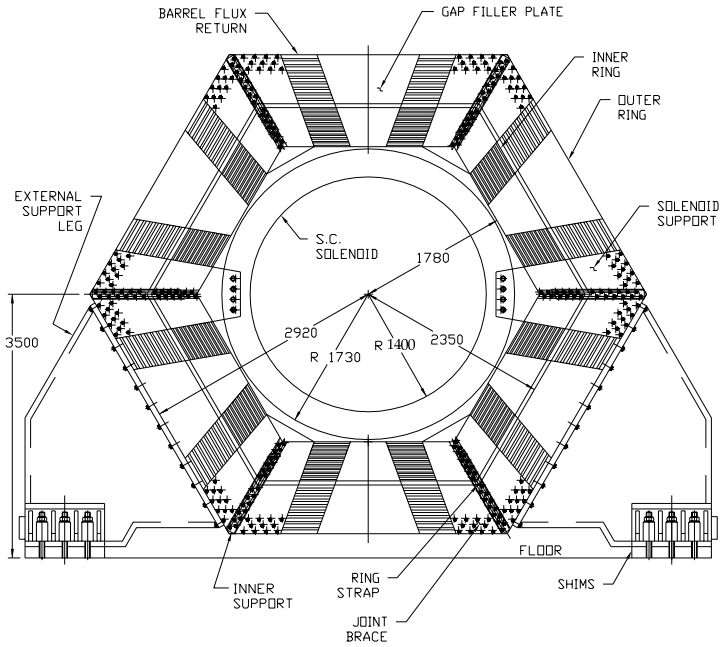

Figure B.1: BaBar magnet layout, taken from [66].

The winding is supported by an aluminium alloy outer cylinder, which provides hoop strength to the coil. The coil has dimensions of 3 m in diameter and 3.7 m in length.

The current density is graded to meet the field uniformity requirements of 2%. The coil is indirectly cooled to 4.5 K using the liquid helium thermo-siphon technique and cooling channels welded to the support cylinder. Automatic cooldown and cryogen supply to the coil and its 40 K radiation shield is done by a helium liquefier/refrigerator via coaxial, return gas screened, flexible transfer lines. A hexagonal flux return, comprised of a barrel and two end doors provides the external flux path for the field. To accommodate the muon detectors, the barrel and end caps are segmented into 20 plates of different thickness. The gaps between the plates are about 3 cm wide.

The solenoid center is 3.500 m above the floor. In Hall A, the beam is 10 ft, or 3.048 m above the floor. It is shown in Fig. B.1 that the distance from the center of the magnet to the bottom plate of the barrel yoke is 2.920 m. Therefore, if the four support pieces of the barrel are modified or rebuilt, one can provide a clearence of ∼12 cm between the bottom plate and the floor. The endcaps can slide transversally on their own supports.

The coil and the thermostat construction limits the integral axial force on the coil to about 35 t. The proposed design of the customized yoke, although asymmetric in Z, provides an acceptable residual force. The result from our preliminary, 2-dimensional calculations is about 2 t.

The optimal solution for the yoke still has to be evaluated, taking into account the costs for adapting various parts of the existing yoke against manufacturing new customized parts.

B.2 Coordinate Detectors

We number the potential locations for the coordinate detectors from 1 to 8. The first 6 locations are just downstream of the 6 wheels with the baffles. The positions 7-8 are downstream of the Cherenkov detector. As we have discussed in Section 3.2.3, 2 measured space points on the trajectories at the locations 6 and 8 (see Fig. 3.3) are sufficient to find the track parameters. The calorimeter measurement of the shower centroid adds another point, with a spatial accuracy of ∼10 mm. For good pattern recognition in a high rate environment at least three space points with a good resolution must be measured. No detailed optimization of the detector arrangement has been done so far. Tentatively, we plan to install the detectors at the locations 5,6,7 and 8. In each location the space point is measured. With not more than one point missing due to inefficiencies, and with a point in the calorimeter, it should provide enough information for the pattern recognition, since the trajectories are nearly straight in this area.

The hit patterns and the detector arrangements are shown in Fig. B.2.

The radial distribution of the low energy background in the system with the baffles is nearly flat (Fig. 3.9). The rate expected from GEANT3 calculations is shown in Table B.1. The rates were increased by a factor of 3 in comparison with Fig. 3.9 in order compensate for possible underestimation of the low energy photons. Only micropattern detectors such as GEM [53,54] or MICROMEGAS [67] can handle the hit densities at the locations 5 and 6. For the locations 7-8 one may consider using straw detectors similar

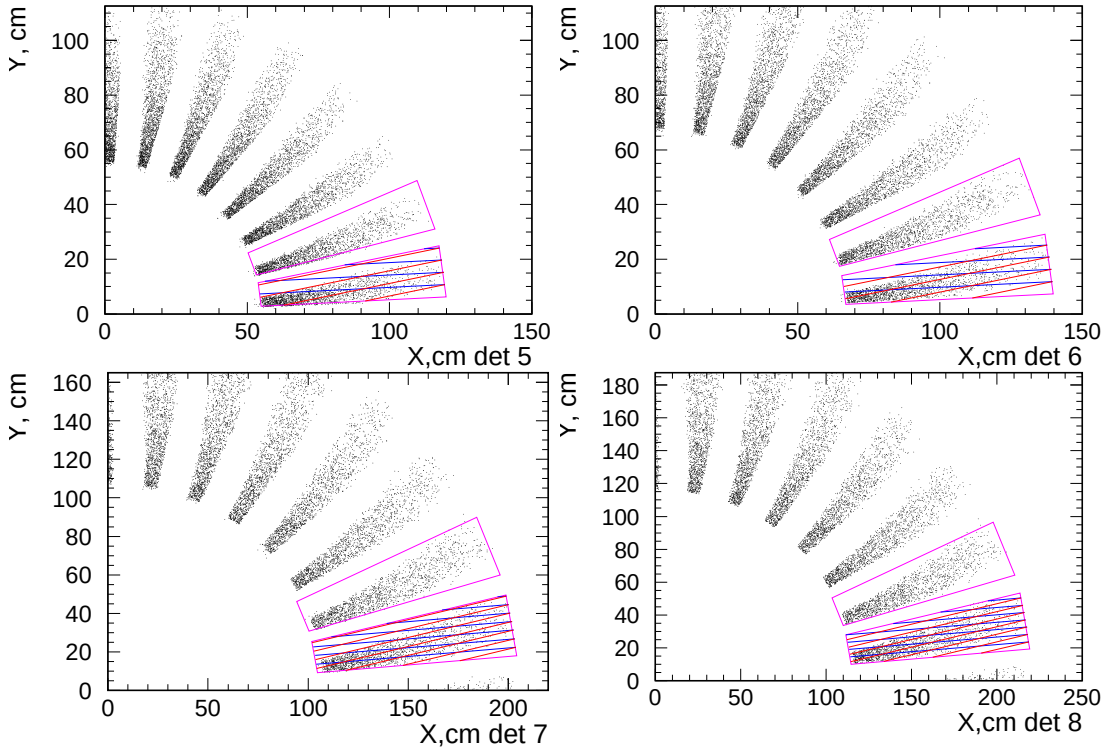

Figure B.2: The electron hit pattern in the locations 5-8, reflecting the geometry of the baffles with its 12°-pitch. The contours of detector segments are shown, along with possible directions of the anode wires or readout stripes. The angle between two readout directions depends on the width of one sector, which may be selected in a range of 9-12°, depending on the plane.

to the TR tracker [68] of the ATLAS experiment. That straws have a 4 mm diameter and should be operational at a rate up to 20 MHz per straw.

The GEM detectors are used with 2-dimensional readouts. The induction electrode contains two sets of stripes or pads, insulated from each other. Various geometries have

Location	Max rate			accidentals	Space points
	per sector	per mm^2	per 0.4 mm strip	per 40 ns	per event
5	250 MHz	6.0 kHz	2.5 MHz	10.0	20.0
6	190 MHz	2.0 kHz	1.6 MHz	7.6	11.0
7	110 MHz	1.0 kHz	0.6 MHz	4.4	3.9

Table B.1: The background rates in the coordinate detectors. The rates predicted by GEANT3 were multiplied by a factor of 3 in order to compensate for possible underestimation of low energy photons. The last column shows the number of space points in a useful event, obtained with a GEM detector with the 2-dimensional readout.

been tested, with the angle between the stripes (U-V) from 5° [69] to 90° [54]. The amplitude correlation of the signals from the two planes can suppress the false U-V combinations by a factor of ∼5, reducing the number of planes and projections needed for the pattern recognition.

Assuming that each of 4 detector planes consists of 30 GEM sectors 10° wide, with stripes made along the sector sides (see Fig. B.2), we end up with a stereo angle of 10°.

Table B.1 indicates that the pattern recognition would start with about 850 potential trajectories - combinations of space points in 3 planes. Due to a weak dependence of the background distribution with the radius, we assume that the detector plane is uniformly populated with false spatial points. Just considering the radial coordinates: the plane 8 (or 7) 100 cm long radially is close to the calorimeter with a 1 cm radial resolution. This suppresses the 3.9 false hit per good event by a factor of 100. For each hit in plane 8 only a band 8 cm wide in radius in plane 6 can contain the matching hit, due to the target size. This leaves about 10% of the track candidates, namely 0.1·11=1.1 false track per event. Then, the matching to plane 5 can be done in a road better than 3 mm wide, which leaves about 0.06 of false tracks per event. The matching in φ as well as the energy matching with the calorimeter should further reduce this contamination. A 4-th plane, at the location close to the plane 5, would reduce the false tracks by a factor of 0.06. An additional reduction of the false space hits in one plane can be potentially achieved by using signals from the last GEM, properly segmented[1].

Location	Z cm	Sector						Total	
		#	$\Delta\varphi$	R_{min} cm	R_{max} cm	pitch mm	# chan	surface m^2	# chan
5	155	30	10°	55	115	0.4	1000	2.7	30 k
6	185	30	10°	65	140	0.4	1220	4.0	36 k
7	295	30	10°	105	200	0.6	1160	7.6	35 k
8	310	30	10°	115	215	0.6	1250	8.6	38 k
total								23.0	140 k

Table B.2: The sizes and the number of readout channels in the GEM coordinate detectors.

Let us assume all the detectors are built using the GEM technology, similar to [53,54], but with a smaller angle of ∼ 10° between the readout projections. The readout pitch was 0.4 mm and a resolution of 71 μm was achieved. Although a resolution of 200 μm is sufficient for us, increasing the pitch increases the rate per stripe, therefore we consider the same 0.4 mm pitch for the planes 5 and 6 and a wider pitch of 0.6 mm for the planes 7 and 8. The detector sizes and the numbers of channels are given in Table B.2.

Several potential issues with the GEM detectors may occur and need to be considered at the stage of further optimization. The largest working chambers so far have a size of

[1] This technique is being developed for the Super Big Bite project at JLab

30×30 cm^2. Recently CERN succeeded in manufacturing of larger triple-GEM packages of 40×100 cm^2, which is about the size of one sector we need. However, one also needs to manufacture larger readout boards. We are considering ∼1 m long readout stripes, which will have a large capacitance. The impact of this on the resolution and the noise has to be studied. The problem can me mitigated by increasing the number of channels.

The GEM detectors give systematic spacial shifts for non-perpendicular trajectories. There are also possible effects of the non-uniform magnetic field at the exit of the solenoid. These effects may reduce the spacial resolution.

B.3 Electromagnetic Calorimeter

The hit patterns in the calorimeter plane and a possible detector arrangement are shown in Fig. B.3.

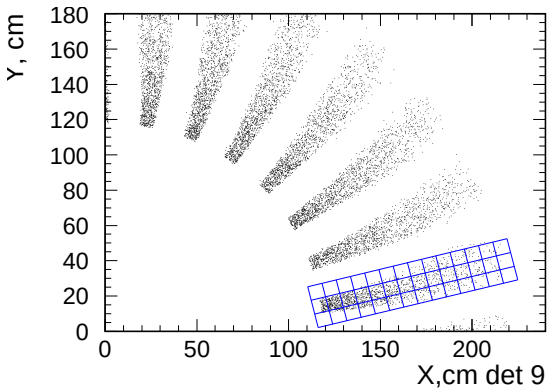

Figure B.3: The electron hit pattern in the calorimeter plane. A possible detector arrangement for one sector, with modules of 8 × 8 cm^2 is shown.

The low energy energy flux at the calorimeter face is about $2 \cdot 10^3$ GeV $\cdot$ cm$^{-2} \cdot$ s^{-1} (see Fig. 3.9). Assuming that all this energy is uniformly absorbed in a 5 cm depth of the calorimeter with an average density of 5 g/cm^3, the dose absorbed in a month of running is ∼30 Gy or 3 krad. Another considerable contribution comes from the pion flux (see Table 3.3). With the average energy deposit of 0.3 GeV per pion, and the average absorption depth of 10 cm, the dose per month is ∼ 2 krad. The experiment is supposed to run for at least a year, and a dose of ∼60 krad is too high for lead glass calorimeters.

Another limitation comes from the magnetic field of 0.01 T in the calorimeter area. The photomultiplier tubes, if used, would require a strong magnetic shielding.

A possible solution is a "shashlyk"-type calorimeter, which has been recently perfected [70, 71] to an energy resolution of $\sigma E/E \approx 2\% \oplus 3\%/\sqrt{E}$ by a thorough optimization of the geometry and the materials used. The calorimeter consists of a lead - plastic scintillator sandwich with several holes punched through its length. The light is collected by a set of wavelength-shifting (WLS) fibers inserted in the holes. The time

resolution of this calorimeter is about 100 ps. For the photodetectors, avalanche photodiodes (APD) are used, which are not affected by magnetic fields. A potential weak point is the radiation hardness of the plastic scintillator used, which might not exceed 100 krad. Other implementations of the "shashlyk" technique provided a resolution of about $\sigma E/E \approx 1\% \oplus 10\%/\sqrt{E}$ [72, 73, 74]. These detectors were built for a radiation environment of 0.5-5 Mrad/year.

In order to provide a good pion suppression the detector must contain a preshower (about 3-6 R.L. thick) part, which can be done relatively easily with the shashlyk geometry. For these studies, we assumed that the preshower was 6 R.L. thick, while the shower was 17 R.L. thick. The simulated signals amplitudes are shown in Fig. B.4. With the splitting used, the preshower/shower ratio allows to suppress the pions by an additional factor of ∼3. The further optimization will depend on the the details of the calorimeter implementation.

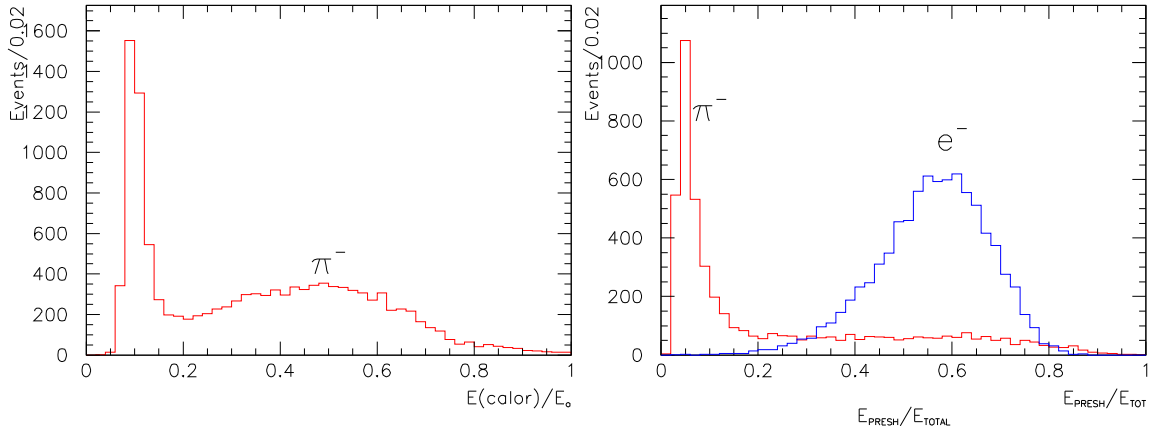

Figure B.4: Simulated calorimeter responses for pions and electrons. Left: the full pion signal, normalized to the pion momentum. Right - the ratio of the preshower and the total signals for electrons and pions.

B.4 Cherenkov Detector

A gas Cherenkov threshold detector is an essential part of the experiment and should provide at least a factor of 10 suppression of the pion background, independently of the calorimeter signals. There are several features to be taken into account:

- The radiator length is limited to about 80 cm. In order to have a large enough signal, we have to use a heavy gas.
- There is a high background of low energy photons. It is preferable to move the photodetector outside of the main flux, to larger radii and a shielded area. It is particularly important for detectors containing solid transparent windows as the photomultiplier tubes.

- The magnetic field in a particular place at large radii depends on the yoke design. With the present design it is about 0.01 T in the area convenient for positioning the photodetectors (Fig. 3.3).

The field of 0.01 T can be shielded enough for the regular PMTs used for Cherenkov detectors. Therefore, we consider the traditional design of gas Cherenkov threshold detectors. The volume is split azimuthally into 15 sectors. Each sector contains an elliptical mirror, a flat mirror and a photodetector. The optical configuration was optimized using GEANT3. The radiator gas C_4F_{10} (the pion threshold is 2.7 GeV/c) would provide at least 20 photoelectrons in a quartz-window PMT. The sight spot diameter is about 18 cm, which will require an optical cone to use a regular, 110 mm photocathode diameter PMT. A lighter gas CF_4 would provide about 9 photoelectrons with a pion threshold of 4.2 GeV/c. The light spot will be smaller.

One can also consider photodetectors immune to the magnetic field. A promising photodetector design, based on the GEM technology [75, 76, 77], uses CsI photocathodes deposited either on the chamber window, or on the GEM surface itself. Depending on the gas used, it can provide a collection efficiency for electrons of 60% or more.

This approach has been used to build a "hadron-blind" detector at PHENIX [75]. It is a windowless, proximity-focus Cherenkov detector with a 50-cm long CF_4 radiator. A triple-GEM detector is located in the same gas volume, the photocathode is deposited on the 1-st GEM. A mesh in front of the photocathode provides a cleaning electrical field preventing the electrons produced by ionizing particles to reach the 1-st GEM. The absence of windows or mirrors, along with a very good transparency of the gas to the UV light provides a high photoelectron yield of about 36. The readout pads have a size comparable with the spot size of the Cherenkov light of 2 cm^2. This detector allows to suppress pions by a factor of 50 at a 90% efficiency for electrons. This design might be applicable for the experiment proposed, however we need a 6.5 m^2 photodetector - 3-times larger than the PHENIX detector. A potential problem is a high rate of soft photons. On the other hand, the 1000 times finer segmentation than in the standard PMT-based detector, may compensate for the higher background.

Another approach would be a replacement of the PMTs by GEM-based photodetectors with quartz windows, 20×20 cm^2 each.

B.5 Trigger

The trigger logic (see Section 3.2.6) is based on the calorimeter signals. Each of 30 sectors will provide a separate trigger. The implementation depends on the electronics of the calorimeter. The pipeline electronics using Flash ADCs allows to organize the trigger within the FADC boards, eliminating the need for separate discriminators. This approach is being developed at JLab for the Hall D experiments.

B.6 Data Acquisition

The DAQ design will be driven by the detector needs, the rates, and the event topology. The events are single-particle events and are about 1 kbyte in size. The maximum trigger rate for the full detector is 500 kHz. With segmentation of the detector into 30 segments, the rates will be ∼16 kHz in each segment, which should be manageable using the pipelining approach that is being developed for the 12 GeV era upgrade of CODA. Using 10 Gigabit networks and fast event-building PCs, as well as large disk buffers and fast tape silos, the event-building and writing to tape might be able to take the full data rate; however, it may be necessary to perform some online data reduction as further explained below.

The DAQ will use the standard JLab CODA (CEBAF Online Data Acquisition) package and will capitalize on the new pipelining frontend architecture being developed for the 12 GeV upgrade which will achieve high rates, up to 200 kHz with virtually zero deadtime. The higher frontend rate capability is achieved essentially by having very large buffers at each stage of the pipeline. Given a trigger, one reads out only the segment of the pipeline corresponding to that trigger time. The JLab-designed VME-based F1-TDCs and Flash ADCs will be available and will support pipelining. In addition, competitive commercial TDC and FADC units are expected to come on the market. The JLab-FADC, for example, will be a 250 MHz 12 bit unit. With the development of a programmable interface to the FPGA firmware on these FADCs, the possibility of a fast and user-programmable trigger is foreseen, which could make the trigger more flexible and cheaper. Note, this FPGA-based trigger may allow a significant data reduction online, for example throwing out spurious hits in the tracking chambers.

We may need to build customized electronics on the frontend for the GEM detectors. For example, the readout developed at CERN [54] also used a pipeline approach which is compatible with the future JLab DAQ design philosophy. An analog application-specific integrated circuit (ASIC) called the APV25 was used for the CERN GEM detector. The chip consists of a preamplifier and shaper stage for each of the input channels, which was continuously sampled at 40 MHz and written into memory cells. Upon receiving a trigger, the corresponding memory locations were transferred to a FIFO with a maximum trigger latency of 4μsec before being multiplexed and read by an ADC. We might copy this design for the GEM detectors, with possible modifications to be compatible with the trigger supervisor. (The trigger supervisor is a custom-made device built by the JLab DAQ group which is an integral part of CODA.)

To take full advantage of faster frond-end readout, the 12 GeV upgrade of CODA plans to use VME64X crates, 10 Gigabit ethernet, and the new Trigger Supervisor that is being designed by the DAQ group that will support pipelining. The frontend VME cpus will be fast, multicore, and have Gigabit ethernet, and will have the option of using embedded Linux.

Some online data reduction may be necessary to reduce the data rate from 500 Mbyte/sec to perhaps less than 50 Mbyte/sec. Some reduction of noise and background may be possible online using the aforementioned FPGA programming in the FADCs. In

addition, the trigger supervisor supports second-level triggers; the first-level trigger is a fast decision and a second-level trigger is a slower, more complex decision, e.g. a decision that the event is a pion. The trigger supervisor then flags the data in the pipeline to not be read out. Further online reduction is possible in either the VME cpus or in the event-builder workstations where even more complex decisions can be made based on analysis of the data. Our preliminary plan is to analyze all the events on-line and write out the raw data only for about 10% of events, for calibration and monitoring purposes.

Appendix C

Polarimetry

C.1 Compton Polarimetry

Compton polarimetery is a very promising technique for high precision polarimetry at beam energies above a few GeV. Beam interactions with a photon target are non-disruptive, so Compton polarimetry can be employed at high currents as a continuous polarization monitor. The photon target polarization can be measured and monitored with a very high precision, and the scattering between a real photon and free electron has no theoretical uncertainty, such as the atomic or nuclear effects which can complicate other measurements. Radiative corrections to the scattering process are at the level of 0.1% and are very precisely known. The SLD result of 0.5% polarimetry demonstrates the feasibility of very high accuracy Compton polarimetry.

C.1.1 The Hall A Compton Polarimeter

As pictured in Fig. C.1, the Hall A Compton polarimeter is located in a chicane, about 15 meters long, just below the beamline. After modification to accommodate 11 GeV running, the electron-photon interaction point will be 21 cm below the primary (straight-through) beamline. After the interaction point, the electron beam is bent about 2 degrees by the third chicane magnet and then restored to the main beamline. The scattered electrons are separated from the primary beam and detected using silicon microstrips, just before the fourth chicane magnet. Scattered photons pass through the third chicane magnet to be detected in a calorimeter.

The photon target will be a 0.85 cm long Fabry-Perot cavity containing up to 2 kW of green (532 nm) light. The laser light is polarized using a quarter-wave plate, and can be toggled between opposite polarizations of highly circularly polarized light. The polarization of the transmitted light from the cavity is continuously monitored, and related to the laser polarization at the interaction point through a precisely measured transfer function. The feedback loop which locks the laser to the cavity resonance can be disabled to enable background measurements.

When well-tuned, the background rates in the photon and electron detectors are

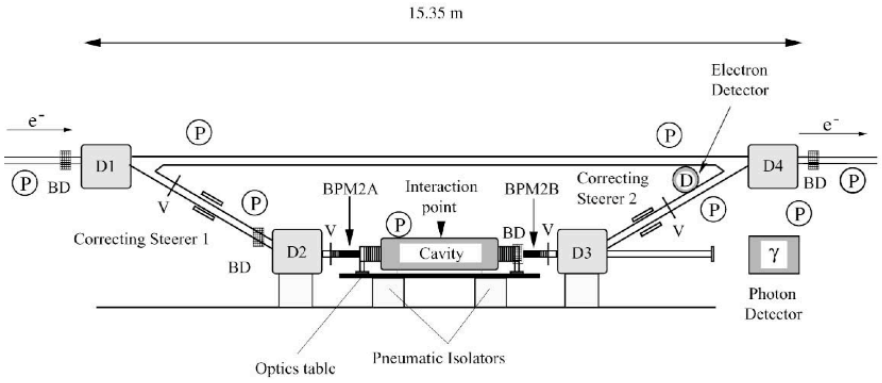

Figure C.1: Schematic of the Hall A Compton polarimeter. Figure from [78].

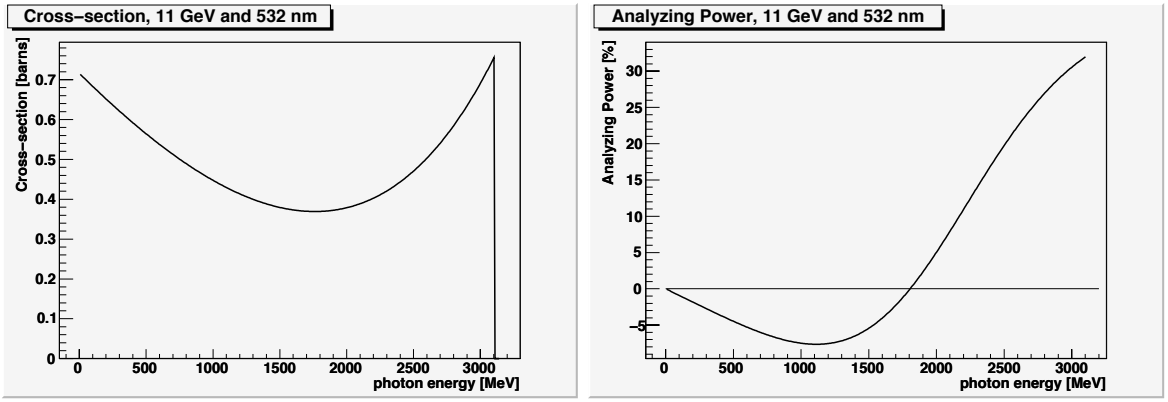

Figure C.2: The cross-section and asymmetry plotted versus Compton scattered photon energy for the Hall A polarimeter at 11 GeV.

similar, and have been held to < 100 Hz/μA in recent use. The dominant source of background is from beam halo or tails intercepting material in the chicane, although Bremsstrahlung from interaction with residual gas also contributes. At 11 GeV, the Compton-scattered rates will be in the range of 1 kHz/μA and the asymmetry will range from 32% to -7%; at 6.6 GeV, the rates will be comparable but the asymmetries about 2/3 as large. While the details depend on the specific detection and analysis approach is employed, statistical precision of 0.4% can be had in less than 5 minutes for most schemes at either energy.

The scattered electrons are detected in 4 planes of silicon microstrips, with 192 strips per plane and a strip pitch of 240 μm, located just upstream of the fourth chicane dipole. The asymmetry is measured as a function of position in the silicon microstrip detector. Although the analyzing power as a function of energy of the Compton scattering process is well-known, an energy calibration is required to convert position in the detector to energy of the electron.

The calorimeter for detecting scattered photons lies about 7 meters downstream of the interaction point. The strong forward boost of scattered photons leads to a tightly collimated photon beam (< 1 mrad), so the calorimeter size relates only to energy resolution through shower loss. The detector response function is calibrated using the electron detector to tag the photon energy. This response function is convoluted with the expected asymmetry distribution to estimate the analyzing power.

The specific calorimeter to be employed is not yet determined. Hall A has used a lead tungstate array at higher (> 3 GeV) energies. Althought the light yield is low, this is not an issue for higher photon energies of the measurements planned here, and the high speed of this material reduces pile-up issues. At lower energies, Hall A will use a GSO crystal with much higher light yield. This crystal might also be suitable, but it is somewhat slower than the lead tungstate. Designs for multi-layer sampling calorimeters, using either scintillation or Cerenkov light, will also be considered.

C.1.2 Systematic Uncertainties

Although the electron and photon detectors measure the same scattering events, many of the potential systematic errors arise in detector calibration and are entirely decorrelated between the analyses. Other sources of error, especially those that are related to the scattering process such as photon polarization or the total luminosity, are fully correlated between the two systems. Each of these separate catagories of potential systematic uncertainty: correlated, electron-only, and photon-only, will be discussed in the following sections.

Sources of Correlated Error

Any error associated with the Compton scattering process will be a common source of systematic error between the electron- and photon-detector analyses. One example lies in the energy normalization of the scattering process. The analyzing power is a function of both electron energy and photon energy, so these must be precisely determined. The photon wavelength will be determined to better than 0.1 nm and the electron energy to 5×10^{-4}, which leads to an uncertainty at the level of 0.03%.

A more significant source of error comes from the uncertainty in the photon polarization. The laser polarization at the interaction point is measured directly by opening the vacuum chamber and inserting optical diagnostics. The cavity mirrors must be removed for this measurement, as they do not transmit sufficient light for measurement when the cavity is not resonant. The effect of the mirrors is deduced from the change in the transfer function through the cavity, after the mirrors are replaced and the cavity locked. This effect is small, typically less than 0.1%. The polariation of the transmitted beam is monitored during production running. In the present Hall A polarimeter, the uncertainty in beam polarization is estimated at 0.35%. Although this number seems quite small, it should be kept in mind that it combines two relatively less challenging measurements: a measure of the depolarization and the linear polarization of the laser light at the level of 8%.

This result can be improved. More frequent measurement of the polarization and monitoring will be required, and a more sophisticated monitoring scheme will be implemented. The effect of vacuum windows will be studied, and if determined to be significant, the strain of the window under vacuum will be included in the transfer function measurement. The circular polarization is near maximum, so the sensitivity to additional birefringence is low. With the necessary effort, the circular polarization of the laser will be known with a precision of not less than 0.2%, which represents an error in the combined linear polarization and depolarization of not worse than 4.5%.

Helicity-correlated changes in luminosity of the laser/electron interaction point can introduce a false asymmetry. Various causes of luminosity variation must be considered, such as electron beam intensity, beam motion or spot-size variation. The control of helicity-correlated beam asymmetries is now a standard technology at Jefferson Lab, and typically achievable results (few part per million intensity, 10's of nanometers beam motion, $< 10^{-3}$ spot size changes) will suitably constrain the electron-photon crossing luminosity variations. Another possible source of false asymmetry would be electronics pickup of the helicity signal, which could potentially impact an integrating photon analysis. However, the demands of the primary experiment for isolation of the helicity signal exceed those for polarimetry by several orders of magnitude. In addition, the laser polarization reversal provides an additional cancellation for asymmetries correlated to the electron beam helicity. Potential effects must be carefully considered, but with due effort, false asymmetries will be a negligible source of uncertainty in this measurement.

Backgrounds are a common, though not fully correlated, problem for the two detector systems. The Hall A polarimeter commonly runs with a signal to background ratio of around 10:1. All known backgrounds are related only to the electron beam, and are not correlated to the presence of the laser light. Frequent, precise background measurements can be easily made by turning off the laser power. As a matter of routine, between 30-60% of data taking is done without the laser, for the purpose of background subtraction. Direct effects of background asymmetries and dilutions are presently estimated to be less than 0.04% in the Hall A system.

Systematic Errors for the Electron Detector

There are two primary sources of potential uncertainty for the electron detector. The first of these is a scale error in the measurement of asymmetries due to an imperfect deadtime correction. The second broadly concerns detector response, spectrometer uniformity and calibration and the impact on the estimated analyzing power.

With data rates potentially up to 100 kHz, DAQ deadtime corrections will be potentially significant, and a dedicated effort to control the related uncertainty will be necessary. The fast-counting DAQ can take very high rates with low deadtimes, and deterministic deadtime intervals are enforced in readout and acquisition electronics stages. The high statistical power of the measurement is of significant use here; the laser power can be varied and the effects mapped to a very high degree of statistical precision. The potential systematic error from deadtime correction arises from asymmetry deadtime as-

sociated with the total counting asymmetry. Although the peak asymmetry is high, the total integrated asymmetry is considerably reduced by the accepted range of negative asymmetry. With care, the total asymmetric deadtime correction will introduce no more than 0.2% uncertainty in the determination of polarization.

The analyzing power for the measured electron distribution can be very accurately determined. The calibration is assisted by the accessibility of two easily identified points of well-defined kinematics: the Compton edge and the asymmetry zero-crossing (0-Xing). Both points are fully determined by the beam and photon energies, and provide a precise method for energy calibration of the electron spectrum. The asymmetry spectrum for 11 GeV is plotted in Figure C.2. At 11 GeV, the Compton edge is 3.1 GeV below the beam momentum, with a peak asymmetry of $\sim 32\%$, and 0-Xing is 1.8 GeV below beam momentum. At the detector, these are located about 4.7 and 2.7 cm from the primary beam, respectively. At 6.6 GeV, the 1.26 GeV Compton edge is 3.2 cm from the primary beam with an asymmetry of $\sim 20.8\%$, while the zero-crossing at 700 MeV below beam energy is 1.8 cm from the beam.

The dominant uncertainties in this method involve the location of these points in the detector and the knowledge of the detector response between the end points. Depending on the analysis method, one can be variously sensitive or insensitive to these uncertainties. Here, we consider three separate methods for analyzing the electron detector data.

- *Integration* The polarization can be determined as a counting asymmetry for the sum of all strips from the Compton edge to the zero crossing.

  Since there is no Compton-scatter rate above the Compton edge, there is no systematic uncertainty in the analyzing power related to the estimated location of this point. The high momentum side of the integration cutoff will not occur precisely at the 0-Xing, but rather at an electron energy corresponding to as much as ± 0.5 of the pitch of the silicon detector strips. Since the asymmetry near the 0-Xing is nearly zero, the error in the 0-Xing location reduces the estimated analyzing power proportionally to the associated fractional change in expected rate; this is effectively an error in background dilution.

  The location of the 0-Xing will be fit using the nearly linear shape of the nearby asymmetry distribution. This procedure will introduce an additional source of statistical noise in the determination of the electron polarization. Small variations in the beam deflection by the third dipole and in the location of the electron detector will reduce systematic bias from the discretization of the data into the silicon strips, or from local differences in efficiency. It should be possible to avoid a systematic bias to a level better than 5% of the width of a strip, which would correspond to a 0.06% effect at 11 GeV and an 0.1% effect at 6 GeV.

  An error in the 0-Xing location could also arise from an experimental false asymmetry. The slope near the 0-Xing is such that a 0.1% false asymmetry would result in reduction of 0.25% the estimated analyzing power (and so a +0.25% in the measured electron polarization). The false asymmetry would directly represent an error in the electron polarization of about 0.51%, so this effect increases the sensitivity

to false asymmetry by factor of about 1.5. Even with this enhancement, the false asymmetry contribution to the polarization will still be negligible.

Probably the most significant uncertainty in the analyzing power will arise from efficiency variations among the silicon strips. Strip-by-strip efficiencies can be calculated by comparing track-hit efficiency between the 4 planes of the silicon detector. Inefficiency is expected to be low (less than 1%) and well measured, which will help minimize this effect. Comparison of results from the 4 detector planes will provide a cross-check on this effect, since local variations in asymmetries should be independent between the planes. Significant variations in the location of the detector relative to the primary beam, which would also help control this effect, should be possible, depending on the observed beam halo.

- *Asymmetry Fit* The polarization can also be found from the shape of the asymmetry over all strips between the Compton edge and the zero crossing. This technique would share the small uncertainties on determination of the 0-Xing with the integration technique. However, it would not be sensitive to strip-to-strip variations in efficiency, which is the dominant senstivity for the integration technique.

  This fit would be senstive to knowledge of the magnetic field uniformity. Deviations from the expected shape would introduce systematic uncertainty. Such an an effect may be evident in fit χ^2, could be cross-checked against the rate distribution, and could also be studied in high-statistics electron asymmetry distribution averaged over many runs.

- *Single Strip* The statistical power of the last, single silicon strip at the Compton edge will be significant, capable of 0.5% measurements on time-scales of around 15 minutes at 11 GeV or 20 minutes at 6.6 GeV. The rate of change of the asymmetry in this region is only 0.9% / mm. Locating this strip, relative to Compton edge, to a little better than half its own width should provide a robust 0.1% accuracy on the analyzing power. This technique would have a greatly reduced sensitivity to the 0-Xing location, dispersion variations or strip efficiency.

For each of these techniques the analyzing power should be estimated with an accuracy of around 0.2% or better. The cross-checks between techniques, each of which have very different sensitivities to possible sources of error, will provide convincing evidence that the system is well understood. Given these considerations, it seems likely that the electron detector analyzing power will not be the dominant source of systematic uncertainty for the polarimetry analysis.

Systematic Errors for the Photon Detector

The determination of the analyzing power is more difficult for the photon calorimeter than for the electron detector due to the width, and shape, of the detector response function. The photon detector analyzing power calculation must convolute this response function with the theoretical analyzing power curve. The response function shape and

energy calibration can be studied using the photon tagging through coincidence triggers with the electron detector.

In general, determining the effect of a low-energy threshold on the analyzing power depends sensitively on the shape of the response function; at low energies this is a major source of uncertainty. At high energies, the improved resolution and consistency of the response function shape over the range of interest will significantly reduce this problem. The electron-tagged photon spectrum, which can be calibrated to the zero-crossing and compton edge of the electron spectrum, is crucial to the energy calibration of the photon detector. The optimum location for the low-energy threshold is likely the asymmetry minimum, where uncertainty in the threshold will have minimal effect. Verifing that the electron polariazation result remains constant over variations in the applied lower threshold of the asymmetry analysis provides a useful cross-check of the technique.

Uncertainties related to the threshold, response function shape, and absolute energy calibration can also be eliminated by integrating all signal, without threshold. These previous problems are then replaced with a requirement on the uniformity of the average response over photon energy. At high energies, one expects very uniform behavior, although detector linearity will be crucial. Because the analyzing power integral is energy-weighted, the statistical figure-of-merit is not badly degraded by the negative asymmetry region.

The PREX experiment, with a beam energy of 1.2 GeV, will be unable to detect the asymmetry zero-crossing in the electron detector and so will be relying on the integrating photon method for polarimetry at the level of 1% precision. Complications in the response function for few to 10 MeV photons, and the inability to detect the electrons to tag electrons of such low energy, make that low energy experiment very challenging. Such low energy photons will be only a small correction to the result at 6.6 or 11 GeV. With the ability to study response function with the tagged photon beam over most of the energy range, the photon detector analyzing power normalization in the range of 0.3-0.4% should be achievable.

The rate in the photon detector is similar to that in the electron detector, around 1 kHz/μA, and the deadtime correction represents a similar potential systematic uncertainty. Counting in the photon detector is also senstive to pile-up, which distorts the asymmetry distribution. Background and rate distributions will serve as inputs to simulation for corrections on the analyzing power determination. In the current Hall A analysis, pile-up effects are estimated at the level of 1%, and the effect can be controled at a level better than 10% of itself. An integrating photon analysis requires no deadtime correction and has a greatly reduced sensitivity to pile-up, which is a significant advantage for high precision.

C.1.3 Summary of Compton Polarimetry Uncertainties

The prospects for 0.4% Compton polarimetry are excellent. However, an extremely aggressive and dedicated effort to reducing systematic uncertainty will be required. Table C.1.3 summarizes the systematic uncertainty estimates discussed above.

Relative error (%)	electron	photon
E_{Beam}	0.03	0.03
Laser polarization	0.20	0.20
False asymetries	0.01	0.01
Background	0.05	0.05
Deadtime	0.2	0.0
Pileup	0.0	0.1
Analyzing power	0.2	0.40
Total:	0.35	0.46

Table C.1: Table of systematic uncertainties for the Hall A Compton polarimeter at 6.6 GeV and 11 GeV. Estimates are described in Sect. C.1.2.

These ambitious goals will require vigorous and dedicated efforts to reduce sources of systematic uncertainty. It is expected that some significant fraction of data production time will be used for studies of the Compton polarimeter system which are not disruptive to the experiment, for example, scans of detector positions, laser power and polarization, data acquisition parameters, etc. The scattering asymmetry with both the 6.6 and 11 GeV beams is relatively large, which allows precision at the level of $\sim$0.5% in less than 1 minute of data. Given this high statistical power, these studies will be an effective method for constraining many of the possible experimental systematic uncertainties.

The future use of the Hall A polarimeter at 6.6 and 11 GeV will be a very different situation from the recent operation. The dominant systematic error in recent operation lay in the determination of the analyzing power. Operating at lower energies, and with an infrared (1064 nm) laser, the asymmetries were significantly lower and therefore the statistical power was worse. In addition, the limits of systematic uncertainty had not been pushed by demands of the experiment precision.

In the case of previous analyses of the electron detector, the zero-crossing calibration had not been exploited. The 0-Xing "integration" analysis was attempted for the first time for the HAPPEX-II and HAPPEX-He measurements. The situation was complicated due to the low beam energy of around 3 GeV, which not only reduced the average asymmetry but also reduced the ratio of Compton-scattered photon energies and the electron energies. At 3 GeV, the zero-crossing was about 5 mm from the primary beam, which was as close as the electron detector could get to the beam. Geometric efficiency at the edge was a signficant complication in this approach. In addition, the microstrip detector was damaged and displayed low and uneven efficiency, which complicated the analysis. The estimated systematic errors for that analysis which were not associated with these efficiency issues are consistent with Table C.1.3.

For the photon detector, the integration readout method has not yet been used for a physics experiment, and the counting photon analysis was typically limited by uncertainties in the detector response at lower energies. And the rapid access to high

statistical power, which is so powerful for cross-checking potential sources of systematic uncertainty, has never before been available to the Hall A Compton.

High-precision Compton polarimetry has also been widely applied at storage rings and colliders. Uncertainties in analyzing power determination have typically limited the precision of high-energy collider Compton photo-detectors to typically $\sim 0.8\%$. These measurements typically use the integrating photon technique for production running, since the electron beam currents are so high. However, in these measurements, photon tagging through coincidence with an electron detector is typically not available for study of the detector response function. The ability of the Hall A Compton polarimeter to perform *in situ* tagged photon calibrations will be a significant advantage.

C.2 Møller Polarimetry

C.2.1 Møller Scattering

Møller polarimeters exploit the properties of the polarized Møller scattering $\vec{e^-} + \vec{e^-} \rightarrow e^- + e^-$. Its unpolarized cross section, first calculated by C. Møller [79], in the Born approximation and the ultrarelativistic limit depends on the scattering angle in c.m. $\Theta_{\rm cm}$ and the Mandelstam variable s as:

$$\frac{d\sigma_\circ}{d\Omega_{\rm cm}} = \frac{\alpha^2}{s} \cdot \frac{(4 - \sin^2\Theta_{\rm cm})^2}{\sin^4\Theta_{\rm cm}}, \tag{C.1}$$

where α is the electomagnetic coupling constant, also presentable as $\alpha = r_e \cdot m_e$, where $r_e = 2.817 \cdot 10^{-13}$ cm is the classical electron radius. In the lab frame of the fixed target experiments, the scattering cross section at $\Theta_{\rm cm} = 90^\circ$ does not depend on s:

$$\frac{d\sigma_\circ}{d\Omega}(\Theta_{\rm cm} = 90^\circ) \approx 178 \text{ mb/ster}. \tag{C.2}$$

The polarized cross section depends on the beam and target polarizations $\mathcal{P}_{beam}$ and $\mathcal{P}_{target}$ as:

$$\frac{d\sigma}{d\Omega_{\rm cm}} = \frac{d\sigma_\circ}{d\Omega_{\rm cm}} \cdot (1 + \sum_{i=X,Y,Z} (A^M_{ii} \cdot \mathcal{P}_{targ\ i} \cdot \mathcal{P}_{beam\ i})), \tag{C.3}$$

where $i = X, Y, Z$ defines the projections of the polarizations. The analyzing power A^M, calculated in the same limits as Eq. C.1 [80, 81], depends on the angle $\Theta_{\rm cm}$ and does not depend on s. Assuming that the beam direction is along the Z-axis and that the scattering happens in the ZX plane:

$$A^M_{ZZ} = -\frac{\sin^2\Theta_{\rm cm} \cdot (7 + \cos^2\Theta_{\rm cm})}{(3 + \cos^2\Theta_{\rm cm})^2}, A^M_{XX} = -\frac{\sin^4\Theta_{\rm cm}}{(3 + \cos^2\Theta_{\rm cm})^2}, A^M_{YY} = -A^M_{XX} \tag{C.4}$$

At $\Theta_{\rm cm} = 90^o$ the analyzing power has its maximum $A^M_{ZZ\ max} = 7/9$. A beam transverse polarization in the scattering plane also leads to an asymmetry, though the analyzing power is lower: $A^M_{XX\ max} = A^M_{ZZ}/7$. The main purpose of the polarimeter is to measure the longitudinal component of the beam polarization.

C.2.2 Ways to Higher Accuracy

The polarized Møller scattering (described in Section C.2.1) is a convenient process for measuring the beam polarization. Its counting rate does not depend on the energy, the analyzing power is high (about 80%) and neither depends on the energy, nor changes considerably in the range of the polarimeter acceptance, and two electrons with high energies in the final state make it easy to detect their coincidence and reduce the background to negligible values.

For the polarized electron target only ferromagnetic foils have been used so far [82, 83, 84, 85, 86, 87, 88]. In fully magnetized iron, for instance, about 2.1 electrons from

the *d*-shell are polarized and the average electron polarization is about 8%. This value can not be calculated from the first principles, but has to be derived from the measured magnetization. Most of the polarimeters used foils tilted at an angle of about 20° to the beam and magnetized by external fields of 10-30 mT directed along the beam. In these conditions the magnetization is not fully saturated and depends on many parameters including the foil annealing and history. It can be measured, typically with an accuracy of 2-3%. The polarimeter of Hall C at JLab [89,88] uses foils perpendicular to the beam, magnetized to full saturation in a strong longitudinal field of 3-4 T. In this case, the magnetization has not been measured, but taken from published data on the properties of bulk iron, which claims an accuracy of $\sim 0.1\%$. In both cases, the orbital contribution to the magnetization of about 5% can be evaluated and subtracted using the magneto-mechanical factor, measured by other dedicated experiments [90]. With strong external fields of 3-4 T several additional correction of about 0.5% have to be made to compensate for extra orbital momenta and other complex effects. This correction is temperature dependent.

The magnetization of ferromagnetics depends on the temperature. The beam heats up the foil and the temperature in the beam area is difficult to measure or calculate accurately. This limits the average beam current to 2-3 μA, much lower than the current of > 50 μA to be used in the experiment. Using different beam regimes for experiment and polarimetry may become a source of systematic errors, difficult to evaluate. A possible way to solve this problem is to use a fast "kicker" magnet to move the beam back and forth across the edge of a foil located at a distance of about 1 mm from the regular beam position [91].

Another source of errors is the heavy atom used for the target. Møller scattering off electrons from the internal atomic shells has a distorted energy-angle correlation of the secondary electrons, with respect to scattering off electrons from the external shells. A difference of the polarimeter acceptance to these two classes of events is the source of a systematic bias (so-called Levchuk effect [92]), typically of about 1-5%. This effect forbids using a strong optical collimation of the secondary particles, favorable otherwise for background suppression. In most cases, the background is dominated by electron-nucleus scattering and contains one electron in the final state. It can be efficiently suppressed by detecting both secondary Møller electrons in coincidence, however this background typically doubles the detectors' counting rate.

The counting rates depend on the target thickness and the apparatus acceptance. The acceptance should not be too small, because of the Levchuk effect. The associated dead time is typically not negligible and can be a source systematic errors.

The list of systematic errors for the JLab Møller polarimeters in Hall A and Hall C are presented in Table C.2.

Although it is possible to reduce considerably the systematic error of the foil polarization by using a very high magnetization field [88], it is difficult to reduce the other errors, in particular the one associated with the beam current limitations. Also, it is difficult to organize continuous measurements since even the thinnest foil used (~ 1 μm)

Variable	Hall C	Hall A		
		present	upgraded	proposed
Target polarization	0.25%	2.00%	0.50%	0.01%
Target angle	0.00%	0.50%	0.00%	0.00%
Analyzing power	0.24%	0.30%	0.30%	0.10%
Levchuk effect	0.30%	0.20%	0.20%	0.00%
Target temperature	0.05%	0.00%	0.02%	0.00%
Dead time	-	0.30%	0.30%	0.10%
Background	-	0.30%	0.30%	0.10%
Others	0.10%	0.30%	0.30%	0.30%
Total	0.47%	2.10%	0.80%	0.35%

Table C.2: A list of systematic errors quoted for the Møller polarimeters in Hall C [88] and in Hall A. The present Hall C configuration is assumed. For Hall A, the first column shows the present configuration, the second column shows the expectations for the high-field target, Hall C style upgrade, which is under way, while the last column shows the expectations for the polarimeter, equipped with an atomic hydrogen target. The regular, low beam current operation is assumed for all but the last column, which describes operations at high beam currents of < 100 μA.

strongly affects the electron beam.

There might be a way to avoid the shortcomings of the ferromagnetic targets. It has been proposed [93, 94, 95] to use polarized atomic hydrogen gas, stored in an ultra-cold magnetic trap, as the target. Such a target of practically 100% polarized electrons would remove the errors associated with the ferromagnetic targets, namely the polarization and the Levchuk effect. The other errors as the analyzing power uncertainty and the dead time can be strongly suppressed. Such a target is thin enough to be used continuously with the experiment. The expected systematic error (see Table C.2) is below 0.5%. A 1% statistical accuracy can be achieved in less than 30 min of running. We propose to develop the novel technique of atomic hydrogen targets for the Møller polarimetry. This will require a dedicated R&D project. Although the technique of hydrogen trapping is well established, there is presently no experience in passing a high intensity beam through such a trap. This project is described in Section C.2.3.

For the backup solution we consider the technique, being developed for Hall C [91], which involves a polarized foil and a "kicker" magnet used to move the beam. This option is described in Section C.2.4.

In both cases, the spectrometer for the Hall A Møller polarimeter (see Fig. C.3) does not need to be changed.

C.2.3 Atomic Hydrogen Target

A detailed description of the project can be found in [95]. Here, a summary is presented.

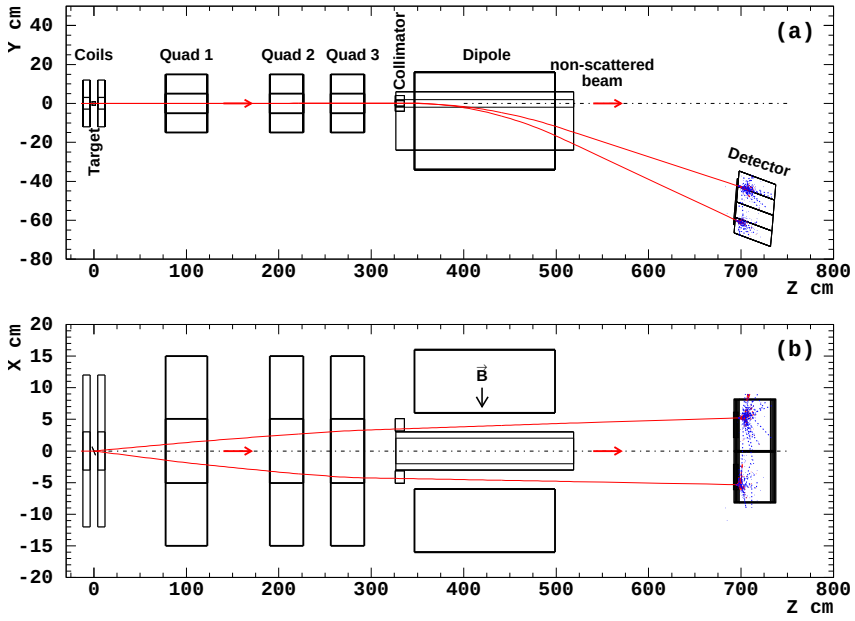

Figure C.3: The layout of the Hall A Møller polarimeter in it present configuration. The planned upgrade for 12 GeV includes lifting of the detector box to compensate for a smaller deflection in the dipole.

Hydrogen Atom in Magnetic Field

The magnetic field B_S and the hyperfine interaction split the ground state of hydrogen into four states with different energies. The low energy states are $|a\rangle = |\downarrow\uparrow\rangle \cdot \cos\theta - |\uparrow\downarrow\rangle \cdot \sin\theta$ and $|b\rangle = |\downarrow\downarrow\rangle$, where the first and second (crossed) arrows in the brackets indicate the electron and proton spin projections on the magnetic field direction. As far as the electron spin is concerned, state $|b\rangle$ is pure, while state $|a\rangle$ is a superposition. The mixing angle θ depends on the magnetic field B_S and temperature T: $tan\ 2\theta \approx 0.05\ \mathrm{T}/B_S$. At B_S =8 T and T = 0.3 K the mixing factor is small: $\sin\theta \approx 0.003$. State $|b\rangle$ is 100% polarized. State $|a\rangle$ is polarized in the same direction as $|b\rangle$ and its polarization differs from unity by $\sim 10^{-5}$.

Storage Cell

In a magnetic field gradient, a force $-\nabla(\vec{\mu_H}\vec{B})$, where μ_H is the atom's magnetic moment, separates the lower and the higher energy states. The lower energy states are pulled into the stronger field, while the higher energy states are repelled from the stronger field. The 0.3 K cylindrical storage cell, made usually of pure copper, is located in the bore of a superconducting ~8 T solenoid. The polarized hydrogen, consisting of the low energy states, is confined along the cell axis by the magnetic field gradient, and laterally by the wall of the cell (Fig C.4).

At the point of statistical equilibrium, the state population, p follows the Boltzmann

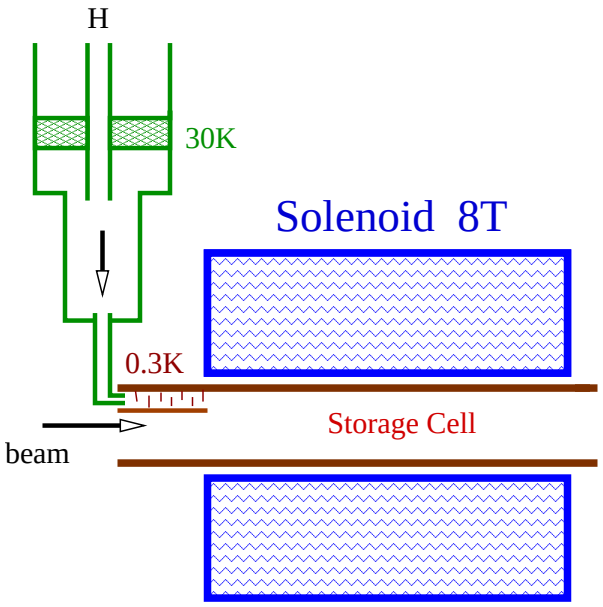

Figure C.4: A sketch of the storage cell

distribution:

$$p \propto \exp(\mu_e B/kT), \tag{C.5}$$

where μ_e is the electron's magnetic moment ($\mu_H \approx \mu_e$) and $k = k_B$ is the Boltzmann constant. The cell is mainly populated with states $|a\rangle$ and $|b\rangle$, with an admixture of states $|c\rangle$ and $|d\rangle$ of $\exp(-2\mu_e B/kT) \approx 3 \cdot 10^{-16}$. In the absence of other processes, states $|a\rangle$ and $|b\rangle$ are populated nearly equally. The gas is practically 100% polarized, a small ($\sim 10^{-5}$) oppositely polarized contribution comes from the $|\uparrow\downarrow\rangle$ component of state $|a\rangle$.

The atomic hydrogen density is limited mainly by the process of recombination into H_2 molecules (releasing ~4.5 eV). The recombination rate is higher at lower temperatures. In gas, recombination by collisions of two atoms is kinematically forbidden but it is allowed in collisions of three atoms. On the walls, which play the role of a third body, there is no kinematic limitation for two atom recombination. At moderate gas densities only the surface recombination matters. In case of polarized atoms, the cross section for recombination is strongly suppressed, because two hydrogen atoms in the triplet electron spin state have no bound states. This fact leads to the possibility of reaching relatively high gas densities for polarized atoms in the traps.

A way to reduce the surface recombination on the walls of the storage cell is coating them with a thin film (~50 nm) of superfluid ^{4}He. The helium film has a very small sticking coefficient[1] for hydrogen atoms. In contrast, hydrogen molecules in thermal equilibrium with the film are absorbed after a few collisions and are frozen in clusters on the metal surface of the trap [96].

[1] The sticking coefficient defines the atom's adsorption probability per collision with a surface.

The higher energy states are repelled from the storage cell by the magnetic field gradient and leave the cell. Outside of the helium-covered cell, the atoms promptly recombine on surfaces into hydrogen molecules which are either pumped away or are frozen on the walls. Some of the higher energy states recombine within the cell and the molecules eventually are either frozen on the helium-coated wall, or leave the cell by diffusion.

The cell is filled with atomic hydrogen from an RF dissociator. Hydrogen, at 80 K, passes through a Teflon[2] pipe to a nozzle, which is kept at ∼30 K. From the nozzle hydrogen enters into a system of helium-coated baffles, where it is cooled down to ∼0.3 K. At 30 K and above, the recombination is suppressed because of the high temperature, while at 0.3 K it is suppressed by helium coating. In the input flow, the atoms and molecules are mixed in comparable amounts, but most of the molecules are frozen out in the baffles and do not enter the cell.

The gas arrives at the region of a strong field gradient, which separates very efficiently the lower and higher atomic energy states, therefore a constant feeding of the cell does not affect the average electron polarization.

This technique was first successfully applied in 1980 [97], and later a density[3] as high as $3 \cdot 10^{17}$ atoms/cm^3 was achieved [98] in a small volume. So far, the storage cell itself has not been put in a high-intensity particle beam.

For the project being discussed a normal storage cell design can be used, with the beam passing along the solenoid axis (Fig. C.4). The double walls of the cylindrical copper cell form a dilution refrigerator mixing chamber. The cell is connected to the beam pipe with no separating windows. The tentative cell parameters are (similar to a working cell [99]): solenoid maximum field of $B_S = 8$ T , solenoid length of $L_S = 30$ cm, cell internal radius of $r_\circ = 2$ cm, cell length of $L_C = 35$ cm and temperature of $T = 0.3$ K. The effective length of such a target is about 20 cm.

For the guideline, we will consider a gas density of $3 \cdot 10^{15}$ cm^{-3}, obtained experimentally [100], for a similar design.

Gas Properties

Important parameters of the target gas are the diffusion speed. At 300 mK the RMS speed of the atoms is ∼80 m/s. For these studies we used a calculated value [101] of the hydrogen atoms cross section $\sigma = 42.3 \cdot 10^{-16}$ cm^2, ignoring the difference between the spin triplet and singlet cross sections. This provided the mean free path $\ell = 0.57$ mm at density of $3 \cdot 10^{15}$ cm^{-3}.

The average time, τ_d for a "low field seeking" atom to travel to the edge of the cell, assuming its starting point is distributed according to the gas density, is[4]: $\tau_d \approx 0.7$ s. This is the cleaning time for an atom with opposite electron spin, should it emerge in the

[2]Teflon has a relatively small sticking coefficient for hydrogen atoms.

[3]This parameter is called concentration, but we will use the word density in the text, since the mass of the gas is not important here.

[4]This time was estimated using simulation, taking into account the gas density distribution along z and the repelling force in the magnetic field gradient.

cell and if it does not recombine before. The escape time depends on the initial position of the atom, going from ~ 1 s at $z = 0$ to 0.1 s at $z = 8$ cm. The average wall collision time is about 0.5 ms.

Gas Lifetime in the Cell

For the moment we consider the gas behavior with no beam passing through it. Several processes lead to losses of hydrogen atoms from the cell: thermal escape through the magnetic field gradient, recombination in the volume of gas and recombination on the surface of the cell.

The volume recombination can be neglected up to densities of $\sim 10^{17}$ cm^{-3} [98].

The dominant process, limiting the gas density, is the surface recombination. In order to keep the gas density constant the losses have to be compensated by constantly feeding the cell with atomic hydrogen. Our calculations, based on the theory of such cells [98], show, that a very moderate feed rate of $\Phi \sim 1 \cdot 10^{15}$ atoms/s would provide a gas density of $7 \cdot 10^{15}$ cm^{-3}.

This can be compared with the measurement [100] of $3 \cdot 10^{15}$ cm^{-3}. The average lifetime of a "high field seeking" atom in the cell is $\sim$1 h.

Unpolarized Contamination

The most important sources of unpolarized contamination in the target gas in absence of beam have been identified:

1) hydrogen molecules: $\sim 10^{-5}$;

2) high energy atomic states $|c\rangle$ and $|d\rangle$: $\sim 10^{-5}$;

3) excited atomic states $< 10^{-10}$;

4) other gasses, like helium and the residual gas in the cell: $\sim 10^{-3}$

The contributions 1)-3) are present when the cell is filled with hydrogen. They are difficult to measure directly and we have to rely on calculations. Nevertheless, the behavior of such storage cells has been extensively studied and is well understood [98]. The general parameters, like the gas lifetime, or the gas density are predicted with an accuracy better than a factor of 3. The estimates 1)-3) are about 100 times below the level of contamination of about 0.1% which may become important for polarimetry. In contrast, the contribution 4) can be easily measured with beam by taking an empty target measurement. Atomic hydrogen can be completely removed from the cell by heating a small bolometer inside the cell, which would remove the helium coating on this element, and catalyze a fast recombination of hydrogen on its surface. However, it is important to keep this contamination below several percent in order to reduce the systematic error associated with the background subtraction.

Beam Impact on Storage Cell

We have considered various impacts the $\mathcal{I}_b = 100$ μA CEBAF beam can inflict on the storage cell. The beam consists of short bunches with $\tau = \sigma_T \approx 0.5$ ps at a $\mathcal{F} = 499$ MHz repetition rate. The beam spot has a size of about $\sigma_X \approx \sigma_Y \sim 0.1$ mm. The most important depolarization effects we found are:

A) gas depolarization by the RF electromagnetic radiation of the beam: $\sim 3 \cdot 10^{-5}$;

B) contamination from free electrons and ions: $\sim 10^{-5}$;

C) gas excitation and depolarization by the ionization losses: $\sim 10^{-5}$;

D) gas heating by ionization losses: $\sim 10^{-10}$ depolarization and a $\sim$30% density reduction.

The effects A) and B) are described below.

Beam RF Generated Depolarization

The electromagnetic field of the beam has a circular magnetic field component, which couples to the $|a\rangle \rightarrow |d\rangle$ and $|b\rangle \rightarrow |c\rangle$ transitions. The transition frequency depends on the value of the local magnetic field in the solenoid and for the bulk of the gas ranges from 215 to 225 GHz. The spectral density function of the magnetic field can be presented in the form of Fourier series with the characteristic frequency of $\omega_\circ = 2\pi\mathcal{F}$. The Fourier coefficients are basically the Fourier transforms of the magnetic field created by a single bunch. The bunch length is short in comparison with the typical transition frequency ($\omega_{trans}\tau \sim 0.1$). The resonance lines of the spectrum (a reflection of the 499 MHz repetition rate) populate densely the transition range (see Fig. C.5). The induced transition rate depends on the gas density at a given transition frequency. This rate was calculated taking into account the beam parameters and the field map of a realistic solenoid. Provided that the field of the solenoid is fine tuned to avoid the transition resonances for the bulk of the gas in the cell (see Fig. C.5), the depolarization described has the following features:

- the transition rate is proportional to $\mathcal{I}_b^2$;
- the average rate of each of the two transitions is about $0.5 \cdot 10^{-4}$ of the target density per second;
- at the center around the beam the full transition rate is about 6% of the density per second.

In order to estimate the average contamination we take into account that each resonance line presented in Fig. C.5 corresponds to a certain value of the solenoid field and, therefore, affects the gas at a certain z. Using a realistic field map of the solenoid we obtained that the average depolarization in the beam area will be reduced to about $\sim 0.3 \cdot 10^{-4}$ by the lateral gas diffusion and by the escape of the "low field seeking" atoms from the storage cell.

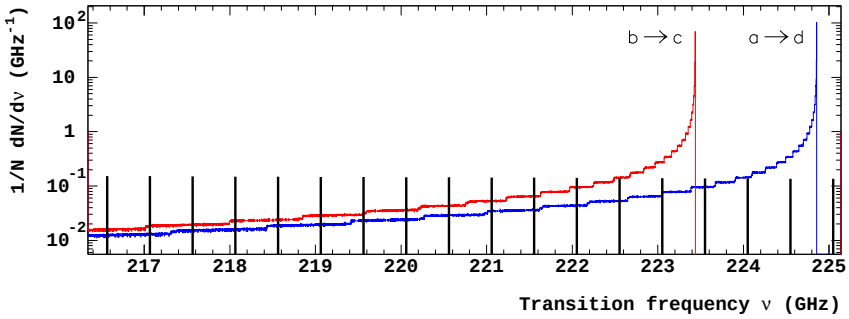

Figure C.5: Simulated spectra of the transitions on the axis of the hydrogen trap with the maximum field of 8.0 T. The density of atoms depends on the field as $exp(-\mu_e B/kT)$. The two curves show $\frac{1}{N}dN/d\nu_{ad}$ and $\frac{1}{N}dN/d\nu_{bc}$ - the relative number of atoms which can undergo $|a\rangle \rightarrow |d\rangle$ and $|b\rangle \rightarrow |c\rangle$ transitions at the given frequency, per one GHz. The resonant structure of the spectral function of the beam-induced electromagnetic field is shown as a set of vertical bars, 499 MHz apart.

In order to study experimentally the depolarization effect discussed, one can tune the solenoid magnetic field to overlap a resonance line with the transition frequency of the gas at the cell center. This would increase the transition rate by a factor of ∼70.

Contamination by Free Electrons and Ions

The beam would ionize per second about 20% of the atoms in the cylinder around the beam spot. The charged particles would not escape the beam area due to diffusion, as the neutral atoms would do, but will follow the magnetic field lines, parallel to the beam. An elegant way to remove them is to apply a relatively weak ∼1 V/cm electric field perpendicular to the beam. The charged particles will drift at a speed of $v = \vec{E} \times \vec{B}/B^2 \sim 12$ m/s perpendicular to the beam and leave the beam area in about 20 μs. This will reduce the average contamination to a 10^{-5} level.

Application of the Atomic Target to Møller Polarimetry

This feasibility study was done for the possible application of the target discussed to the existing Møller polarimeter in Hall A at JLab.

The beam polarization at JLab is normally about 80%, at beam currents below 100 μA. Scaling the results of the existing polarimeter to to the hydrogen target discussed we estimated that at 30 μA a 1% statistical accuracy will be achieved in about 30 min. This is an acceptable time, in particular if the measurements are done in parallel with the main experiment.

There is no obvious way to measure directly the polarization of the hydrogen atoms in the beam area. The contamination from the residual gas is measurable. The rest relies on calculations. All calculations show that the polarization is nearly 100%, with a possible contamination of <0.01%, coming from several contributions. The impact of

the most important of these contributions can be studied, at least their upper limits, by deliberately increasing the effect. For example, the beam RF induced transitions can be increased by a factor of ∼70, by fine tuning of the solenoid magnetic field. The contribution from the charged particles in the beam area can be varied by a factor up to $\sim 10^4$, by changing the cleaning electric field.

The systematic errors, associated with the present Hall A polarimeter, when added in quadrature give a total systematic error of about 3%. Scaling these errors to the design with the hydrogen target reduces the total error to about 0.3%. If we scale the accuracy of the Hall C polarimeter (see Table C.2), the projected total error would be better than 0.2%. There is no doubt that achieving such an accuracy is a major challenge and will require re-evaluation of the error budget for including smaller effects, so far neglected. However, the technique described has a potential to deliver an accuracy of 0.4% required for the experiment proposed.

C.2.4 Møller Polarimeter in Hall C

The Hall C Møller polarimeter was originally designed and constructed by the Basel Nuclear Physics group to overcome what has been to date, the most significant systematic uncertainty in the Møller polarimetry technique - namely the knowledge of the polarization of the "target" used in the measurement of the double–spin Møller scattering asymmetry.

As described in Sec. C.2, the Hall C Møller polarimeter makes use of a pure iron foil, typically 1 to 10 μm thick oriented perpendicular to the electron beam direction and brute–force polarized out of plane using a 3–4 T superconducting solenoid. In principle, such a target results in knowledge of the target polarization to better than 0.25% [102].

One drawback of this saturated foil target, however, is the need to avoid significant temperature changes due to beam heating. As seen in Fig. C.6, a temperature increase of 60–70 degrees C results in a reduction of the target polarization of $\approx$ 1%. The need to avoid such temperature changes typically limits the beam current used in Møller measurements to 1-2μA. Higher currents can and have been used in Hall C using a circular raster of ≈1 mm radius to limit beam heating. However, even with a large raster, practical beam currents are limited to 20 μA before beam heating becomes significant. This is still well away from the nominal current ($> 50\mu$A) to be used in this experiment. In principle, measurements using the Kerr effect may be used to monitor the relative target polarization, but this requires that the laser impinge on the iron foil at precisely the same point (and perhaps with the same shape) as the electron beam.

One can attempt to mitigate foil heating effects using a fast beam kicker system combined with a thin strip or wire target. In this system, the electron beam is kicked at some low duty cycle onto or across a pure iron target. The beam is only impinging on the target for timescales on the order of μs such that the target does not have much opportunity to heat up, while the relatively long time between kicks allows the target to cool.

A series of tests have been performed in Hall C with two prototype kicker magnets

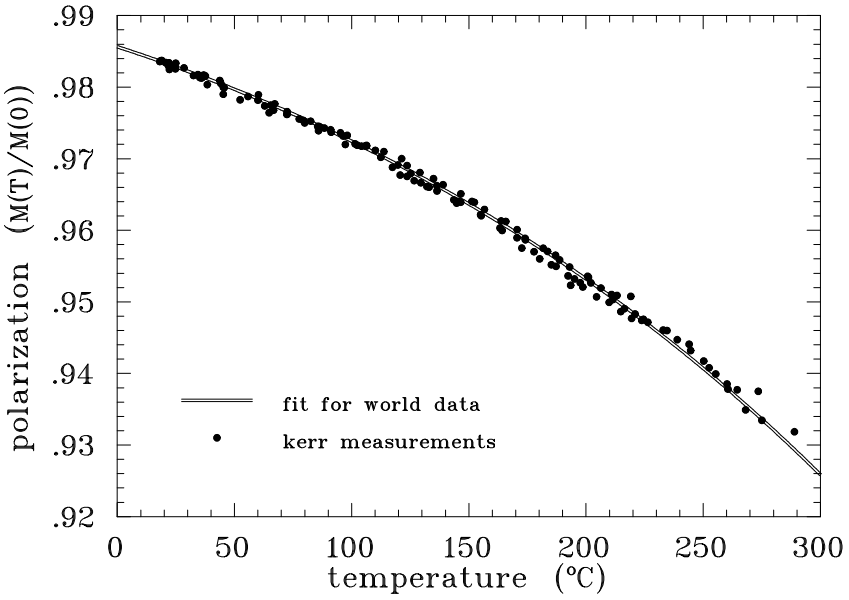

Figure C.6: Relative magnetization vs. temperature for a pure iron foil driven to magnetic saturation (from [102]). The iron foil used in the Hall C Møller polarimeter is normally at room temperature with no active cooling.

and two different target configurations [91]. Initial tests were performed with 25 μm diameter iron wires replacing the iron foil at the Møller target. While these tests were moderately successful, it was found that the high instantaneous current combined with the relatively thick profile of the target lead to a high rate of random coincidences. The second generation prototype target replaced the iron wires with a 1 μm strip target, reducing the instaneous rate.

Results from the second generation tests are shown in Fig. C.7. In this case, the duration of the beam "kick" was about 10 μs at a repetition rate between 5 and 10 kHz. Data were taken using the kicker and iron strip target up to 40 μA. In general, the results were consistent with there being no effect from target heating, albeit with relatively low precision. Problems with beam transport precluded the use of higher beam currents. Finally, it should be noted that apparent instabilities with either the source or Hall C Møller polarimeter itself (found by taking "calibration" data at 2 μA from a normal iron foil) made it difficult to conclude that target heating effects were completely avoided.

An improved kicker magnet capable of scanning the beam across an iron strip target in $\approx$ 1 μs has been constructed and will be installed for the Q_{Weak} experiment in Hall C. In addition to the improved kick speed, the new kicker will hold the electron beam at a nearly fixed position on the foil (see Fig. C.8) such that one can gate off the data–taking during periods in which the beam is "in transit." We estimate that allowing the beam to dwell on the iron strip target for periods of $\approx$1 μs with a frequnecy of 2.5 kHZ will keep target depolarization due to heating effects to the 1% level.

Application of a similar technique for this experiment requires consideration of sev-

eral issues. First, the fastest kicker magnet developed for Hall C will only operate up to a beam energy of ≈2 GeV. Given that the currents will likely be about a factor of three smaller, a slower kicker is likely acceptable. For example, a kick duration of 8 μs is sufficiently fast to keep target depolarization effects at the 1% level. Space in the beamline would need to be found, preferably far from the Møller target region to maximize deflection for a given $\int \vec{B} \cdot d\vec{l}$. Also, it should be noted that for the Hall C system, up to 1% effects are deemed acceptable, assuming that we can estimate the correction to the target polarization with a precision of something like 50% of the size of the effect. Since the goal here is 0.5% polarimetry, the allowed effects from target heating will need to be smaller. A kicker capable of kick durations of ≈4 μs yielding 1-2 mm deflection at the Møller target at 11 GeV would need to be designed and built.

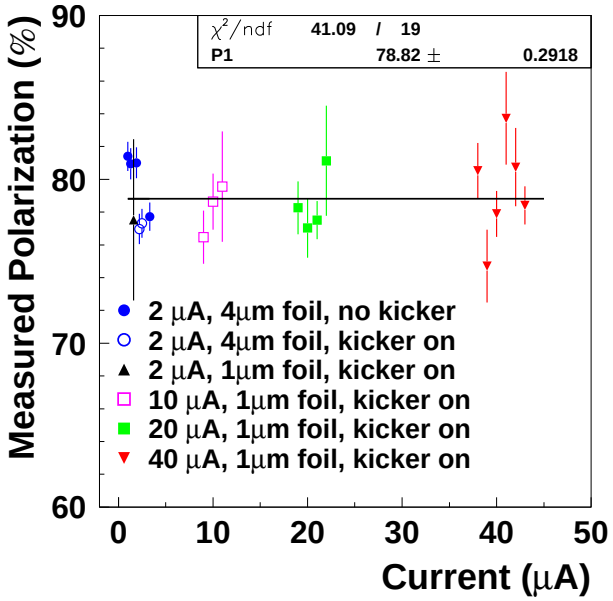

Figure C.7: Results of polarization measurements taken in Hall C using the second generation kicker magnet impinging on a 1 μm thick iron foil strip target. Measurements were made at beam currents up to 40 μA. Higher currents were not accessible to due to beam losses from the deflected electron beam. Control measurements at 2 μA were not stable, so these measurements cannot be used to prove 1% precision at high currents.

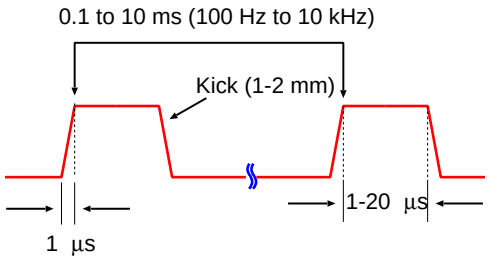

Figure C.8: Schematic of the operating mode of the new kicker magnet to be installed for Q_{Weak}. The beam is kicked 1-2 mm in about 1 μs and remains stationary on the Møller target for 1 to several μs.

Appendix D

Options for the Apparatus: Double Toroid Spectrometer (DTS)

The apparatus described in Sec. 3.2 represents what we feel is the best optimization of the spectrometer requirements and cost. An alternative spectrometer, based on two toroidal magnets has also been considered. The design and cost of a toroidal-based spectrometer are presented in this appendix.

D.1 Overview

With a single toroidal magnet, the tracking detectors can be positioned downstream of the magnet with the magnet shading the detectors from a direct view of the target. In this configuration, the momentum can be measured only if the target is very short. Therefore, we are considering two toroidal magnets, both focusing the electrons toward the beam:

- *TOR1:* a strong magnet focusing the DIS electrons in the given kinematic range nearly parallel to the beam;
- *TOR2:* a magnet of the same dimensions as TOR1, but weaker, providing the momentum measurement.

The first arm of detectors is located between *TOR1* and *TOR2*, the second arm is located downstream of *TOR2*.

A regular toroid with a field $B \propto 1/R$ is not ideally suited to focus the particles of interest. Instead, we are considering a toroid with a constant field, with the current, crossing a circle of radius R, being $I \propto R$. Its coils should be filled uniformly with the wire. An optimized optics using ideal toroids with constant fields is shown in Fig. D.1. The collimators at small angles shade the detectors from the target. *TOR1* should provide a field of ≈ 2.1 T, the field in *TOR2* can be 2-3 times smaller. This design leads to a very low level of background in the detectors, which are located in areas free of strong magnetic fields. It also allows for the use of conventional detector types, as drift chambers, photomultiplier tubes and lead-glass calorimeters.

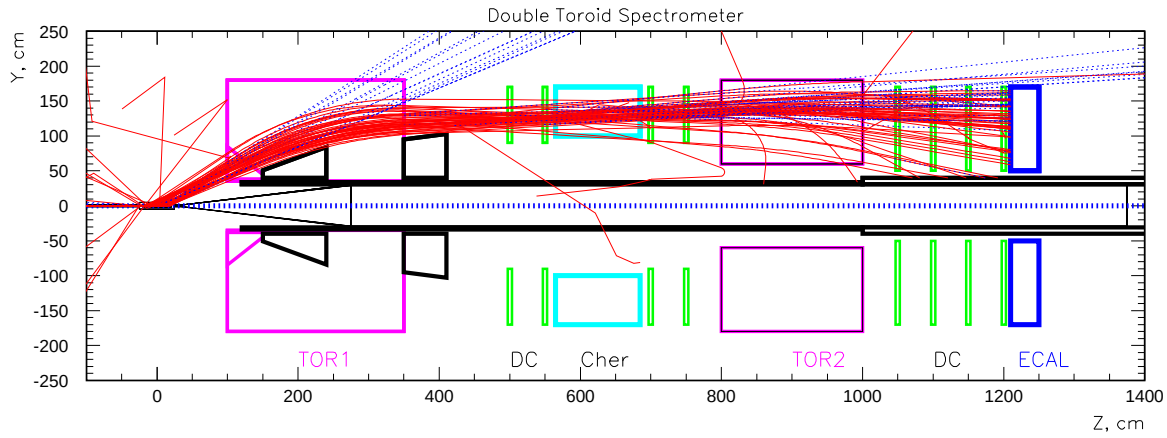

Figure D.1: The layout of the DTS design. The target is located 1 m upstream of the front of *TOR1*-magnet. Two conical collimators absorb the small angle and low momentum background. The 1^{st} detector arm (between the two magnets) is equipped with coordinate detectors and a gas Cherenkov detector. The second arm contains coordinate detectors and an electromagnetic calorimeter.

D.2 Toroidal Magnets

For *TOR2* we plan to use the existing magnet built for G0 experiment at JLab [103,104]. This superconducting toroidal magnet has 8 coils. Each coil contains 4 layers times 36 cable turns per layer and operates at 5 kA/cm^2. The coil thickness is 12 cm. The maximal field in the coil area is about 4 T, the full stored energy is 7.6 MJ. The calculated field in one sector is shown in Fig. D.2.

Designing the *TOR1*-magnet we take into account the limitation on the allowed field in the coil area, for the given current density, and the requirements of the optics. In order to match the geometry of *TOR2* we consider the *TOR1*-magnet containing 8 or 16 coils. The larger the number, the smaller is the acceptance, but also the lower is the field in the coil area. At the current level of optimization, we came to the coil geometry shown in Fig. D.3. We assume that the superconducting cable has a cross section of 5×20 mm^2.

The field maps are shown in Fig. D.4 for two options: 8 thick coils and 16 thinner coils. For the second option, current density and the maximum field in the coil area are smaller. The current was adjusted to provide the required optics. The results are summarized in Tab. D.1. The 8-coil option for *TOR1* provides a larger acceptance than the 16 coil option because it contains fewer cable layers in total but requires higher current and provides a higher field in the coil area. In the 16-coil option, these these two crucial parameters in the safe range.

The optics of DTS has a peculiar defocusing feature, which reduces the overall acceptance. The toroidal magnet has a radial field component close to the coil (see Figs. D.2, D.4) which pushes the particles toward the coil. The bend is enough to send these particles into the coil of the second toroid. The more coils the toroid has, the less

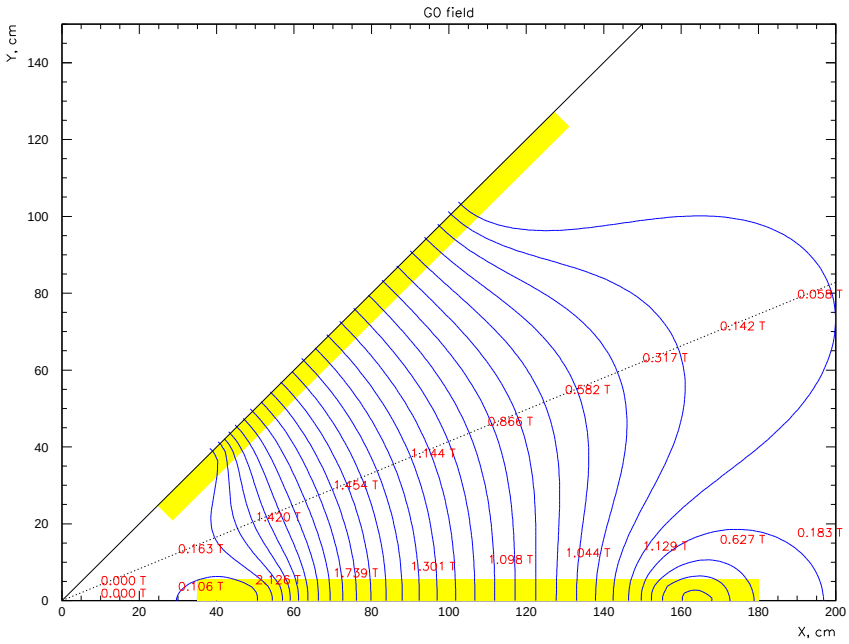

Figure D.2: The field map of the G0 toroidal magnet.

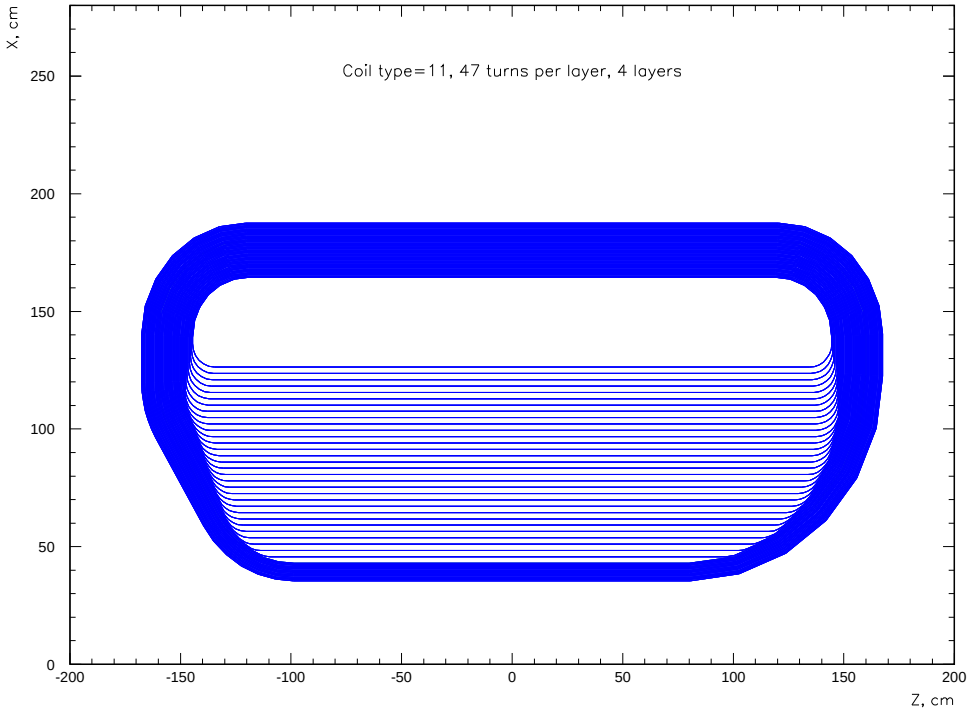

Figure D.3: The *TOR1* coil geometry. The coil may contain 4-6 layers with 47 turns per layer.

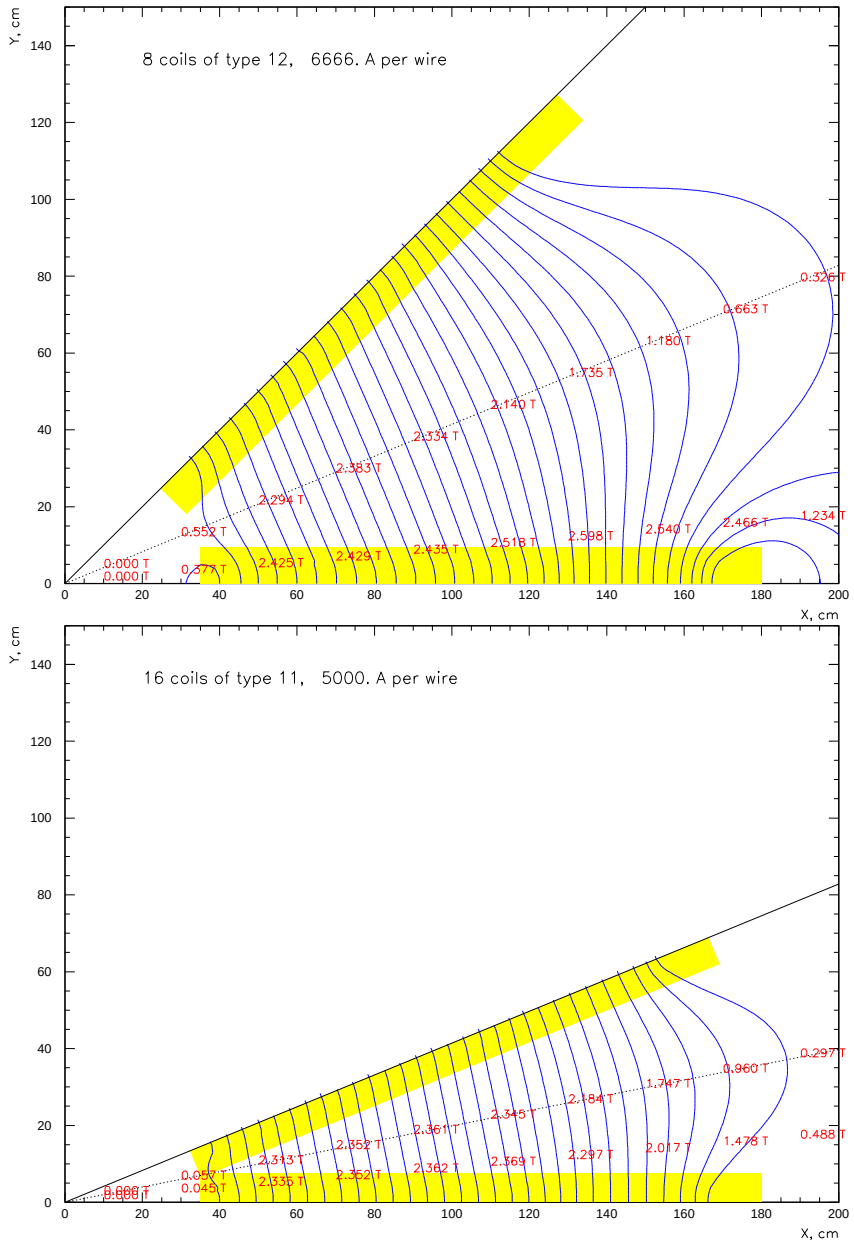

Figure D.4: The field maps of the *TOR1* toroidal magnet. Top: 8 coils with 6 layers per coil, at 6.7 kA/cm^2. Bottom: 16 coils with 4 layers per coil, at 5.0 kA/cm^2

Magnet	type	coils	layers/coil	turns/layer	kA/cm^2	B_{max}, T	MJ
TOR2	G0	8	4	36	5.0	4.0	7.6
TOR1	a)	8	6	47	6.7	6.0	60.0
	b)	16	4	47	5.0	4.0	55.0

Table D.1: The parameters of the toroidal magnets considered.

is the radial component. Therefore, 16-coil option partly recovers its loss of acceptance.

D.3 Spectrometer Resolution

To evaluate the spectrometer resolution, an empirical, "look-up table" approach similar to one used for the solenoidal spectrometer (see Section 3.2.3) was used. The segments of the particle trajectory are reconstructed in both spectrometer arms, the momentum is evaluated based on the bend in *TOR2*, using look-up tables, then the scattering angle is evaluated using another look-up tables, projecting the bend in *TOR1*. The uncertainty in momentum and in angle are strongly correlated. For this first evaluation, the φ dependence of the field was ignored, only the trajectories lying in the central plane of a sector have been considered. The results are shown in Fig. D.5. The resolution is better than that of the solenoid spectrometer (see Section 3.2.3).

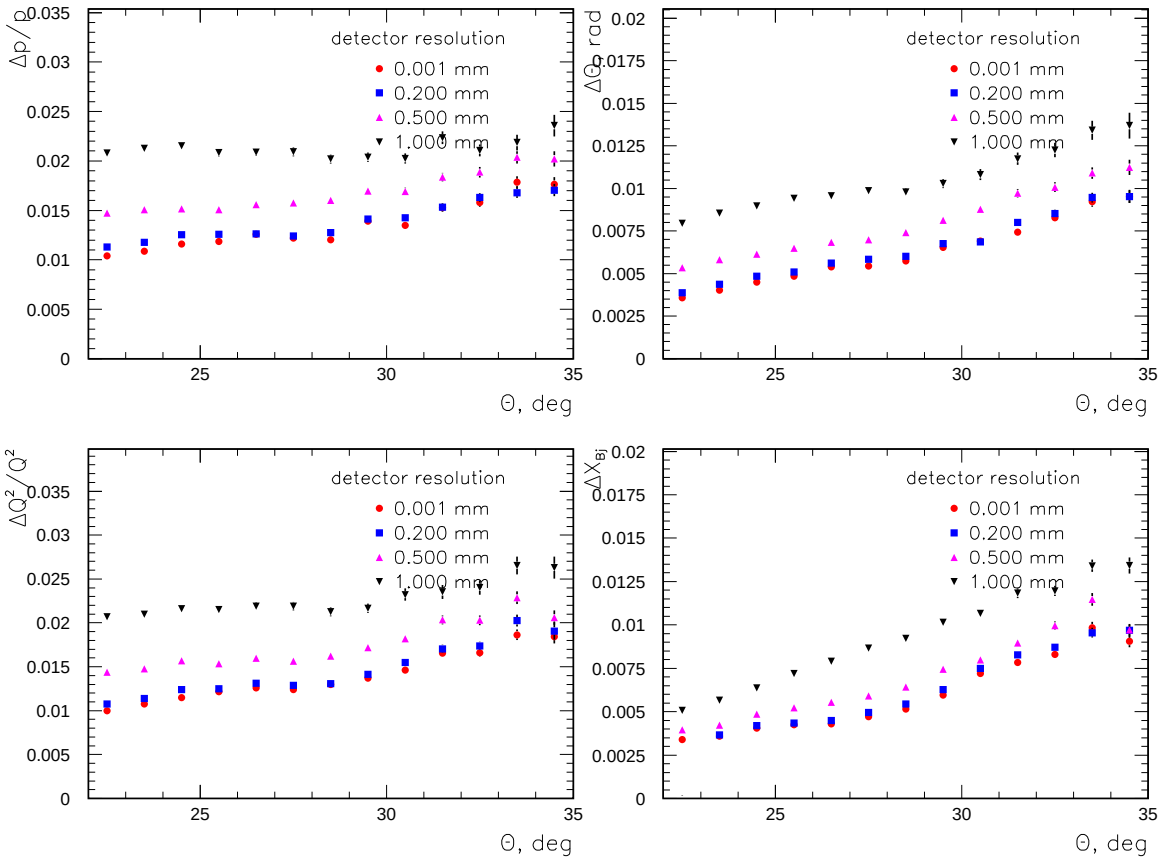

Figure D.5: The spectrometer resolutions (RMS) in momentum p and the scattering angle θ, as well as the derived DIS variables Q^2 and x_{Bj}. These resolutions are calculated for 4 different detector position resolutions.

Process	DTS-8	DTS-16
DIS total	20 kHz	16.0 kHz
DIS $W > 2$ GeV, $x_{Bj} > 0.65$	8 kHz	6.4 kHz
π^- $P > 0.3$ GeV	200 kHz	160 kHz

Table D.2: Calculated DIS and pion rates for two *TOR1* options: with 8 coils (DTS-8) and with 16 coils (DTS-16).

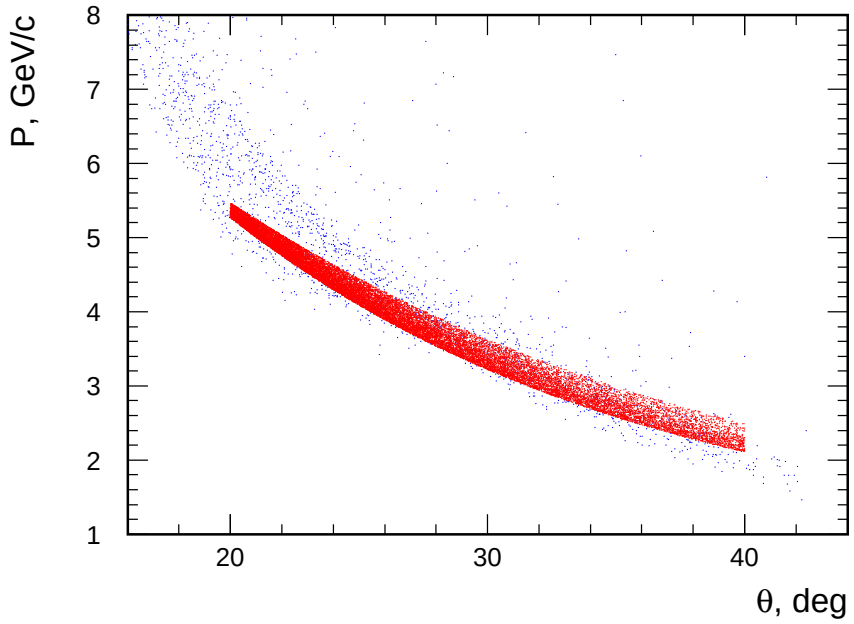

Figure D.6: The DTS acceptance area in the $p - \theta$ plane (blue dots) matches well the DIS $x_{Bj} > 0.65$ sample (red dots).

D.4 The Acceptance and the Rates

The DIS and background rates were evaluated similar to the SoLID design (see Section 3.2.8). The rates calculated for various conditions are presented in Tab. D.2. The DIS $x_{Bj} > 0.65$ rates are comparable to those for SoLID (see Table 3.3), but the pion rate is nearly 3 orders of magnitude lower. Also, the DIS $0.55 < x_{Bj} < 0.65$ events are suppressed and would require a separate run at lower magnetic fields. The acceptance of DTS is extremely selective to a certain kinematics range, which is illustrated in Fig. D.6.

D.5 Implementation

In comparison with the SoLID design, the DTS design requires a new and complex magnet to be built. The rest of the spectrometer, including the detectors is conceptually

much simpler than the SoLID spectrometer. Due to low backgrounds the requirements to the detectors, PID and the trigger are relaxed in comparison with the SoLID design. However, because of the 2-arm setup, twice as many coordinate detectors are needed.

D.5.1 Magnets

Building *TOR1* is a serious challenge because of the size, the coil complexity and the stored energy. The 16-coil magnet would operate in safe conditions as far as the superconductor stability is concerned. The 8-coil version may be beyond the allowed area and further evaluation is necessary.

The G0 magnet will require a considerable refurbishing. The frontal wall has to be equipped with thin windows, similarly to the rear wall. The heavy shielding, installed inside the vacuum vessel, has to be removed.

D.5.2 Coordinate Detectors

Lower background rates in the toroid-based design will allow for the use of more conventional detectors. The minimal detector to accomplish the goals of the experiment needs to have a threshold Cherenkov detector to π/e discrimination, tracking detectors both downstream an upstream of *TOR2*, trigger scintillators and a preshower/shower calorimeter system. In the following, these detectors will be described in greater detail and rough cost estimates are made for each element.

Tracking Chambers

The spectrometer will measure the bend of each particles trajectory in *TOR2*. To do this accurately, two sets of tracking chambers are required on both the upstream and downstream side of *TOR2* for each of the 8 sectors, that is a total of 32 individual tracking chambers. The resolution of the spectrometer in terms of the relevant kinematic variables as a function of the tracking resolution is shown in Fig. D.5. Each set of tracking chambers would consist of a u, u' pair and a v, v' pair. The chambers upstream of *TOR2* would cover radially from 100 to 150 cm, and the two chambers downstream of *TOR2* would cover from 50 to 150 cm radially. (See Fig. D.1.) The two options under consideration for these chambers are an MWPC with 2 mm cells or a drift chamber with 1 cm cells. Either chamber will give sufficient resolution for the measurements; although, the drift chamber or a *finer* pitched MWPC might be preferred as shown in Fig. D.5. The MWPC has the advantage that it can handle 10× the rate as the drift chamber, based on geometry and the use of a gas with a faster drift velocity. It does this at the expense of more channels and the likely need for a recirculating gas system. The upstream (downstream) MWPC's would require 250 (500) channels/plane. This is compared with the 50 (100) channels for the drift chambers. In either case, the preamp and readout could be done for approximately $33/channel using custom, FPGA-based readout cards similar to a design being implemented in Fermilab E-906/Drell-Yan. Based on this and a very rough estimate of the cost of building 32 nearly-identical chambers the

entire tracking hardware and readout could be constructed for approximately \$2.3M for the drift chambers (without contingency or indirect costs) or approximately twice that for the MWPC solution because of the significant increase in readout channels.

Preshower and Shower Detectors

The preshower and shower detectors are needed for electron/pion separation. As a rough guide, we anticipate using a 10 cm thick (3.7 X_0) Pb-Glass preshower followed by a 25 cm Pb-Glass (9.3 X_0) shower counter. This gives a total of 13 X_0 of material. The PRIMEX collaboration was able to obtain Pb-Glass for approximately \$1/cm^3 in a collaboration with ITEP [105] in 1999, or around \$1.30 today. While this collaboration has not been explored, we use this as a cost basis for Pb-Glass. Each of the eight sectors will have approximately 6,100 cm^2 area so that the preshower counter will cost approximately \$79k and the shower counter will cost approximately \$198k. The sector can be covered by 16 blocks of $10\times10\times(35-60)$ cm^3 for the preshower and 66 blocks of $10\times10\times25$ cm^3 for the shower. These 82 channels/sector could be outfitted with photomultipliers/bases/shields for approximately \$300/channel with an additional \$100/channel for readout electronics. The total cost for eight sectors would be approximately \$2.5M (without contingency or indirect cots). It is likely that some amount of the Pb-Glass detectors could be recovered from existing experiments which have been decommissioned.

Trigger Scintillators and Gas Cherenkov

In the DTS design there will be two sets of trigger scintillators, one before and one after *TOR2*. These could be 10 cm wide strips aligned with the preshower counters. Based on quotes from Eljen Technology, the scintillator and light guide material for each sector should cost around \$4k, with the caveat that a substantial component of plastics is oil, the price of which has been fluctuating wildly in recent years. Using the same readout cost/channel as for the shower counters (\$400/channel) and 32 channels/sector, the total cost per sector is \$17k or \$134k or the entire spectrometer.

The threshold Cherenkov would be set of eight volumes of relatively simple geometry. It is hoped that much of the technology being used in the Cherenkov for the CLAS12 upgrade can be duplicated for the DTS Cherenkov counter, and might be realized for around \$400k. Unlike the preferred solenoid spectrometer solution, this Cherenkov will not have large magnetic fields located near the photomultiplier tubes.

Summary of DTS Detectors and Cost

The particle position and identification detectors used in the DTS are envisioned as very conventional nuclear physics detectors. These are proven technologies with relative easily justified cost estimates. Particle identification will be done with a combination of a threshold Cherenkov counter for each sector and preshower/shower detectors. The momentum measurement will be made by measuring the bend of the particle though the essentially dipole field in each toroid section with conventional drift chambers on each

Table D.3: A very rough cost estimate of the DTS detector package is given in this table. This estimate is extremely preliminary, so contingency of 50% is assumed. Indirect rates would vary depending on the institution at which the work is done.

	Cost (k$)	
Item	Base Cost	w/50% Cont.
Tracking	2,300	3,450
Preshower/shower	2,500	3,700
Hodoscope & Cherenkov	534	801
Total	5,334	7,951

side. Triggering will be one with scintillator hodoscopes located near two of the tracking stations. The total cost is estimated to be $5.3M (without contingency and indirect costs) and is broken down in Tab. D.3.

Bibliography

[1] T. Hobbs and W. Melnitchouk, "Finite-Q^2 corrections to parity-violating DIS," *Phys. Rev.*, vol. D77, p. 114023, 2008, 0801.4791.

[2] A. Acha *et al.*, "Precision Measurements of the Nucleon Strange Form Factors at $Q^2 \sim 0.1$-GeV^2," *Phys. Rev. Lett.*, vol. 98, p. 032301, 2007, nucl-ex/0609002.

[3] K. A. Aniol *et al.*, "Parity-violating electroweak asymmetry in e(pol.) p scattering," *Phys. Rev.*, vol. C69, p. 065501, 2004, nucl-ex/0402004.

[4] D. S. Armstrong *et al.*, "Strange quark contributions to parity-violating asymmetries in the forward G0 electron proton scattering experiment," *Phys. Rev. Lett.*, vol. 95, p. 092001, 2005, nucl-ex/0506021.

[5] F. E. Maas *et al.*, "Evidence for strange quark contributions to the nucleon's form factors at $Q^2 = 0.108$-(GeV/c)^2," *Phys. Rev. Lett.*, vol. 94, p. 152001, 2005, nucl-ex/0412030.

[6] C. J. Horowitz, S. J. Pollock, P. A. Souder, and R. Michaels, "Parity Violating Measurements of Neutron Densities," *Phys. Rev.*, vol. C63, p. 025501, 2001, nucl-th/9912038.

[7] C. Y. Prescott *et al.*, "Parity non-conservation in inelastic electron scattering," *Phys. Lett.*, vol. B77, pp. 347–352, 1978.

[8] C. Y. Prescott *et al.*, "Further Measurements of Parity Nonconservation in Inelastic electron Scattering," *Phys. Lett.*, vol. B84, p. 524, 1979.

[9] P. A. Souder *et al.*, "Measurement of parity violation in the elastic scattering of polarized electrons from C-12," *Phys. Rev. Lett.*, vol. 65, pp. 694–697, 1990.

[10] P. L. Anthony *et al.*, "Precision measurement of the weak mixing angle in Moeller scattering," *Phys. Rev. Lett.*, vol. 95, p. 081601, 2005, hep-ex/0504049.

[11] S.-L. Zhu, S. J. Puglia, B. R. Holstein, and M. J. Ramsey-Musolf, "The nucleon anapole moment and parity-violating e p scattering," *Phys. Rev.*, vol. D62, p. 033008, 2000, hep-ph/0002252.

[12] R. D. Young, J. Roche, R. D. Carlini, and A. W. Thomas, "Extracting nucleon strange and anapole form factors from world data," *Phys. Rev. Lett.*, vol. 97, p. 102002, 2006, nucl-ex/0604010.

[13] A. Accardi and W. Melnitchouk, "Target mass corrections for spin-dependent structure functions in collinear factorization," 2008, 0808.2397.

[14] X. C. Zheng, "Disparity e08-011." URL http://hallaweb.jlab.org/experiment/E05-007/.

[15] M. J. Ramsey-Musolf and S. Su, "Low energy precision test of supersymmetry," *Phys. Rept.*, vol. 456, pp. 1–88, 2008, hep-ph/0612057.

[16] A. Kurylov, M. J. Ramsey-Musolf, and S. Su, "Supersymmetric effects in parity-violating deep inelastic electron nucleus scattering," *Phys. Lett.*, vol. B582, pp. 222–228, 2004, hep-ph/0307270.

[17] J. T. Londergan and A. W. Thomas, "The validity of charge symmetry for parton distributions," *Prog. Part. Nucl. Phys.*, vol. 41, pp. 49–124, 1998, hep-ph/9806510.

[18] J. T. Londergan and A. W. Thomas, "Charge symmetry violation corrections to determination of the Weinberg angle in neutrino reactions," *Phys. Rev.*, vol. D67, p. 111901, 2003, hep-ph/0303155.

[19] J. T. Londergan and A. W. Thomas, "Charge symmetry violating contributions to neutrino reactions," *Phys. Lett.*, vol. B558, pp. 132–140, 2003, hep-ph/0301147.

[20] G. P. Zeller *et al.*, "A precise determination of electroweak parameters in neutrino nucleon scattering," *Phys. Rev. Lett.*, vol. 88, p. 091802, 2002, hep-ex/0110059. [Erratum-ibid. **90**, 239902 (2003)].

[21] A. D. Martin, R. G. Roberts, W. J. Stirling, and R. S. Thorne, "Uncertainties of predictions from parton distributions. II: Theoretical errors," *Eur. Phys. J.*, vol. C35, pp. 325–348, 2004, hep-ph/0308087.

[22] E. Sather, "Isospin violating quark distributions in the nucleon," *Phys. Lett.*, vol. B274, pp. 433–438, 1992.

[23] E. N. Rodionov, A. W. Thomas, and J. T. Londergan, "Charge asymmetry of parton distributions," *Mod. Phys. Lett.*, vol. A9, pp. 1799–1806, 1994.

[24] A. D. Martin, R. G. Roberts, W. J. Stirling, and R. S. Thorne, "Parton distributions incorporating QED contributions," *Eur. Phys. J.*, vol. C39, pp. 155–161, 2005, hep-ph/0411040.

[25] M. Gluck, P. Jimenez-Delgado, and E. Reya, "Radiatively generated isospin violations in the nucleon and the NuTeV anomaly," *Phys. Rev. Lett.*, vol. 95, p. 022002, 2005, hep-ph/0503103.

[26] J. T. Londergan, D. P. Murdock, and A. W. Thomas, "Parton charge symmetry violation: Electromagnetic effects and W production asymmetries," *Phys. Rev.*, vol. D73, p. 076004, 2006, hep-ph/0603208.

[27] J. T. Londergan, D. P. Murdock, and A. W. Thomas, "Experimental tests of charge symmetry violation in parton distributions," *Phys. Rev.*, vol. D72, p. 036010, 2005, hep-ph/0507029.

[28] J. T. Londergan and A. W. Thomas, "Implications of current constraints on parton charge symmetry," *J. Phys.*, vol. G31, pp. 1151–1163, 2005.

[29] M. Virchaux and A. Milsztajn, "A Measurement of alpha-s and higher twists from a QCD analysis of high statistics F-2 data on hydrogen and deuterium targets," *Phys. Lett.*, vol. B274, pp. 221–229, 1992.

[30] P. Amaudruz *et al.*, "The ratio F_2(n) / F_2(p) in deep inelastic muon scattering," *Nucl. Phys.*, vol. B371, pp. 3–31, 1992.

[31] J. Blumlein and H. Bottcher, "Higher Twist Contributions to the Structure Functions $F_2^p(x,Q^2)$ and $F_2^d(x,Q^2)$ at Large x and Higher Orders," *Phys. Lett.*, vol. B662, pp. 336–340, 2008, 0802.0408.

[32] J. D. Bjorken, "Model independent remarks on electron - quark parity violating neutral - current couplings," *Phys. Rev.*, vol. D18, p. 3239, 1978.

[33] L. Wolfenstein, "Testing the Weinberg-Salam model in polarized e d and e p deep inelastic scattering," *Nucl. Phys.*, vol. B146, p. 477, 1978.

[34] E. Derman, "Parity violation in polarized electron - deuteron scattering without the parton model," *Phys. Rev.*, vol. D19, p. 133, 1979.

[35] S. J. Brodsky, "Dynamical higher-twist and high x phenomena: A window to quark quark correlations in QCD," 2000, hep-ph/0006310.

[36] P. Castorina and P. J. Mulders, "Twist four corrections to asymmetry in polarized electron Deuteron scattering," *Phys. Rev.*, vol. D31, pp. 2760–2764, 1985.

[37] S. Fajfer and R. J. Oakes, "Twist - Four Effects on the Asymmetry in Polarized Electron Deuteron Scattering and Sin**2-Theta(W)," *Phys. Rev.*, vol. D30, p. 1585, 1984.

[38] R. L. Jaffe and M. Soldate, "Twist Four in the QCD Analysis of Leptoproduction," *Phys. Lett.*, vol. B105, pp. 467–472, 1981.

[39] S. Alekhin, S. Kulagin, and R. Petti, "Update of the global fit of PDFs including the low-Q DIS data," 2008, 0810.4893.

[40] U.-K. Yang, A. Bodek, and Q. Fan, "Parton distributions, d/u, and higher twists at high x," 1998, hep-ph/9806457.

[41] M. Tzanov *et al.*, "Precise measurement of neutrino and anti-neutrino differential cross sections," *Phys. Rev.*, vol. D74, p. 012008, 2006, hep-ex/0509010.

[42] W. Melnitchouk, I. R. Afnan, F. R. P. Bissey, and A. W. Thomas, "Comment on 'Parton distributions, d/u, and higher twist effects at high x'," *Phys. Rev. Lett.*, vol. 84, p. 5455, 2000, hep-ex/9912001.

[43] W. Melnitchouk and A. W. Thomas, "Neutron / proton structure function ratio at large x," *Phys. Lett.*, vol. B377, pp. 11–17, 1996, nucl-th/9602038.

[44] S. I. Alekhin, "Global fit to the charged leptons DIS data: α(s), parton distributions, and high twists," *Phys. Rev.*, vol. D63, p. 094022, 2001, hep-ph/0011002.

[45] S. Kuhlmann *et al.*, "Large-x parton distributions," *Phys. Lett.*, vol. B476, pp. 291–296, 2000, hep-ph/9912283.

[46] S. Bultmann, "The BoNuS experiment at Jefferson Lab," *AIP Conf. Proc.*, vol. 747, pp. 46–49, 2005.

[47] I. Cloet, W. Bentz, and A. W. Thomas. private communication.

[48] B. Aubert *et al.*, "The BaBar detector," *Nucl. Instrum. Meth.*, vol. A479, pp. 1–116, 2002, hep-ex/0105044.

[49] K. Halbach and R. F. Holsinger, "Superfish-a Computer Program for Evaluation of RF Cavities with Cylindrical Symmetry," *Part. Accel.*, vol. 7, pp. 213–222, 1976.

[50] R. Brun *et al.*, "GEANT Detector Description and Simulation Tool, CERN Program Library (1993)," We use GEANT version 3.21.

[51] "HEPDATA: Reaction Database." URL http://www.slac.stanford.edu/spires/hepdata/.

[52] D. E. Wiser, *Inclusive photoproduction of protons, kaons, and pions at SLAC energies*. PhD thesis, U. of Wisconsin, 1977. UMI 77-19743.

[53] S. Bachmann *et al.*, "Performance of GEM detectors in high intensity particle beams," *Nucl. Instrum. Meth.*, vol. A470, pp. 548–561, 2001.

[54] B. Ketzer, Q. Weitzel, S. Paul, F. Sauli, and L. Ropelewski, "Performance of triple GEM tracking detectors in the COMPASS experiment," *Nucl. Instrum. Meth.*, vol. A535, pp. 314–318, 2004.

[55] J. Alcorn *et al.*, "Basic Instrumentation for Hall A at Jefferson Lab," *Nucl. Instrum. Meth.*, vol. A522, pp. 294–346, 2004.

[56] L. W. Mo and Y.-S. Tsai, "Radiative corrections to elastic and inelastic e p and mu p scattering," *Rev. Mod. Phys.*, vol. 41, pp. 205–235, 1969.

[57] W. J. Marciano and A. Sirlin, "On Some General Properties of the O(alpha) Corrections to Parity Violation in Atoms," *Phys. Rev.*, vol. D29, p. 75, 1984.

[58] K. Hagiwara *et al.*, "Review of particle physics," *Phys. Rev.*, vol. D66, p. 010001, 2002.

[59] S. Eidelman *et al.*, "Review of particle physics," *Phys. Lett.*, vol. B592, p. 1, 2004.

[60] K. Abe *et al.*, "A high-precision measurement of the left-right Z boson cross-section asymmetry," *Phys. Rev. Lett.*, vol. 84, pp. 5945–5949, 2000, hep-ex/0004026.

[61] K. Kumar, R. Michaels, P. Souder, and G. Urciuolli, "The lead radius experiment prex, e06002." URL http://hallaweb.jlab.org/parity/prex/.

[62] K. Paschke and P. s. Souder, "Happex-iii, e05-009."

[63] R. P. I. Carlini, "The qweak experiment." URL http://www.jlab.org/Hall-C/Qweak/index.html.

[64] P. Fabbricatore *et al.*, "The Superconducting magnet for the BaBar detector of the PEP-II B factory at SLAC," *IEEE Trans. Magnetics*, vol. 32, pp. 2210–2213, 1996.

[65] R. A. Bell *et al.*, "The BaBar superconducting coil: Design, construction and test," *Nucl. Phys. Proc. Suppl.*, vol. 78, pp. 559–564, 1999.

[66] D. Boutigny *et al.*, "BaBar technical design report," SLAC-R-0457.

[67] C. Bernet *et al.*, "The 40-cm x 40-cm gaseous microstrip detector Micromegas for the high-luminosity COMPASS experiment at CERN," *Nucl. Instrum. Meth.*, vol. A536, pp. 61–69, 2005.

[68] E. Abat *et al.*, "The ATLAS Transition Radiation Tracker (TRT) proportional drift tube: Design and performance," *JINST*, vol. 3, p. P02013, 2008.

[69] M. Ziegler, P. Sievers, and U. Straumann, "A triple GEM detector with two-dimensional readout," *Nucl. Instrum. Meth.*, vol. A471, pp. 260–263, 2000.

[70] G. S. Atoian *et al.*, "Development of shashlik calorimeter for KOPIO," *Nucl. Instrum. Meth.*, vol. A531, pp. 467–480, 2004, physics/0310047.

[71] G. S. Atoian *et al.*, "An Improved Shashlyk Calorimeter," *Nucl. Instrum. Meth.*, vol. A584, pp. 291–303, 2008, 0709.4514.

[72] A. Zoccoli, "The electromagnetic calorimeter of the HERA-B experiment," *Nucl. Instrum. Meth.*, vol. A446, pp. 246–252, 2000.

[73] G. Avoni *et al.*, "The electromagnetic calorimeter of the HERA-B experiment," *Nucl. Instrum. Meth.*, vol. A580, pp. 1209–1226, 2007.

[74] A. A. Alves *et al.*, "The LHCb Detector at the LHC," *JINST*, vol. 3, p. S08005, 2008.

[75] Z. Fraenkel *et al.*, "A hadron blind detector for the PHENIX experiment at RHIC," *Nucl. Instrum. Meth.*, vol. A546, pp. 466–480, 2005, physics/0502008.

[76] F. Sauli, "Novel Cherenkov photon detectors," *Nucl. Instrum. Meth.*, vol. A553, pp. 18–24, 2005.

[77] R. Chechik, A. Breskin, and C. Shalem, "Thick GEM-like multipliers: A simple solution for large area UV-RICH detectors," *Nucl. Instrum. Meth.*, vol. A553, pp. 35–40, 2005, physics/0502131.

[78] N. Falletto *et al.*, "Compton scattering off polarized electrons with a high finesse Fabry-Perot cavity at JLab," *Nucl. Instrum. Meth.*, vol. A459, pp. 412–425, 2001.

[79] C. Møller, "Zur Theorie des Durchgangs schneller Elektronen durch Materie," *Annalen der Physik*, vol. 406, pp. 531–585, 1932.

[80] A. A. Kresnin and L. N. Rosentsveig, "Polarization asymmetry of møller scattering," *Soviet JETP*, vol. 5, pp. 288–292, 1957.

[81] A. M. Bincer, "Scattering of longitudinally polarized fermions," *Phys. Rev.*, vol. 107, pp. 1434–1438, Sep 1957.

[82] P. S. Cooper *et al.*, "Polarized electron Electron Scattering at GeV Energies," *Phys. Rev. Lett.*, vol. 34, p. 1589, 1975.

[83] B. Wagner *et al.*, "A Møller polarimeter for CW and pulsed intermediate-energy electron beams," *Nucl. Instrum. Meth.*, vol. A294, pp. 541–548, 1990.

[84] J. Arrington *et al.*, "A Variable energy Møller polarimeter at the MIT Bates Linear Accelerator Center," *Nucl. Instrum. Meth.*, vol. A311, pp. 39–48, 1992.

[85] K. B. Beard *et al.*, "Measurement of the polarization of a pulsed electron beam with a Møller polarimeter in the coincidence mode," *Nucl. Instrum. Meth.*, vol. A361, pp. 46–52, 1995.

[86] H. R. Band, G. Mitchell, R. Prepost, and T. Wright, "A Møller polarimeter for high energy electron beams," *Nucl. Instrum. Meth.*, vol. A400, pp. 24–33, 1997.

[87] A. V. Glamazdin *et al.*, "Electron beam Moeller polarimeter at JLAB Hall A," *Fizika*, vol. B8, pp. 91–95, 1999, hep-ex/9912063.

[88] M. Hauger *et al.*, "A high-precision polarimeter," *Nucl. Instrum. Meth.*, vol. A462, pp. 382–392, 2001, nucl-ex/9910013.

[89] P. Steiner, A. Feltham, I. Sick, M. Zeier, and B. Zihlmann, "A high-rate coincidence Møller polarimeter," *Nucl. Instrum. Meth.*, vol. A419, pp. 105–120, 1998.

[90] G. G. Scott, "Review of gyromagnetic ratio experiments," *Rev. Mod. Phys.*, vol. 34, pp. 102–109, Jan 1962.

[91] D. Gaskell, D. G. Meekins, and C. Yan, "New methods for precision Møller polarimetry," *Eur. Phys. J.*, vol. A32, pp. 561–564, 2007.

[92] L. G. Levchuk, "The Intraatomic motion of bound electrons as a possible source of a systematic error in electron beam polarization measurements by means of a Møller polarimeter," *Nucl. Instrum. Meth.*, vol. A345, pp. 496–499, 1994.

[93] E. Chudakov and V. Luppov, "Møller polarimetry with atomic hydrogen targets," *IEEE Trans. Nucl. Sci.*, vol. 51, pp. 1533–1540, 2004.

[94] E. Chudakov and V. Luppov, "Moeller polarimetry with atomic hydrogen targets," *Eur. Phys. J.*, vol. A24S2, pp. 123–126, 2005.

[95] E. Chudakov and V. Luppov, "Møller polarimetry with atomic hydrogen targets," tech. rep., JLab, 2005. URL http://www.jlab.org/~gen/hyd/loi_3.pdf.

[96] I. F. Silvera, "Ultimate fate of a gas of atomic hydrogen in a liquid-helium chamber: Recombination and burial," *Phys. Rev. B*, vol. 29, pp. 3899–3904, Apr 1984.

[97] I. F. Silvera and J. T. M. Walraven, "Stabilization of atomic hydrogen at low temperature," *Phys. Rev. Lett.*, vol. 44, pp. 164–168, Jan 1980.

[98] I. F. Silvera and J. T. M. Walraven, "Spin polarized atomic hydrogen," *Progress in Low Temperature Physics, vol. X*, pp. 139–370, 1986.

[99] T. Roser *et al.*, "Microwave driven extraction of stabilized spin polarized atomic hydrogen," *Nucl. Instrum. Meth.*, vol. A301, pp. 42–46, 1991.

[100] M. Mertig, V. G. Luppov, T. Roser, and B. Vuaridel, "Continuous density measurement of atomic hydrogen by means of a bolometer," *Rev. Sci. Instrum.*, vol. 62, pp. 251–252, 1991.

[101] M. D. Miller and L. H. Nosanow, "Possible "new" quantum systems. ii. properties of the isotopes of spin-aligned hydrogen," *Phys. Rev. B*, vol. 15, pp. 4376–4385, May 1977.

[102] L. V. de Bever, J. Jourdan, M. Loppacher, S. Robinson, I. Sick, and J. Zhao, "A target for precise mller polarimetry," *Nucl. Instrum. Meth.*, vol. A400, no. 2-3, pp. 379 – 386, 1997.

[103] P. D. Brindza, D. Beck, R. Laszewski, L. Bartoszek, R. Wands, and D. Mitchell, "Superconducting toroidal magnet design for the G0 experiment at TJNAF," *IEEE Trans. Appl. Supercond. (USA)*, vol. 7, no. 2, pp. 618–621, 1997.

[104] P. D. Brindza, D. Beck, K. Nakahara, D. Spayde, S. Williamson, T. A. Antaya, M. Trepanitis, and T. Brandsberg, "The G0 spectrometer superconducting magnet system: from a challenging construction to reliable operations," *IEEE Trans. Appl. Supercond. (USA)*, vol. 16, no. 2, pp. 248–252, 2006.

[105] A. Gasparian *et al.*, "Conceptual Design Report: A Precision Measurement of the Neutral Pion Lifetime via the Primakoff Effect," 1999.